Dwarf galaxies in a cosmological context: A testbench for galaxy modeling

Christine M. Simpson

Submitted in partial fulfillment of the
requirements for the degree
of Doctor of Philosophy
in the Graduate School of Arts and Sciences

COLUMBIA UNIVERSITY

2014

©2013
Christine M. Simpson
All rights reserved

ABSTRACT

Dwarf galaxies in a cosmological context: A testbench for galaxy modeling

Christine M. Simpson

Presented here are simulated models for the evolution of a 10^9 $M_\odot$ dark matter halo in a cosmological setting with an adaptive mesh refinement code as an analog to local low-luminosity dwarf irregular and dwarf spheroidal galaxies. The primary goals of this study are to investigate the roles of reionization and supernova feedback in determining the star-formation histories of low-mass dwarf galaxies and to explore the effect of differing numerical implementations of supernova feedback on galactic enrichment and winds. Our models include a wide range of physical effects, including metal cooling, molecular hydrogen formation and cooling, photoionization and photodissociation from a metagalactic (but not local) background, a simple prescription for self-shielding, star formation and two different models for supernova-driven energetic feedback. To better understand the impact of each physical effect, we carry out simulations excluding each major effect in turn. We find that reionization is primarily responsible for expelling most of the gas in our simulations, but that supernova feedback is required to disperse the dense, cold gas in the core of the halo. Moreover, we show that the timing of reionization can

produce an order-of-magnitude difference in the final stellar mass of the system. While the stellar masses produced in our models with purely thermal supernova feedback are consistent with observed low-luminosity dwarfs, the resulting median stellar metallicity is considerably larger than observed systems. We investigate the efficacy of purely thermal energetic feedback, and suggest that it may still suffer from excessive radiative losses, despite reaching stellar particle masses of about 100 $M_\odot$ and a comoving spatial resolution of 11 pc. We investigate a second model for supernova feedback that includes kinetic as well as thermal energy in the proportions predicted by Sedov-Taylor models on the resolution scales of our galaxy simulations. We extensively test the effect of this model in media of different densities and at different resolutions and we conclude that the inclusion of kinetic energy is most important in dense gas simulated at low resolution. The effect of this new model on our simulated dwarf galaxy is significant, as it produces stronger galactic winds that suppress and regulate star formation and more efficiently eject metals from star forming gas. The resulting system at $z = 0$ has an order of magnitude lower luminosity and an average stellar metallicity consistent with observed dwarfs. The distribution of stellar metallicity is too narrowly peaked, however, indicating the need for further refinement of our model and perhaps the inclusion other sources of stellar feedback such as Type Ia supernovae or stellar winds. We conclude that the observed chemical abundance patterns in local dwarf galaxies provide a unique testbench for refining models of stellar feedback in galaxy simulations at high resolution.

Contents

List of Figures

List of Tables

ACKNOWLEDGMENTS

This is probably the most difficult section of this thesis to write, because it can't possibly be complete, but I will make an attempt.

First, I would like to thank the astronomy department at Columbia. I remember six years ago how uncertain I was about coming to Columbia, but joining this department has honestly been one of the best decisions of my life. So many people here have taught me so much, I've grown tremendously as a researcher, a thinker, a teacher, a student, a leader and a friend. The galaxies group at Columbia has been especially supportive and I'm so grateful for the opportunity to be a part of such a special group. I also have to thank Millie and Ayoune for all their help and support in navigating the Columbia bureaucracy.

Before I came to Columbia, I had many other wonderful teachers. I'd like to thank the mathematics and astronomy departments at Wellesley College, especially Steve Slivan, Kim McLeod and Wendy Bauer. Wellesley seems like so long ago, but it has been such an important stepping stone in my life in so many ways.

I am tremendously grateful for the two foundational years I spent at Wesleyan University. My thesis advisor at Wesleyan, Bill Herbst, taught me so much about research. I'm also grateful for the support I received from Kathy LeDuc, John Salzer, Kathy Rhode and Ed Moran. I wouldn't be here without them.

Leaving Columbia means I won't get to see my fellow grads everyday. I've had a taste of how this feels over the past few years as friends have graduated. I will miss all of you, but we will see each other often, I'm sure. I've had so many fantastic office mates: Erika, Yuan, David and Steven; I wish you could all come to Heidelberg! So many

other grads have been fantastic friends as well: Lia, Josh, Colin, Joo, Jenna, Ximena, Taka, Cameron, Stephanie, Munier, Lauren, Sarah, Maureen, Duane, Jeff, Jennifer, Dan, Destry, Maria, Kyle, Neil, Kathryn and Adrian.

My committee and mentors throughout my time at Columbia have been such important sources of advice and support. Mary, David, Mordecai and Jacqueline have all very patiently supported me over the years.

If it weren't for Kathryn Johnston, I probably wouldn't be at Columbia. My almost advisor has always been a great source of perspective over the years, and I'm very grateful for her support.

I cannot thank Greg Bryan enough for his support and guidance over the past five years. We've had so many meetings and discussions over the years, and no matter what mood I came into the room with, I always left feeling better about our research and eager to tackle it head on.

Hannah Barker has been one of my best friends over the past six years and has always been there for me to lean on. I could write a song about it; it would be very sappy song, but true! I honestly cannot imagine spending these years in New York without her; she is one of the most level headed people I know, and I'm going to miss her terribly next year.

Finally, my most important thanks and love go to my parents. They haven't always understood the past six years, but they've always supported me. I am tremendously grateful for all the love and support they have given me over the years.

June 2013, New York City

Chapter 1

Introduction

1.1 Dwarf galaxies and their place in the Universe

Dwarf galaxies offer some of the most fascinating puzzles in modern cosmology. The currently favored cosmological model for the universe, ΛCDM, predicts a large number of small dark matter halos in the Universe with the potential to host dwarf galaxies. We expect to find thousands of these systems around large galaxies like the Milky Way. The fact that we do not see this number of luminous systems (Klypin et al. 1999; Moore et al. 1999) and that the properties of the systems are not what we expect (Boylan-Kolchin et al. 2012) is an interesting conundrum. The internal dynamics of Milky Way dwarfs certainly suggest that they are extremely dark matter dominated systems if their gravity is indeed Newtonian, which would lend support to the idea that the dwarfs we see may be part of a larger dark or under-luminous population of low mass dark matter halos.

A variety of astrophysical effects may act to suppress the baryon content of dwarf galaxies. Empirically, there are many clues that implicate a variety of processes in the

suppression of dwarf galaxy formation. The strong environmental quenching observed in luminous dwarfs (Geha et al. 2012) and the correlation between distance and gas content seen in less luminous Local Group dwarfs (Grcevich & Putman 2009) indicate that environmental effects such as ram pressure stripping may play an important role in suppressing star formation and removing gas from dwarfs. Many dwarfs have star formation histories dominated by old stellar populations indicating that a universal star formation suppression mechanism such as reionization may play an important role in dwarf evolution (Weisz et al. 2011b; Monelli et al. 2010). The extremely low stellar metallicities found in Milky Way dwarf spheroidal galaxies (dSphs) relative to the expected metal production of their stellar populations indicate that nearly all of the metals produced by stars in these systems are lost (Kirby et al. 2012). This degree of metal loss indicates a process that preferentially removes metal rich gas from these systems. A likely possibility for such a mechanism is supernova feedback, which may also play a role in the suppression star formation. The impact of supernova feedback may also be implicated in the internal dynamics of Milky Way dSphs. These data, when combined with dynamical modeling, seem to indicate that in some systems the central dynamical potential may be much shallower than the predictions of ΛCDM (Walker & Peñarrubia 2011). Supernova heating, through its impact on gas dynamics, may act to destroy dark matter cusps (Pontzen & Governato 2012).

With such a diverse array of galaxy suppression mechanisms at play in dwarfs, it is no wonder that their baryon content as a function of circular velocity, in addition to being low, is also very scattered and follows no well defined trend (unlike massive disk galaxies) (McGaugh et al. 2010). This gives the impression that dwarf galaxy formation

is a very ad hoc and stochastic process. However, this impression is certainly flawed as many dwarf galaxy properties exhibit remarkable consistency.

Milky Way dwarfs appear to have a constant central mass (within 300 pc) of 10^7 $M_\odot$ over five orders of magnitude in luminosity (Strigari et al. 2008) and their mean stellar metallicity tightly correlates with their luminosity over more than three orders of magnitude (Kirby et al. 2011a). Despite their small sizes and large mass-to-light ratios, dwarf galaxies appear to lie on many of the scaling relations seen in massive galaxies (Kormendy et al. 2009; Tolstoy et al. 2009). Rather than viewing dwarf galaxies as a distinctly different mode of galaxy formation, it may well make more sense to view dwarfs as one end of a single distribution of galaxy formation. Understanding the physics that shape dwarf galaxies is partially an effort to understand a particularly inefficient mode of galaxy formation, but it also is an effort to understand how physical processes involved in galaxy formation scale across galaxy mass to produce the observed continuous evolution in galaxy properties.

1.2 A tip in the balance results in a galaxy

The competition between a variety of baryonic heating and cooling mechanisms plays an important role in regulating the gas available for star formation in galaxies. How one set of processes dominates over the other will determine a variety of galaxy properties; from this balancing act a galaxy is born. Understanding galaxy formation is therefore in part about understanding how these microphysical processes work in galaxies.

The microphysical heating and cooling mechanism at play in galaxy formation op-

erate in a non-linearly growing potential well while being perturbed by environmental effects such as ram pressure and by effects of secular evolution of massive baryonic structures such as disks and bars. As we have established, since dSphs of Local Group are observed to have large mass-to-light ratios and old stellar populations, it is likely that their evolution has been heavily influenced by heating processes that suppressed later star formation. Several heating processes at play in dwarf evolution include the metagalactic UV background during the epoch of reionization (Bullock et al. 2000; Gnedin & Kravtsov 2006), supernova feedback (Governato et al. 2010; Sawala et al. 2010) as well as local UV heating and winds from young stars.

Heating mechanisms appear to be very important in dwarfs, but understanding the cooling mechanisms that balance them is also crucial. Many of the heating processes we have outlined are a consequence of stellar evolution and are therefore correlated with the star formation rate. In low mass haloes with very low metallicities, the effect of molecular line cooling from H_2 may be an important factor in determining the star formation rate. Cosmological galaxy simulations often assume an equilibrium cooling curve for low metallicity gas, but non-equilibrium effects may also be important (Abel et al. 2002; Glover & Clark 2012b).

Reproducing the proper phase distribution of gas in the interstellar medium is quite difficult, however, modeling star formation from this medium through the creation of aggregate star particles is also quite uncertain. We see stars forming from dense molecular clouds in our own galaxy and Kennicutt (1998) has demonstrated that the star formation rate of galaxies correlates strongly with the gas surface density. Despite this observed relation, the gas density threshold for star formation is often an adjustable parameter

in cosmological galaxy simulations in part because of resolution limitations, and indeed, adjusting the star formation threshold at fixed resolution can produce very different galaxy properties (see Guedes et al. 2011). Modeling star formation from particular gas phases may also produce different behavior; Kuhlen et al. (2012) have shown that modeling star formation as dependent on the molecular gas fraction suppresses the star formation rate in low mass galaxies at high redshift. However, Glover & Clark (2012a) have argued that simply the gas density determines the star formation rate and the molecular gas fraction plays little direct role. Since many of the other uncertain subgrid processes that we have discussed (i.e. feedback) are dependent on the star formation rate, uncertainties in modeling star formation have the potential to compound themselves in a galaxy model, and in low mass dwarf galaxies where star formation and its quenching can balance so precariously, these issues may be especially important.

1.3 A testbench for galaxy formation

Many of the processes involved in the formation of dwarf galaxies operate in galaxies of all sizes, however, dwarf galaxies provide an attractive laboratory for their study since their small sizes allow simulators the ability to reach higher resolutions. High resolution is important for resolving the dense gas from which stars form and for retaining the energy in hot gas, and is therefore key to constraining the star-formation rate. High spatial resolution (of order 1 pc) is especially important in limiting diffusion from cold, high-density gas into hot, rarefied gas produced by supernova explosions (e.g, de Avillez & Mac Low 2002; Joung & Mac Low 2006). Without resolution on this scale, feedback energy is rapidly

radiated (e.g. Katz et al. 1992). Simulations of galaxy formation often compensate for this behavior by imposing feedback driven winds or by enhancing the impact of feedback heating by either distributing energy to diffuse gas phases (e.g. Springel & Hernquist 2003; Scannapieco et al. 2006) or turning off cooling for a time (Stinson et al. 2006; Governato et al. 2010). These different approaches to modeling feedback can produce different star formation histories and galaxy properties even when keeping the total amount of supernova energy the same between different model implementations (Schaye et al. 2010; Sales et al. 2010). We understand a great deal about the structure of supernova remnants from observations of nearby resolved examples (e.g. Badenes 2010), and it is possible to model the impact of supernovae in idealized simulations of the ISM (e.g, de Avillez 2000; Joung & Mac Low 2006), but how these processes depend on, and interact with, global galaxy properties to produce global behavior such as galactic winds remains an open question.

In addition to the resolution advantages inherent in simulating dwarfs, the well defined scaling relations observed in dwarf galaxy central masses and stellar metallicities provide a clear set of constraints for galaxy simulations and models. Dwarf galaxies are therefore an ideal testbench for galaxy simulation techniques, especially for techniques that model subgrid processes such as supernova feedback. Dwarf galaxy properties that are especially sensitive to supernova feedback and may be used by simulators to better constrain their models are the metallicity of stars and the duration and frequency of star formation bursts.

Several simulation models have attempted to simulate galaxies at high resolution either at high redshift or in an idealized setting. Wise et al. (2012a) simulate the high

redshift evolution of low mass halos at very high resolutions with a model that includes thermal supernova feedback as well as energy and pressure from UV radiation produced by young stars. They also explore the transition between Pop II and Pop III star formation. Hopkins et al. (2011) construct a model using an SPH code that includes energy and momentum from stellar winds, UV radiation and supernovae and has been used for very high resolution simulations of isolated disk galaxies. Agertz et al. (2013) also construct a detailed model of stellar feedback that includes momentum and energy from stellar winds, stellar UV heating and supernovae for use in simulations with moderate resolution that is notable for the completeness of it treatment and the inclusion of momentum.

For the reasons we have discussed, dwarf galaxies provide an attractive means by which to constrain high resolution galaxy simulation techniques. We should caution however that our approach should be to constrain techniques rather than to constrain the level or intensity of model parameters. Our goal is to better understand the physics responsible for the formation of dwarf galaxies. This goal would not be served by arbitrarily adjusting model parameters until the right 'fit' is found. Complex galaxy simulations of the type we will describe should not be viewed as a modeling technique with the aim of determining best fit parameters for physical prescriptions but rather as a method for differentiating between different physical prescriptions themselves.

1.4 Overview

The goal of this study is to understand the detailed physics that regulate galaxy formation in very low mass dark matter halos. We will attempt to construct a galaxy model that

is complete enough such that it includes the dominant physical effects at play in dwarf formation while being computationally light enough to be able to complete cosmological simulations within a hubble time. Chapter 2 will present a first set of cosmological galaxy models that primarily probe the dichotomy between reionization and supernova feedback in the suppression of star formation in a low mass dark matter halo. These models will also explore the effectiveness of the thermal supernova feedback model used by exploring the ways in which metals are ejected from star forming gas. Chapter 3 will explore a new model for supernova feedback that includes the injection on short timescales of kinetic energy. Chapter 4 will explore some preliminary applications of this new feedback method that will demonstrate the ways in which it can affect the star formation rate and the metallicity of the stellar component. Chapter 5 will summarize these results and discuss potential future work.

Chapter 2

Simulating Dwarf Galaxies in a Cosmological Context

In this chapter, we begin with a broad exploration of the dominant physical effects that shape the evolution of low mass dwarf galaxies. For this study, we have deliberately chosen simple and widely used prescriptions to model subgrid baryonic effects such as supernova feedback and reionization. Our goal is to test these model prescriptions at high resolution by carefully comparing our simulation results to observations. We believe that the specific ways in which our simulations succeed or fail to reproduce observations can tell us much about the ability of these model prescriptions to capture the relevant baryonic physics properly.

We will also attempt to better understand the factors that control the gas content, star formation rate, and stellar mass for Local Group dwarf analogues. We are particularly interested in probing the relative impacts of supernova feedback and reionization on the evolution of these low-mass systems. We will attempt to do this by better understanding

the detailed evolution of the gas phase distribution within a cosmological context. The simplicity of our model assumptions for subgrid baryonic physics will hopefully provide clarity in interpreting the implications of our results for the evolution of real systems.

To these ends, we have conducted a series of high resolution cosmological, hydrodynamical simulations of a single dwarf halo with prescriptions for H_2 and metal line cooling; star formation and supernova feedback; and a global UV background that ionizes neutral gas and dissociates molecules. We target a dark halo mass of 10^9 $M_\odot$, at the low-mass end of the range in dwarf galaxy halo masses. Modeling of the dynamics of Local Group dwarfs suggests they reside in dark matter haloes of approximately this mass or smaller (e.g Tollerud et al. 2011).

We describe our simulation methods and physical prescriptions in Section 2.1 and present the results of our canonical simulations in section 2.2.1. We have also conducted simulations where we have adjusted some of the physical prescriptions implementing supernova feedback and reionization to gauge their effect in our model. We present the results of these alternate physics runs in Section 2.2.2. We discuss the results of our simulations and compare our results to observations and other simulations in Section 2.3.

2.1 Methods

We conducted our simulations with the structured adaptive mesh refinement (AMR) hydrodynamics code Enzo (Bryan 1999; Norman & Bryan 1999; O'Shea et al. 2004). Enzo uses an Eulerian method for solving the hydrodynamics equations on a Cartesian grid. We chose a grid-based method because of its ability to resolve interfaces in multiphase

gas (Slyz et al. 2005; Agertz et al. 2007; Tasker et al. 2008). We used the ZEUS hydro solver in Enzo which uses a simple and robust second-order finite difference method (van Leer 1977; Stone & Norman 1992). Dark matter and stars are represented by particles, and the gravitational interactions are computed by solving the potential on the mesh (O'Shea et al. 2004). Our model also solves non-equilibrium evolution rate equations for e^-, H, H^+, He, He^+, He^{++}, H^-, H_2, and H_2^+, as well as cooling from these species (Anninos et al. 1997; Abel et al. 1997). In addition, we include metal line cooling, photoionizing and photodissociating backgrounds, star formation and thermal feedback, and self-shielding by neutral and molecular gas, which are all described in more detail below. Our version of the code is publicly available in the auto-inits branch of the online Enzo repository[1] as changeset 15651fe320ff.

2.1.1 Initial conditions

We generated cosmological initial conditions with Enzo's initial conditions generator *inits*. We used the best fit cosmological parameters from the WMAP5 data release ($\Omega_m = 0.274$, $\Omega_b = 0.0456$, $\Omega_\Lambda = 0.726$ and $h = 0.705$) (Hinshaw et al. 2009). We begin our simulations at redshift $z = 99$ when perturbations in the universe still grow linearly. Our cosmological box is 4 comoving Mpc h^{-1} on a side and is divided into 128^3 cells on the root grid. We note that our box size is too small to accurately sample large scale modes, and the largest mode in the box becomes non-linear at low redshift. This will affect the statistics of the halos in our box, and will also impact accretion at late times; however, since this is an exploratory study to understand the gross evolutionary properties of a single low mass

[1] enzo-project.org

dwarf halo, we argue that this level of error is acceptable. In particular, we note that while the accretion history of our chosen halo may be biased, it is likely to fall within the wide range of possible such histories for halos of this mass. We will redress this problem in later work.

Our goal is to simulate a single dwarf halo at high resolution. We first selected a target halo from a simulation of our cosmological box with no refinement. We identified halos close to our target mass of 10^9 $M_\odot$ at $z = 0$. We found that lower mass halos traveled a longer distance relative to their size than higher mass halos (reflecting the fact that all halos participate in large-scale bulk flows). We chose a halo that traveled a relatively small distance relative to its r_{200} radius during the simulation to minimize the area of refinement necessary in resimulations. Our chosen halo travels a distance of 0.9 comoving Mpc h^{-1} during the simulation. This choice was motivated by concern for computational efficiency, however, it had the result of selecting a relatively isolated halo. The closest halo with comparable mass to our target halo has a mass of 8.52×10^8 $M_\odot$ and is at a distance of 338 kpc, which is approximately 14 times r_{200} for our halo. The most massive halo in the box is 1.43×10^{12} $M_\odot$ and is 2.9 Mpc from our target halo.

The target halo identified, we then created new, refined initial conditions based on the trajectory of our halo and its particles. We laid down a series of nested static subgrids that refine the root grid by a total of three additional levels so that in the most refined region the effective initial resolution was 1024^3. The cell size within the most refined static subgrid before adaptive refinement is therefore 5.54 comoving kpc. One corner of the maximally refined static subgrid was defined by the target halo's final position plus a buffer of 10 r_{200} radii. The opposite corner was set to contain the volume enclosing the

initial positions of the halo's particles in the coarse simulation, plus an additional buffer of 10% of the width of this enclosing volume in each direction. A buffer region of four intermediate resolution grid cells was placed around the boundaries of each successively nested static grid. The initial resolution of a cell sets the mass of the dark matter particles laid down within it, so the higher resolution cells have lower mass dark matter particles. The buffer regions are important to ensure that higher mass particles did not impact the evolution inside the highly refined region. These initial conditions set the minimum mass of dark matter particles to be 5353 $M_{\odot}$.

To further restrict refinement to the halo of interest, we have employed a new technique that identifies dark matter particles in our refined initial conditions that end the simulation in our target halo and then requires the presence of these particles for the refinement of a given cell. We identified halo dark matter particles in our refined initial conditions by first running a dark matter only simulation to $z = 0$. We identified particles that ended the simulation within $3r_{200}$ radii of the halo centre and tagged them as 'must refine particles.' In all subsequent runs with hydrodynamics, we restrict adaptive refinement to cells that contain must refine particles and that are within the highest resolution initial subgrid. Cells meeting these criteria may be further refined based on their dark matter and baryon density such that additional refinement was added (by a factor of 2) whenever the dark matter mass in a cell exceeded four times the dark matter particle mass, with a similar criterion for the gas. We did not explicitly implement refinement based on the Jeans length, however, we found that with our density refinement criteria that in most dense regions we either resolved the Jeans length by four grid cells (meeting the criterion of Truelove et al. (1997) to avoid artificial fragmentation) or the density of the

gas was greater than our chosen threshold density for star formation. The net result of our method is that the adaptive refinement tracks the dark matter particles and gas that ends up in the halo of interest. In our highest resolution run (Simulation R10 in Table 2.1), we find that 99% of the dark matter particles within r_{200} are must refine particles at $z = 0$. This method resulted in a computational savings of more than a factor of 10, as compared to allowing refinement anywhere in the most refined initial grid, which is standard practice.

In our highest resolution simulations, we allow a total of 12 levels of adaptive refinement beyond the root grid. These simulations therefore have a minimum cell length of 10.8 comoving pc. This means at high redshift ($z \sim 9$) our calculations have a physical resolution of order one pc. We have also conducted simulation R43 that allows only 10 levels of adaptive refinement beyond the root grid for a minimum cell length of 43.3 comoving pc. We will discuss this simulation in Section 2.3.3.

2.1.2 Metal cooling

As noted earlier, we include radiative cooling from nine atomic and molecular species (Abel et al. 1997; Anninos et al. 1997), whose (non-equilibrium) abundances are explicitly followed. In addition, the code also tracks a mean metallicity, and additional metal heating and cooling rates are interpolated from equilibrium cooling tables, in a way similar to that described in Smith et al. (2008): Cloudy (Ferland et al. 1998) is used to generate five-dimensional tables that give the net metal cooling and heating rates, depending on the gas metallicity, electron fraction, density, temperature and redshift. The redshift tracks the time-dependence of the metagalactic UV background (see below). The combination of heating and cooling from non-equilibrium atomic and molecular hydrogen combined

Table 2.1 Summary of Simulations.

Name	Δx_{min} (comoving pc)	e_{SN}	Δz	H_2 Cooling	Z_{max} ($Z_\odot$)
R10	10.8	3.7×10^{-6}	7-6	yes	none
R10-earlyUV	10.8	3.7×10^{-6}	9-8.9	yes	none
R10-noH2	10.8	3.7×10^{-6}	7-6	no	none
R10-noUV	10.8	3.7×10^{-6}	none	yes	none
R10-noFB	10.8	0	7-6	yes	none
R10-noFB-LimCool	10.8	0	7-6	yes	0.1
R10-lowFB	10.8	10^{-6}	7-6	yes	none
R10-DM	10.8	-	-	-	-
R43	43.3	3.7×10^{-6}	7-6	yes	none

Note: The quantities presented in each column are (1) the minimum cell width for the calculation, (2) the fraction of rest mass energy that star particles return to the gas, (3) the redshift range over which the UV background is introduced, (4) whether the abundance of or cooling from H_2 is tracked, (5) and the maximum effective metallicity for metal cooling.

with equilibrium metal lines, allows for a more accurate estimate of the cooling rates, particularly for low metallicity gas. Since we follow the abundance of H_2, the cooling rates we compute for low temperature, low metallicity gas where H_2 cooling dominates are particularly accurate. We do not include molecular hydrogen formation on dust grains, but by the time this pathway becomes important, metal cooling dominates over H_2 cooling anyway (Glover 2003). Finally, we note that we do not include molecules formed out of heavy elements, but these tend to be less important than fine-structure lines (Glover & Clark 2012b), particularly at low abundances.

2.1.3 UV background

We include both photoionizing and photodissociating metagalactic backgrounds in our model. We assume spatially uniform photoionizing rates for H I, He I and He II that vary with redshift, taken from Haardt & Madau (2001). This background includes ionization

from both quasars and stars. For most of our runs we start turning on the photoionizing background at $z = 7$ and gradually ramp it up to full strength by $z = 6$. The photodissociation rate of H_2 is taken to be 1.13×10^{-8} times the flux in the Lyman-Werner bands (Abel et al. 1997). We adopt the average flux in the Lyman-Werner bands from the spectra of Haardt & Madau (2011). This flux is redshift dependent and we assume it to be spatially uniform. We turn on the photodissociating background at the same time as we start the photoionizing background (without a ramp-up period, as there is no significant gas heating associated with this transition). In order to investigate the impact of the timing of the reionization epoch, we also carried out a simulation in which we turned on the UV background at an earlier redshift, $z = 8.9$, and ramped up the ionizing background to full strength by redshift $z = 8$.

Although the UV background is spatially uniform, we apply a crude self-shielding correction. The H I ionizing flux felt by each cell is attenuated by a factor of $\exp(-\Delta x n_{\rm HI} \bar{\sigma}_{\rm ion})$, where Δx is the cell size, $n_{\rm HI}$ is the neutral hydrogen density, and $\bar{\sigma}_{\rm ion}$ is the frequency-averaged photoionization cross-section for H I. We computed the frequency-averaged photoionization cross-section as

$$\bar{\sigma}_{\rm ion} = \frac{\int_{\nu_0}^{\infty} \frac{4\pi J}{h\nu} \sigma \, {\rm d}\nu}{\int_{\nu_0}^{\infty} \frac{4\pi J}{h\nu} \, {\rm d}\nu}, \tag{2.1}$$

where J is the flux of the ionization background, which we approximate as $J \propto \nu^{\beta}$, and σ is the frequency dependent ionization cross-section, which is zero for frequencies less than ν_0, the threshold frequency for ionization of H I, and $\sigma \propto A_0 \nu^{-3}$ for frequencies greater than ν_0. The parameter β is the power law slope of the ionization background which we

take to be -1.57, approximately the slope of the photoionization background that we use. The parameter A_0 is the peak ionization cross-section for H I. With these assumptions we calculate the average photoionization cross-section to be $\bar{\sigma}_{\rm HI} = A_o\beta/(\beta - 3)$.

A similar correction is made for the H I photoheating rate, where we use the frequency-averaged photoheating cross-section which we compute as

$$\bar{\sigma}_{\rm heat} = \frac{\int_{\nu_0}^{\infty} \frac{4\pi J}{h\nu}(h\nu - h\nu_0)\sigma \, {\rm d}\nu}{\int_{\nu_0}^{\infty} \frac{4\pi J}{h\nu}(h\nu - h\nu_0) \, {\rm d}\nu}, \tag{2.2}$$

which we find is proportional to $\bar{\sigma}_{\rm ion}$ by a factor of $(\beta+1)/(\beta-2)$. Corrections are also made for He I and He II ionization and heating using the corresponding values of A_0 for each species taken from Brown (1971) and Osterbrock & Ferland (2006). These corrections are approximate, as they assume that only gas in the local cell contributes to self-shielding, but they do suppress ionization and heating in dense regions.

We also apply a simple self-shielding correction to the Lyman-Werner background as described in Shang et al. (2010); this uses the local H_2 densities multiplied by the local Jeans length to determine an estimate of the column density of H_2 that is shielding each cell. The simple estimate in Draine & Bertoldi (1996) is then used to compute a self-shielding correction factor. Wolcott-Green et al. (2011) have recently shown that this can result in an overestimate of the self-shielding correction for our conditions; however, given the highly uncertain level of the Lyman-Werner background, this approximation is sufficient for this work.

2.1.4 Star formation and supernova feedback

Star particles are created during the course of a simulation following the prescription of Cen & Ostriker (1992). The implementation in Enzo is described in more detail in Tasker & Bryan (2006), but we briefly outline it here. Star particles are created in a cell if its density rises above 10^5 times the universal mean density at that redshift, if the divergence of the local velocity is negative, and if the local cooling time is less than the dynamical time (or the gas temperature is less than 10^4 K). If these requirements are met, then the star formation rate is computed according to $\dot{\rho}_{\rm SFR} = \epsilon_{\rm SF}\rho_{\rm gas}/t_{\rm dyn}$, where $\epsilon_{\rm SF} = 0.01$ is the star formation efficiency (e.g. Krumholz & Tan (2007)) and $t_{\rm dyn} = (3\pi/32G\rho)^{1/2}$ is the dynamical time. A star particle is then created with mass $M_* = \dot{\rho}_{\rm SFR}\Delta t\Delta x^3$, where Δt is the timestep. To prevent very small star particle masses, a stochastic prescription is used such that star particles are not created until 100 $M_\odot$ of stars are predicted to form; once that limit is reached, a star particle of 100 $M_\odot$ is created (up to a maximum of 80% of the baryonic mass in the cell).

Once they are created, star particles return both energy and mass to their surrounding gas, also following the prescription of Cen & Ostriker (1992). Star particles return some fraction of their rest mass energy to thermal energy in the gas. We chose this value to be 3.7×10^{-6} for most of our simulations. This corresponds to 150 $M_\odot$ worth of stars to produce one supernova's worth of energy (10^{51} ergs). This energy is continuously injected as thermal energy into the gas over the feedback time t_f, which is a few dynamical times (i.e. ten Myr to a few tens of Myr) as detailed in Tasker & Bryan (2006). The energy and mass return fractions depend sensitively on assumptions regarding the IMF; the values adopted in this paper are in the ranges determined by other works (e.g. Jungwiert et al.

2001; Kroupa 2007; Oppenheimer & Davé 2008; Conroy & Gunn 2010). Note that we do vary the fraction of rest mass energy returned in feedback in order to investigate the impact this has on our results. The particle also returns 25% of its mass to the gas.

Our choice of a purely thermal feedback model is motivated by simple models of individual supernovae which show that the supernova driven Sedov blast wave reaches a radius of a few parsecs in dense gas before radiative cooling begins to slow it down and it radiates away energy (Chevalier 1974). One might expect that in a galaxy simulation with a resolution comparable to this scale, artificial radiative losses seen in previous lower resolution studies (e.g. Katz et al. 1992) would be small. In such a simulation this resolution would negate the need for artificial subgrid models necessary to compensate for this effect (e.g. turning off radiative cooling). Our main simulations have a spatial resolution of 10.8 comoving pc; therefore, for $z \geq 3$, our simulations have a spatial resolution less than 3 pc, which is the level of resolution needed to test this hypothesis. Given the observed old stellar populations found many dSphs and their small sizes, these systems are an ideal test case for this type of model run at these resolutions. We will discuss the efficacy of this model and our assumptions in Section 2.3.2.

We follow a single gas metallicity field in all our simulations, so we do not follow the detailed chemical evolution of individual metal species. The metallicity field (ρ_Z) is initialized to a low value at the beginning of the simulation (10^{-10} times the mean gas density). When star particles form, they are assigned the metal fraction ρ_Z/ρ_{gas} of their birth cell. Stars return 2% of their total mass to this metallicity field over the feedback timescale t_f using the same temporal functional form as used for the thermal feedback. During each time step, the ejected metal mass is added directly to the single cell in which

the star particle resides. The 2% metal yield we use is a fiducial value consistent with previous work (Madau et al. 1996). Uncertainties in individual stellar yields and the IMF make this value very difficult to constrain. Moreover, a more sophisticated chemical model could be employed that includes different types of supernovae with different injection timescales and chemical yields. We are interested in probing the broad effect of a using a purely thermal supernova model at high resolution in an AMR code and understanding the *relative* effects of supernovae and reionization. For these reasons we have chosen to use a simple chemical model.

2.1.5 Halo tracker and data analysis

The problem of finding and tracking inheritance between dark matter halos within cosmological simulations is not a trivial one. We used the halo finder `hop` (Eisenstein & Hut 1998) to identify halos in our simulation and a simple halo tracker to track inheritance between halos, starting with the final target halo at $z = 0$ and working backwards in time to higher redshifts. For each child halo, the tracker finds parent halos in the preceding output by identifying halos that contain dark matter particles that end up in the child halo. Parent halos that contribute more than 10% of the child halo's dark matter mass or contain more than 10^7 $M_\odot$ in dark matter mass are considered significant parents. The lineages of these significant parents are then tracked back to previous outputs in the same manner.

The ability of this simple halo tracker to separate halo lineages is limited by the ability of `hop` to separate interacting halos and by the cadence of simulation outputs. There were cases of interacting halos where `hop` was unable to properly separate halos and the halo

tracker was therefore unable to properly separate lineages containing these halos. In these cases, we present the potential lineages of interacting halos as equivalent and do not attempt to distinguish between them.

We analysed the baryon quantities of identified halos with the simulation data analysis and visualization tool yt (Turk et al. 2011). We also used yt to construct the images, phase diagrams and radial halo profiles which we present.

2.2 Results

We have run a suite of simulations of a single dark matter halo, varying the physical prescriptions outlined in Section 2.1. Table 2.1 summarizes the simulations discussed in this paper. Analysis is conducted on simulation outputs that are written every 108 Myr. Two of our runs, R10 and R10-earlyUV, include all of the physics we have described previously, but differ in the time at which the UV backgrounds are introduced. We call these two runs our canonical runs, and describe them in detail below. We have also run a simulation completely neglecting the UV backgrounds, simulation R10-noUV. This simulation, unlike our other simulations which were run to $z = 0$, was run only to $z = 3.1$. We chose to end R10-noUV at this redshift because of the copious cold, dense gas produced. This gas made the simulation run quite slowly and by redshift 3.1, the difference in evolution was clear. Simulations R10-lowFB, R10-noFB and R10-noFB-LimCool all examine the impact of changing the strength of supernova feedback. We also tested the importance of H_2 for cooling by removing it as a coolant in simulation R10-noH2. This set of simulations gives us broad levers on the relative importance of most

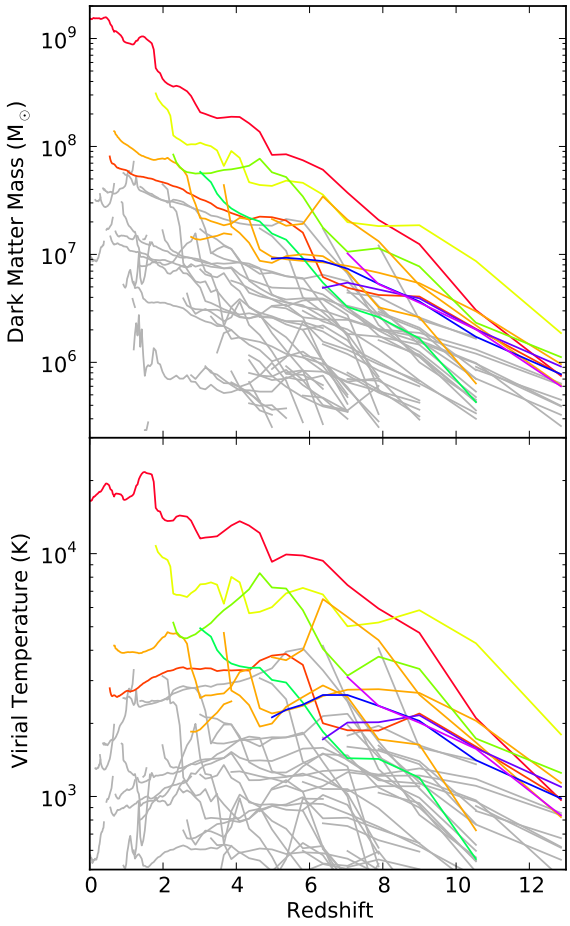

Figure 2.1 Top: Evolution of the dark matter mass within r_{200} (top) and virial temperature (bottom) of progenitor halos in simulation R10. Coloured lines indicate halos containing star particles, while gray lines indicate halos that remain dark. A line begins when a halo becomes massive enough to be detected by our halo finder and ends when the halo merges into a more massive halo. We note that substructure can occasionally separate far enough from its parent halo to be detected for a brief time as a separate halo, and therefore appears as short lines. In particular, two star forming progenitors have a series of close encounters during which our halo finder was unable to distinguish between them – their evolution is shown in orange.

of the heating and cooling effects important in dwarf formation. In particular, we aim to understand the fundamental question of how the dual effects of supernova feedback and reionization shape the baryon fractions and star formation rates of dwarf galaxies.

2.2.1 Canonical runs

In this section, we describe in detail the results of R10 and R10-earlyUV, which are the highest resolution simulations to include all of the physics outlined in Section 2.1. R10-earlyUV differs from R10 in that the uniform UV backgrounds were turned on in the same way as described in Section 2.1 but between redshifts 8 and 8.9 instead of between redshifts 6 and 7. The purpose of introducing the global UV background at different times is to explore the effect of patchy reionization. More isolated regions of the universe farther from major sources of ionizing photons may be affected by the ionizing background later than less isolated regions. In both R10 and R10-earlyUV, the universe is ionized by redshift six.

2.2.1.1 Global properties

The halo we have chosen is fairly isolated at $z = 0$; however, like all dark matter halos in cosmological simulations, it assembles hierarchically. Figure 2.1 shows the evolution of the dark matter halo masses and virial temperatures (as defined in Machacek et al. 2001) of progenitor halos in R10 and R10-earlyUV. We present the dark matter evolution only for halos in R10 since the dark matter evolution is virtually identical in R10-earlyUV. At $z = 9$, there are 30 progenitor halos more massive than 10^6 $M_\odot$. Two of these halos are more massive than 10^7 $M_\odot$, and these two halos gradually build up their mass within two

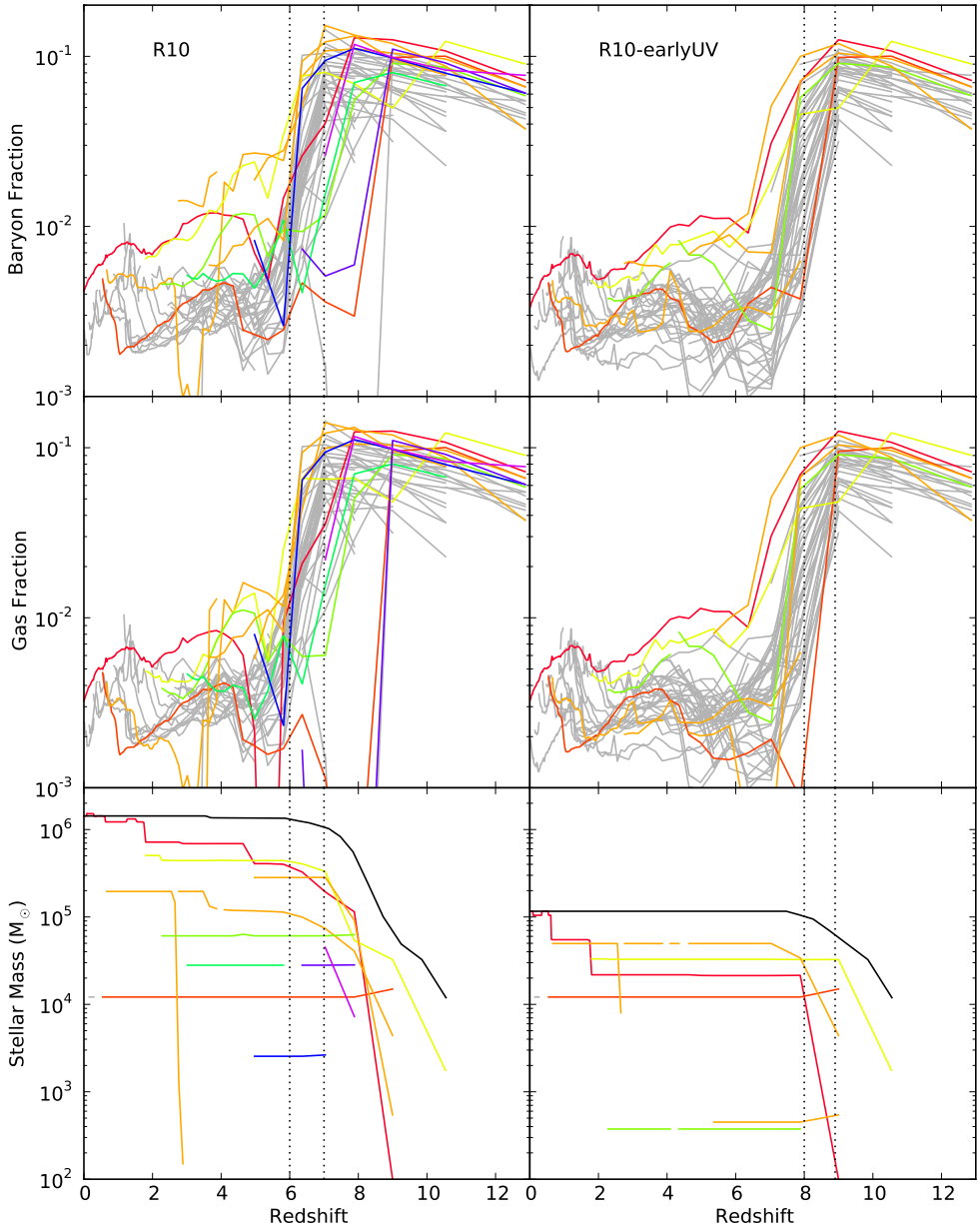

Figure 2.2 Evolution of baryon properties, within r_{200}, of progenitor halos in simulation R10 (left column) and R10-earlyUV (right column). Top row: The ratio of baryon mass to total mass. Middle row: The ratio of gas mass to total mass. Bottom row: The total stellar mass. The cumulative mass distribution of star particles that end the simulation in the final halo is shown in black. The solid line colors have the same meaning as in Figure 2.1. The dotted lines bracket the redshift range over which the photoionization background is introduced and ramped up to full strength.

groups over the course of the simulation. The two halos merge at $z = 1.8$ in a merger that is about 2:1 in dark matter and nearly 1:1 in stellar mass in both R10 and R10-earlyUV.

The evolution of a variety of baryon quantities in progenitor halos is shown in Figures 2.2 and 2.3. We track gross properties of progenitor halos in Figure 2.2 such as the total baryon fraction, gas fraction and stellar mass and quantities associated with the densest cell in each halo in Figure 2.3 such as its density and metallicity. The densest cell within each halo is the cell most likely to form star particles in our model. Given the low star formation rates expected of progenitor halos and the fact that our star formation and supernova feedback models operate on a cell-by-cell basis, the properties of the cell with the maximum likelihood of star formation can be very informative.

The evolution of the gas fraction in progenitor halos appears to be dominated by reionization. Figure 2.2 shows sharp declines in the gas and baryon fractions in both R10 and R10-earlyUV at their respective times of reionization. These declines are due to photo-evaporative outflows triggered by reionization (Barkana & Loeb 1999; Gnedin & Kravtsov 2006). We see that once the gas fraction declines during reionization, it remains suppressed for the remainder of the simulation. We see no evidence for re-accretion of gas once the main halo has been assembled at $z = 1.8$.

There are also smaller, but still significant, declines in the gas fraction prior to reionization in several luminous progenitors (Figure 2.2). These declines appear to be correlated with peaks in the star formation rate as shown in the bottom panels of Figure 2.3. Therefore, we conclude that they are primarily due to supernova feedback.

The gas fraction indicates how the bulk of the gas responds, but star formation depends on the presence of dense gas. The evolution of the density of the densest cell

in each progenitor halo shares some characteristics with the evolution of the gas fraction, but it is not identical. The peak cell density declines after reionization, but the decline is delayed relative to the declines seen in gas fraction. This is due, in part, to self-shielding from the UV background. In R10 particularly, there appears to be an extended epoch of elevated gas density in one progenitor that does not end until $z = 4$ and another progenitor is able to briefly re-cool some gas, although this dissipates by $z = 3.5$. We see that the evolution of the peak cell density tracks the star formation rate in individual halos, also shown in Figure 2.3, which is unsurprising as the presence of dense gas controls star formation in our model.

The evolution of the properties of the densest cell shown in Figure 2.3 can be quite stochastic in nature, with sharp changes especially at high redshift. These changes are due to the short timescale for cell-by-cell variations in our models. Our high spatial resolution enhances the importance of mixing to the evolution of the ISM, which likely plays a role in these variations. Also at this epoch, star-formation with accompanying supernova feedback is very important. At high redshift, regions of high gas metallicity coincide with regions of recent star formation. Over time these regions of enhanced gas metallicity expand, driven by the energy of supernovae to pollute the IGM as seen in Figure 2.4. This expansion causes the gas metallicity in the central regions where the stars are located to decline. We discuss the effectiveness of metal ejection in Section 2.3.4.

There are multiple star forming progenitor halos in both simulations; however, R10-earlyUV has fewer, due to the earlier onset of reionization. It appears that some halos which cooled later in R10 do not have time to cool before reionization occurs in R10-earlyUV. The bottom panels of Figure 2.3 show both the star formation rate inferred

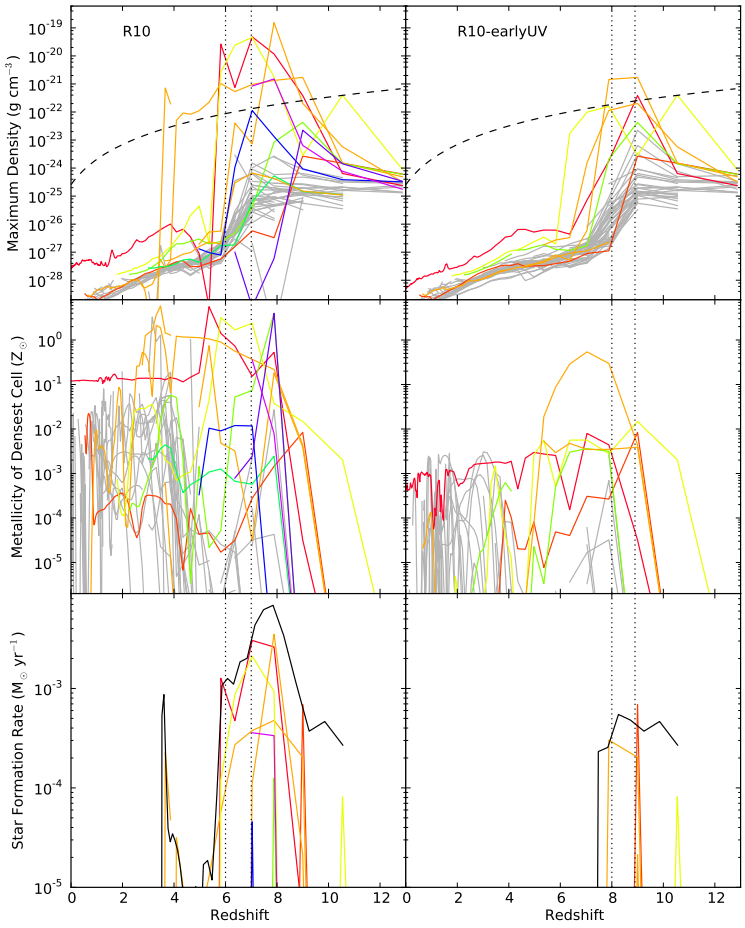

Figure 2.3 Evolution of the peak density, metallicity and star-formation rate within progenitor halos in R10 (left column) and R10-earlyUV (right column). Top row: Evolution of the maximum density within each progenitor halo. The density threshold for star formation is shown as a dashed line. Middle row: Evolution of the metallicity of the peak density cell shown in the top row. Bottom row: The star-formation rate within the last 22 Myr for each progenitor halo is plotted with color lines, while the star-formation rate inferred from the star particles that end the simulation in the final halo is shown in black. One halo in R10 (plotted in dark green) underwent a single star formation event that happens between outputs. Another halo in R10 (plotted in dark purple) accreted its stellar population through a major merger with a slightly less massive progenitor but did not form its own *in situ* stellar population before the merger. Neither halo is therefore plotted in the bottom panel. A different halo in R10-earlyUV (plotted in light green) also underwent a star formation event between outputs and is not plotted in the bottom panel. The dotted lines bracket the redshift range over which the photoionization background is introduced and ramped up to full strength.

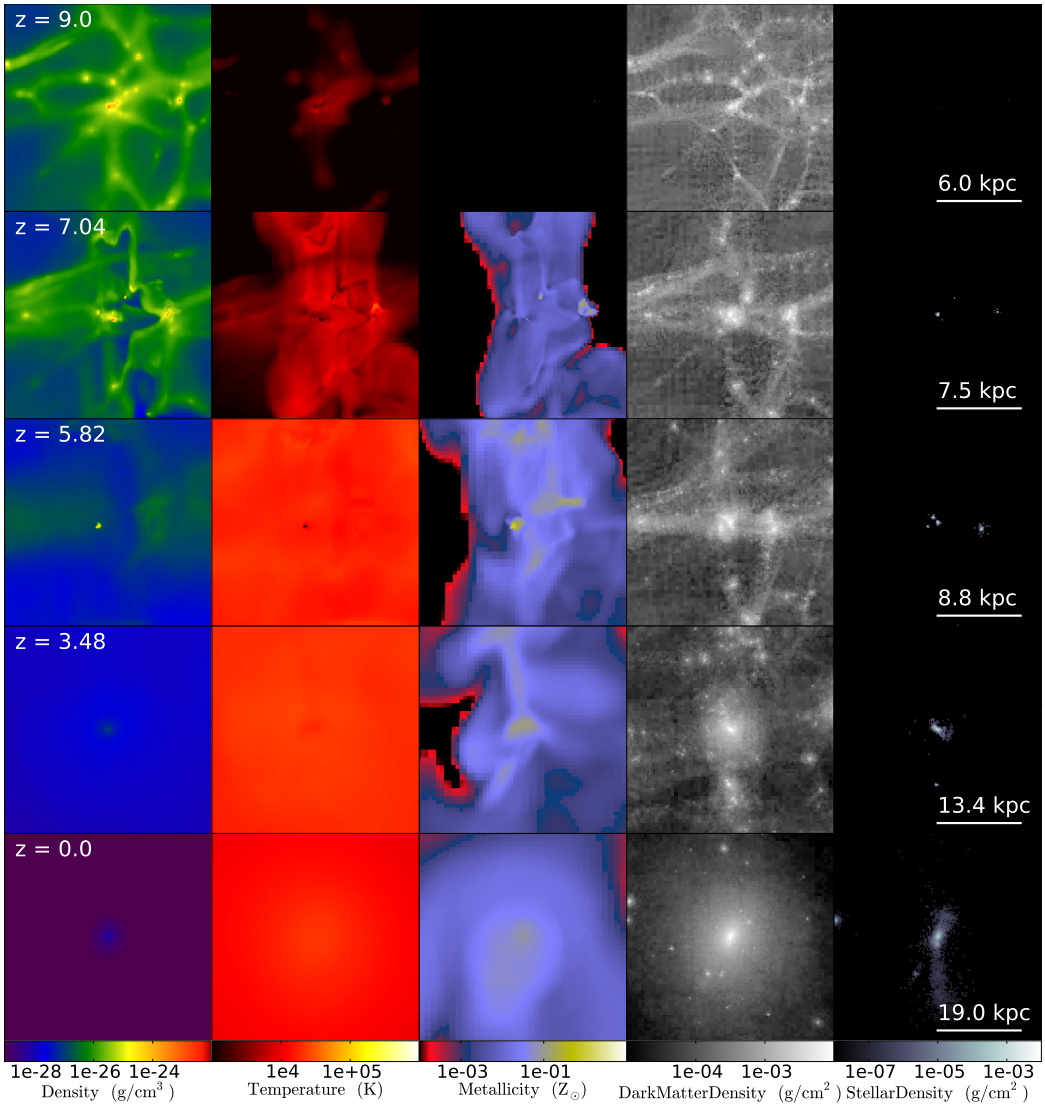

Figure 2.4 From top to bottom, cubic projections centered on a massive star-forming progenitor halo at $z = 9.0, 7.04, 5.82, 3.48$ that also show several other lower mass star-forming progenitors. The bottom row shows the final halo at $z = 0$. From left to right, the panels show projected gas density, temperature, metallicity, dark matter density, and stellar density. The panels presented in the first four rows have a comoving width of 150 kpc; the final row of projections at $z = 0$ have a width of 48 kpc, which is $2r_{200}$ for the final halo. The scale of the images in physical, non-comoving units is indicated for each redshift. At $z = 9$ the other massive star-forming progenitor is 14 physical kpc from the centered halo and is therefore not shown. Projections of gas density, temperature and metallicity are weighted by gas density and projections of dark matter density and stellar mass density are unweighted (see Equation 3 in Turk et al. (2011)). Note that this weighting scheme gives units of volume density for gas density and units of surface density for dark matter and stellar density.

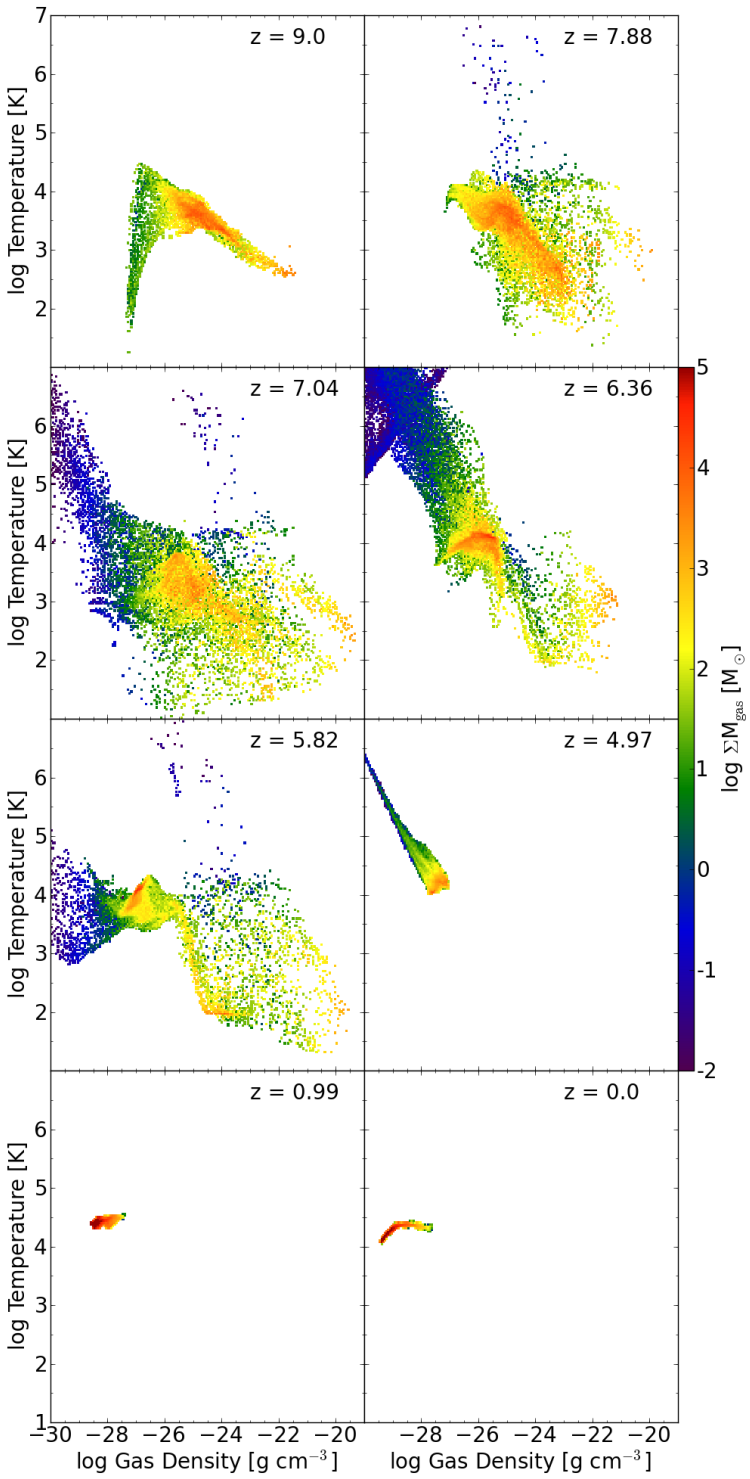

Figure 2.5 Density-temperature distributions of gas within the r_{200} radius for one of the massive halo progenitors at the redshifts shown. The color of cells shows the cumulative sum of mass within the corresponding density-temperature bin.

from the stellar population in our target halo at redshift zero, and the instantaneous star formation rates in all progenitor halos measured at each data output. The star-formation rate inferred from the stellar population at redshift zero is built up from star-formation events in multiple progenitor halos with varying durations and intensities.

Several star forming progenitors undergo star formation events that appear to be single bursts and have a duration of order of or less than the time between data outputs (108 Myrs). Three star forming progenitors in R10 and four star forming progenitors in R10-earlyUV are captured in a star-forming state in only a single data output. One progenitor in each of R10 and R10-earlyUV undergoes a star burst that occurs between outputs. The total mass in stars produced in this mode is small in R10, constituting less than 8% of the final stellar mass. In R10-earlyUV its contribution to the final (smaller) stellar mass is much greater, constituting over 57%. In R10-earlyUV there is essentially a single progenitor that has an extended period of star formation.

2.2.1.2 A detailed look at the evolutionary stages

In order to get a better qualitative understanding of how our simulated dwarf galaxy evolves, we next look at the spatial properties of the halo at various times in R10. The evolution of gross halo properties presented in Figures 2.1-2.3 can be tracked through the progression of projections presented in Figure 2.4, which are centered on one of the two massive, star-forming progenitor halos of our final halo and show its assembly at high redshift from a small group of other dwarf progenitors. We can see the spatial variations in gas density, temperature and metallicity produced by the processes of cooling, supernova feedback, reionization and self-shielding. We can also see the hierarchal build-up of both

dark matter mass and stellar mass which constitute the final halo. We can break down the evolution of this halo into a number of states described by these projections and by the density-temperature phase plots for the same progenitor halo presented in Figure 2.5.

The first stage presented is at $z = 9$ and is shown in the top left panel of Figure 2.5. We see the halo just prior to the onset of star formation. Near the virial radius the gas shock heats and creates a reservoir of gas at roughly the virial temperature of the halo. This gas can then begin to cool via H_2 cooling (e.g. Abel et al. 2002). Figure 2.1 shows the evolution of the virial temperature of many progenitor halos; prior to reionization in both the R10 and R10-earlyUV runs, all progenitor halos have virial temperatures less than 10^4 K. Therefore, for primordial gas in these halos, the only important coolant is molecular hydrogen; atomic line cooling is not significant. This stage is also shown in projections in the first row of Figure 2.4.

Eventually the gas reaches the second stage (top-right panel of Figure 2.5; $z = 7.88$) where gas temperatures in the centre fall to 200 K and gas densities cross 10^{-21} g cm^{-3}, roughly the gas density threshold for star formation in our model at high redshift. Once gas becomes dense enough to form stars in this second stage, we see evidence of supernova-heated gas with temperatures in excess of 10^6 K and the picture becomes more complex.

In the third stage (see panel labelled $z = 7.04$ in Figure 2.5), gas continues to be heated by supernovae and shows evidence of pressure equilibrium at low densities and high temperatures, as shown in the phase diagram. Also, with the injection of metals, gas can now cool to temperatures below 100 K at a broad range of densities. In some cases, the gas does appear to be significantly affected by supernova feedback in this stage. Figures 2.2 and 2.3 show the evolution of the gas fraction and the peak gas density of

many halos. Prior to reionization there are examples of decrements in both quantities, which must be due to supernova feedback. The second row in Figure 2.4 also shows this stage. We can see that, by this point, metals have been ejected from progenitor halos and have significantly enriched the intra-group medium.

After $z = 7$ (in the R10 run), the onset of photoionizing and photodissociating backgrounds causes a dramatic change in the phase structure of gas within progenitor halos. In this fourth stage (see panels labelled $z = 6.36$ and $z = 5.82$ in Figure 2.5), we see nearly all of the gas heated to a temperature of about 10^4 K. In some halos (including the one shown in Figures 2.4 and 2.5), the gas is able to remain dense or briefly recool, producing an additional wave of star formation. The third row of Figure 2.4 shows this stage. This stage does not appear in halos in R10-earlyUV and it ends in all progenitor halos in R10 by $z = 3.5$.

After this point, once the dense star-forming gas has been dissipated, a small amount of high-temperature gas persists within the supernova heated phase in a fifth stage (see panel labelled $z = 4.97$ in Figure 2.5). However, this gas phase eventually dissipates and the small amount of remaining gas sits at a temperature slightly above 10^4 K. This is both the temperature of the IGM and roughly the virial temperature of the final halo.

At low redshift (see the last two panels of Figure 2.5), a series of dry mergers continue until the final halo is assembled. The final halos that result in R10 and R10-earlyUV are gas poor spheroids of dark matter and star particles. R10 and R10-earlyUV differ in stellar mass by an order of magnitude: the halo in R10, which had a late onset of reionization, has a final stellar mass of 1.43×10^6 $M_\odot$, while the halo in R10-earlyUV, which had an earlier onset of reionization, has a final stellar mass of 1.16×10^5 $M_\odot$. Table 2.2 summarizes some

Table 2.2 Summary of Final Halo Properties.

	R10	R10-earlyUV
$M_{tot}/M_\odot$	1.55×10^9	1.55×10^9
$M_*/M_\odot$	1.43×10^6	1.16×10^5
M_{gas}/M_{tot}	3.24×10^{-3}	3.25×10^{-3}
r_{200} (kpc)	23.7	23.9
$r_{1/2}$ (pc)	704	213
$M_{1/2}/M_\odot$	3.05×10^7	3.86×10^6
$M_{300}/M_\odot$	7.53×10^6	7.41×10^6
$\sigma_{1/2}$ (km/s)	7.83	8.30
Log($\langle Z/Z_\odot \rangle$) (median)	-0.29	-1.22
Log($\langle Z/Z_\odot \rangle$) (mean)	-0.076	-0.92
$\sigma_Z/Z_\odot$	0.84	0.14

Note: The quantities presented in each row are (1) the total mass within r_{200}, (2) the total stellar mass within r_{200}, (3) the total gas fraction within r_{200}, (3) r_{200}, the radius within which the mean halo density is 200 times the critical density of the universe, (4) the radius enclosing half the stellar mass, (5) the total mass within $r_{1/2}$, (6) the total mass within 300 pc, (7) the velocity dispersion of star particles within $r_{1/2}$, (8) the mass-weighted median of the star particle metallicities, (9) the mass-weighted mean of the star particle metallicities, (10) the mass-weighted standard deviation of the star particle metallicities.

of the final halo properties in these simulations.

2.2.2 Alternate physics runs

We have also conducted a number of simulations in which we have altered some aspect of our physical prescriptions in order to better understand their effect on the evolution of the final halo. We have done simulations that have changed some aspect of the cooling prescription, the supernova feedback prescription and the UV background prescription. Table 2.1 summarizes these simulations.

2.2.2.1 Simulation without H_2 cooling

We conducted a simulation without the creation of or cooling from H_2. Simulation R10-noH2 has line cooling from six atomic species of hydrogen and helium as well as metal line cooling and heating from the Cloudy models of Smith et al. (2008). The UV backgrounds, the self-shielding by neutral gas, and the star formation and feedback models are the same as R10. This simulation produced an entirely dark halo; no star formation occurred. We found that without molecular hydrogen cooling, gas temperatures in the most massive progenitors did not fall below 500 K and densities remained below 6×10^{-24} g cm^{-3}. The peak in gas density occurred at $z = 5.8$, shortly after reionization reached full strength. Our model requires gas to be denser than 8.09×10^{-23} g cm^{-3} to form star particles at this redshift. With no initial star formation, there is no source for metals, which are the most important gas cooling agents for star formation. Once the photoionizing background is turned on, the halo gas is further heated and the gas becomes even more difficult to cool. The result is an entirely dark halo at $z = 0$.

2.2.2.2 Simulations with alternate UV backgrounds

Our canonical simulations demonstrate that the UV background has an important effect on the evolution of the halo gas. We observe that the gas fractions of progenitor halos drop dramatically at the redshift of full-strength reionization in both our early reionization simulation (R10-earlyUV) and our late reionization simulation (R10). We also observe gross differences in the properties of the final stellar component between these two simulations. The total stellar mass in the final halo differs by an order of magnitude between the two runs and the star-formation history is more bursty and truncated in R10-earlyUV.

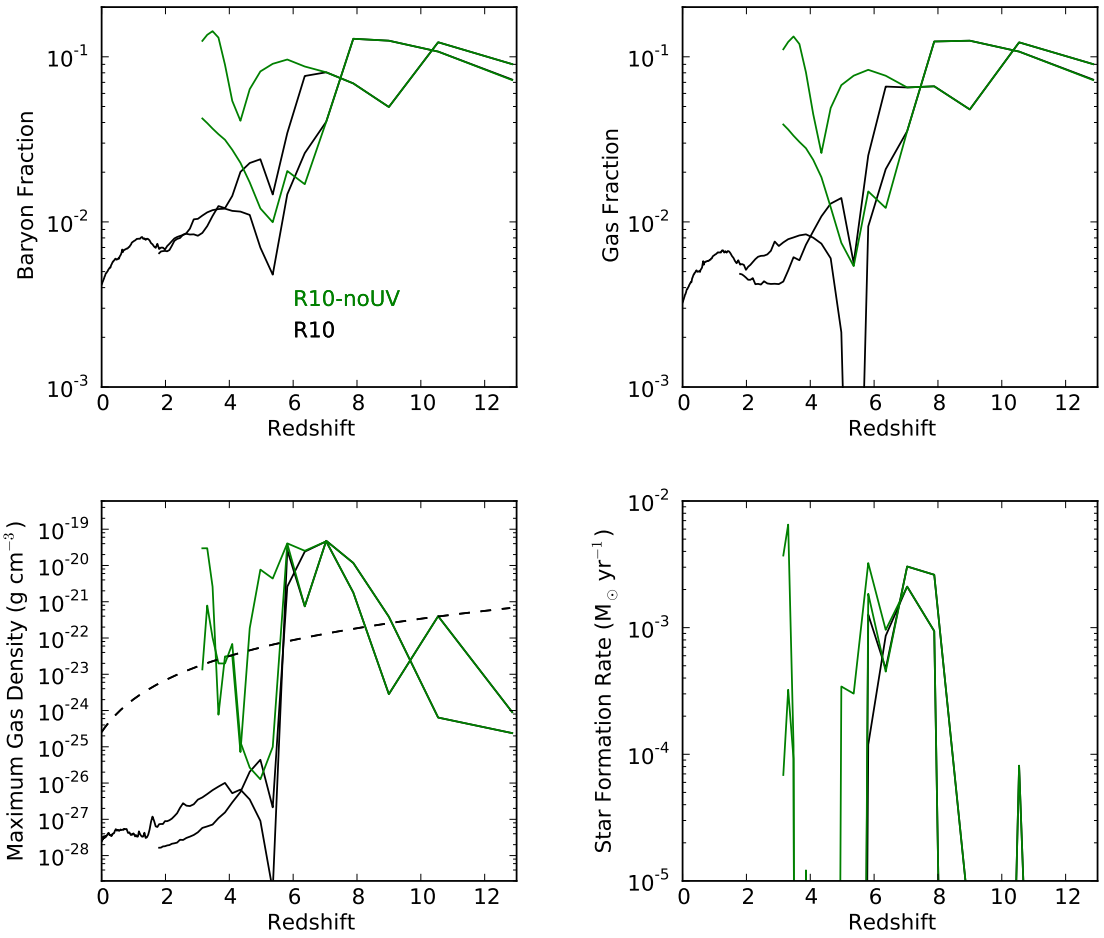

Figure 2.6 Evolution of properties for two massive progenitors in simulations R10 (black) and R10-noUV (green). R10-noUV was not run past a redshift of 3.1. The properties shown here are the halo baryon fraction within the r_{200} radius (top left); the halo gas fraction within the r_{200} radius (top right); the density of the densest cell within each halo (bottom left); and the stellar mass within the r_{200} radius for each halo (bottom right). The density threshold for star formation is shown as a dashed line in the bottom left panel showing the peak gas density.

The median stellar metallicity is much lower in R10-earlyUV (0.06 $Z_\odot$versus 0.51 $Z_\odot$), a consequence of the lack of late and extended star-formation bursts.

To further explore the effect of the UV heating on the halo's evolution, we conducted a simulation without the photoionizing and photodissociating UV fields, R10-noUV. This simulation was only run to a redshift of 3.1, but interesting comparisons can still be made. Figure 2.6 shows the evolution of a variety of gas properties for the two massive progenitors of our final halo in R10-noUV (we show only two halos for clarity). There are some striking similarities and differences in the evolution of these halos between R10 and R10-noUV. We see dips in the gas fractions of halos in R10-noUV, some quite dramatic, but the gas fraction is able to rebound in both massive progenitors. By $z = 3.1$, when we stop R10-noUV, there is an order of magnitude difference in baryon and gas fractions for both halos between the two simulations. The baryon fraction in one halo has rebounded to its level at $z = 12$.

The dense gas exhibits similar behavior. The peak gas density does drop considerably between redshifts of 6 and 4, but the gas is able to re-cool and condense to a level where it is able to form stars. This produces an uptick in the star formation rate and several halos are forming stars at $z = 3.1$ when the simulation was ended.

The dips seen in the gas fraction and peak gas density in R10-noUV are most likely due to the effect of supernova feedback. In the absence of UV heating, supernovae act as the main regulator of the star formation rate in this run. The degree of supernova heating scales with the star formation rate and once the rate drops, gas is able to both re-accrete onto the halo and re-cool in its centre. This produces an increase in the star formation rate. We did not run this simulation beyond $z = 3.1$, so it is impossible to say whether

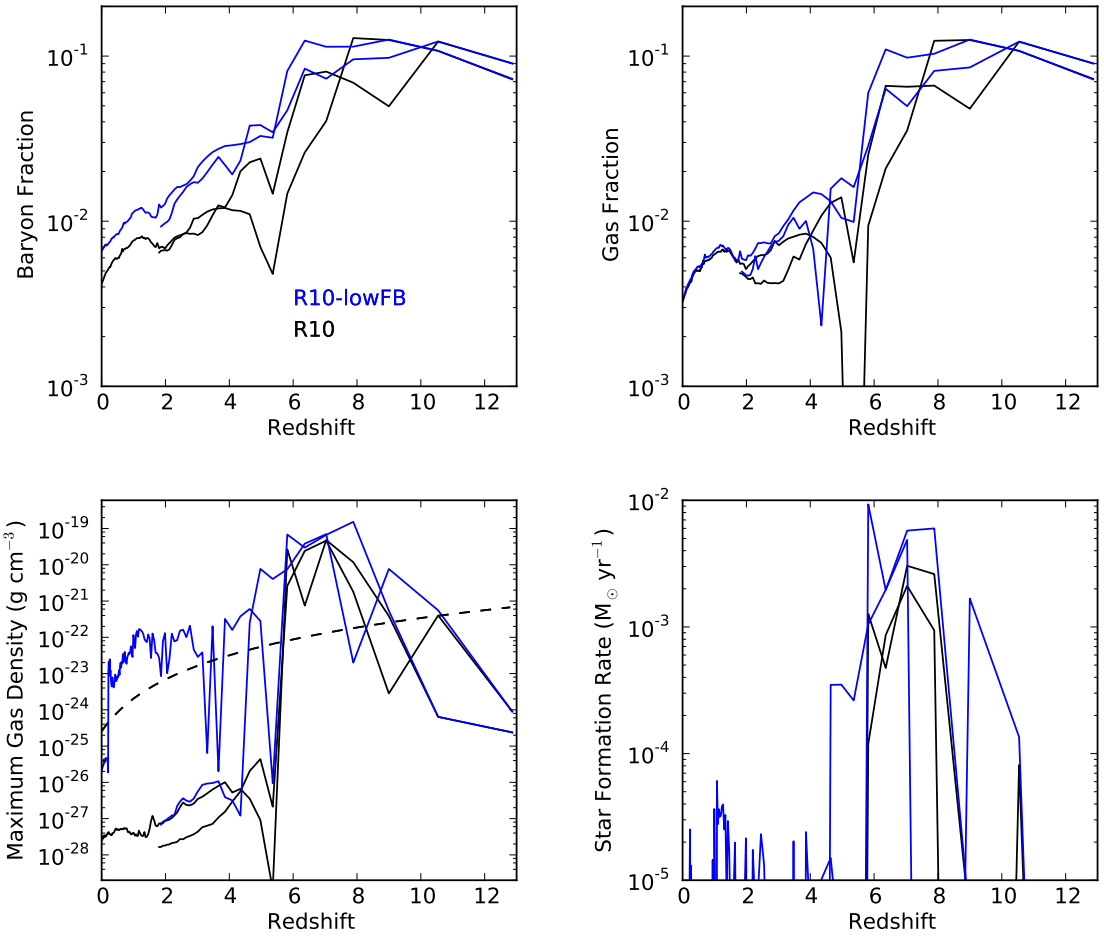

Figure 2.7 Evolution of properties for two massive progenitors in simulations R10 (black) and R10-lowFB (blue). The properties depicted are the same as those shown in Figure 2.6.

this cyclical process will continue or whether the constant bursts of star formation will produce an overall net decline in the gas fraction or peak gas density.

These simulations indicate that the UV background plays a crucial role in regulating the gas fractions of the progenitor halos. In our model, it produces a sharp drop in the gas fraction in all halos. This drop leaves an imprint on the star formation history inferred from the final stellar population of our target halo (the solid black lines in the bottom two panels of Figure 2.3). This imprint is particularly evident because our UV backgrounds

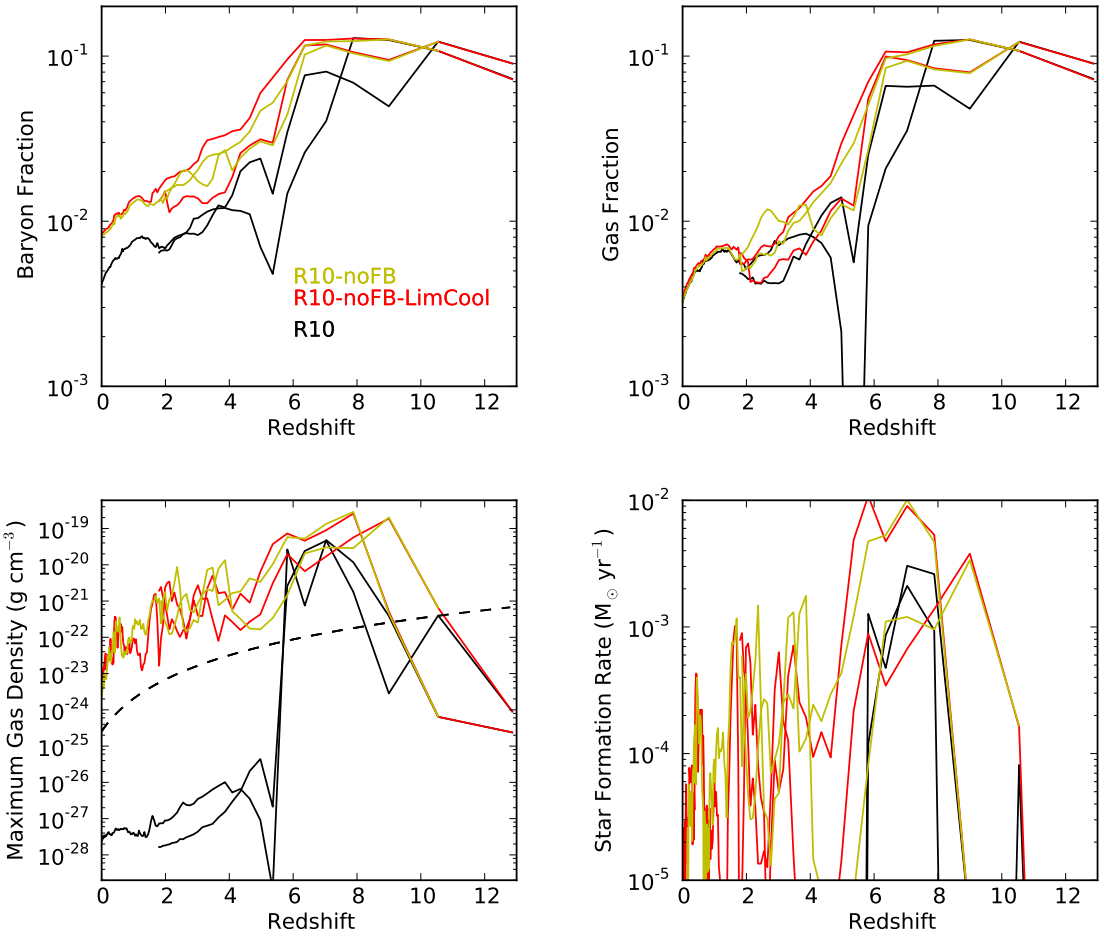

Figure 2.8 Evolution of properties for two massive progenitors in simulations R10 (black), R10-noFB (yellow) and R10-noFB-LimCool(red). The properties depicted are the same as those shown in Figure 2.6.

are spatially uniform, so all progenitors are affected with the same level of flux, and all the progenitor halos are in the mass range sensitive to the UV backgrounds.

2.2.2.3 Simulations with alternate supernova feedback levels

We also conducted three simulations exploring the effect of changing the strength of supernova feedback in our model. In most of our simulations, including R10, star particles

return 3.7×10^{-6} of their rest mass energy to thermal gas energy. In simulation R10-lowFB, we have set this fraction to be 10^{-6}. In simulations R10-noFB and R10-noFB-LimCool, star particles return zero thermal energy to the gas through supernovae, however, star particles do return metals to the gas in the same way as in R10 and R10-lowFB.

Properties for the two most massive progenitor halos in simulation R10-lowFB are shown in Figure 2.7. The gas fractions for these two halos behave in nearly the same fashion as they do in simulation R10. There appear to be smaller declines in the gas fraction prior to $z = 6$, which must be due to the reduced impact of supernova heating. Curiously, while the gas fraction declines in the same way and to the same levels as in R10, the peak gas density within each halo behaves differently. There are sharp declines in the peak gas density between redshifts 6 and 4, but the peak gas density is then able to rise significantly in one of the progenitors, up to the level required for star formation.

This difference in the evolution of dense gas results in steady, low-level star formation in R10-lowFB down to low redshift, unlike in R10. The final stellar mass in R10-lowFB is 5.03×10^6 $M_\odot$, almost five times the stellar mass found in R10. The stellar component is also more metal rich than in R10: the log of the mean and median stellar metallicities is 0.30 and 0.10 respectively, more than 0.4 dex higher than in R10. The longer star formation history, higher stellar mass and higher stellar metallicities are due to the decreased ability of supernova feedback to destroy self-shielded clumps and drive metals from star-forming gas in this simulation.

Star particles in our model impact the thermal state of the gas in two ways: first, by heating it through supernova feedback, and second, by injecting metals that act as coolants. In simulations R10-noFB and R10-noFB-LimCool we have completely eliminated thermal

feedback while maintaining the metal feedback. Unsurprisingly, we see metals collecting in the centres of halos to a much greater degree than in R10, making it unclear if changes in the no-feedback runs are due to a lack of energetic input, or an increase in the metal cooling rate.

To differentiate between these causes, in run R10-noFB-LimCool we capped the effective metallicity used for cooling at 0.1 $Z_{\odot}$. Figure 2.8 shows that the differences between R10-noFB and R10-noFB-LimCool are minimal; therefore the differences seen between these two simulations and R10 are due to a lack of heating by supernovae, not to enhanced cooling from the collected metals.

The gas fractions of halos in R10-noFB and R10-noFB-LimCool decline in almost the same way as in R10 after the introduction of the UV fields. They are slightly elevated down to $z \sim 2$, as compared to the gas fractions in R10, but this may be due to their higher gas fractions at $z = 6$ when the ionizing background reaches its full strength. As in R10-lowFB, the overall decline in the gas fraction does not correlate with an overall decline in the peak gas density. The peak gas density in both massive progenitors dips at $z = 6$, but it does not fall below the threshold density for star formation, and we see that a low level of star formation persists in both progenitors down to $z = 0$.

In all four simulations that explore different levels of supernova feedback (R10, R10-lowFB, R10-noFB and R10-noFB-LimCool), the final gas fraction is extremely low and virtually identical. Comparing these results with those from R10-noUV, we can conclude that the factor that mainly determines the gas fraction of the halo is the UV background. Supernova feedback does play an important role in regulating the dense gas component, from which stars are formed. UV heating can produce an initial, sharp suppression of the

peak gas density, however it is supernova heating that appears to determine whether it remains suppressed.

2.3 Discussion

We have explored a variety of physical effects in a series of high-resolution, hydrodynamical, cosmological simulations. Our goals were to better understand the physics that regulate star formation in a dwarf halo comparable in mass to the dwarf satellite galaxies seen in the Local Group, as well as to test current feedback models in such systems. We found that the combination of supernova feedback and reionization causes a large suppression of the star formation rates in these halos. Reionization appears to regulate the overall gas budget within the halo. Supernova feedback seems to more directly affect the dense gas that is available for star formation. Of course, these heating sources are not strictly exclusive in their effects; supernova feedback can have a quasi-periodic effect on the gas fraction and reionization can cause a dip in the peak gas density. However, the quantities affected are typically able to recover in the absence of their primary regulator.

The reason for this dichotomy between reionization and supernova feedback is primarily their different physical locations within the halo. The UV backgrounds we implement are uniform and are attenuated by our self-shielding prescriptions in dense gas at halo centres. At the onset of reionization, the ionizing background is able to produce a pressure imbalance nearly everywhere in the halo except the very centre. A large fraction of gas is therefore driven out of the halo in photoevaporative winds, while the central dense gas can remain intact for some time (Alvarez et al. 2006; Gnedin & Kravtsov 2006;

Whalen et al. 2008)

Thermal energy from supernova feedback is only injected into the single cell containing a young star particle in our model. Since the star particles tend to form and remain centrally located in halos throughout the simulation, the energy they inject tends to affect central dense gas. We do see evidence that supernovae in our model affect regions outside the central dense gas in the form of supernovae driven outflows which enrich the IGM with metals, as seen in Figure 2.4 and discussed more below. It is unclear, however, to what extent our supernova feedback model accurately captures the heating of the ISM. While the simulations that we have run with little or no thermal feedback seem to indicate that our feedback prescription is key in expelling dense gas and truncating the star formation history, we will explore this issue in more detail later in this section.

In the following sections, we will first compare our results to observed properties of low mass dwarf systems, then we will examine the effect of supernova heating in more detail, followed by discussions of spatial resolution and metal dispersal, and ending with a discussion dark matter properties and neglected physics.

2.3.1 Observable properties

In this section we compare our models to observations of several types of low-luminosity dwarf galaxies. This comparison is important because understanding the ways in which our simulations fail to produce realistic galaxies can provide important insights into the specific ways in which our model prescriptions fail. We can consider two classes of dwarf galaxies for comparison: mass analogues and environmental analogues. Our simulated halos have stellar masses and velocity dispersions similar to those of dSphs found near

the Milky Way. Unfortunately, their proximity to a large galaxy does not make them suitable environmental analogues; our simulated halo is 2.9 Mpc from a Milky Way sized halo. Dwarf galaxies have been observed in underdense environments, however, most of these are dIrrs that are more luminous than both the typical Milky Way dSphs and our simulated halos (Weisz et al. 2011b). A handful of dSphs are known in low-density environments (e.g. Makarov et al. 2012), however while some of these systems may be relics of reionization (Monelli et al. 2010), others likely underwent pericentric passages with a large host galaxy (Teyssier et al. 2012). Many of the lowest luminosity dwarfs discovered around the Milky Way have been found in the SDSS, for which the distance limit for detection has been demonstrated to be less than the Milky Way virial radius (Koposov et al. 2008). It is therefore possible that similar low-luminosity dwarfs await detection at greater distances in low-density environments.

As shown in Table 2.2, our canonical simulations R10 and R10-earlyUV produce final halos with dynamical masses within 300 pc close to 10^7 $M_\odot$, similar to those derived for Milky Way dSphs (Strigari et al. 2008). The final velocity dispersion of star particles within the radius enclosing half the stellar mass, $r_{1/2}$, is roughly 8 km s^{-1} in both simulations, making them dynamical analogues of Milky Way dSphs as shown in Figure 2.9. In the following subsections we discuss other observational comparisons.

2.3.1.1 Total stellar mass

The final stellar masses produced in our simulated halo are 1.43×10^6 $M_\odot$ in R10 and 1.16×10^5 $M_\odot$ in R10-earlyUV. Assuming a stellar mass-to-light ratio in the V band of 2 $M_\odot/L_\odot$ for our (old) stellar population (Kruijssen & Mieske 2009), the halos in R10 and

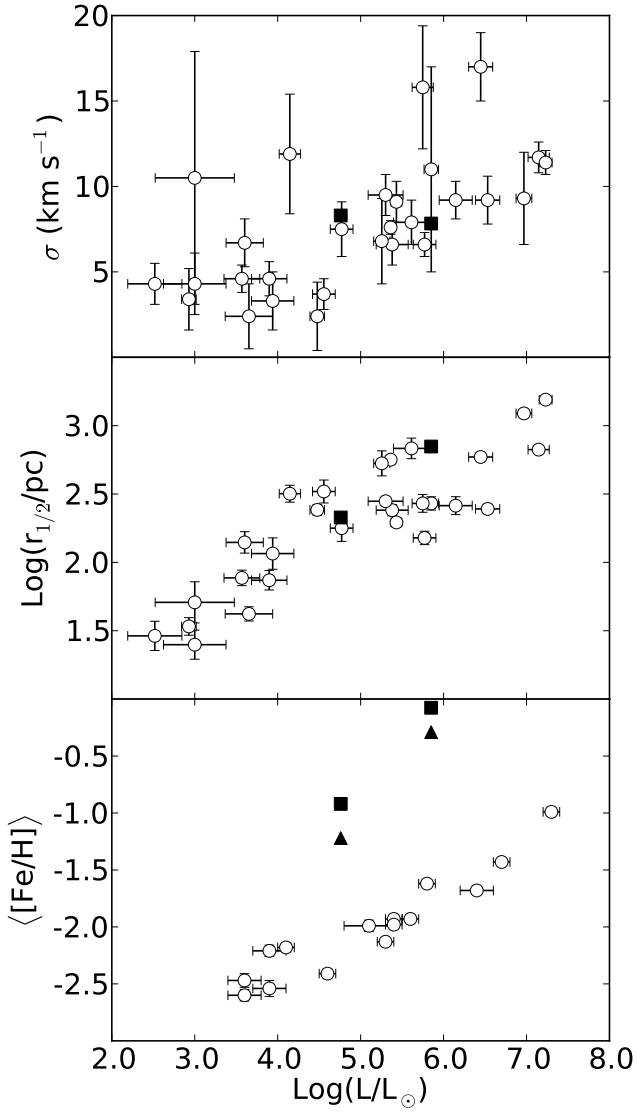

Figure 2.9 Comparison between the observational properties of Local Group dSphs and the simulated properties of the final halos produced in R10 and R10-earlyUV. All quantities are plotted against total V band luminosity. V band luminosities are estimated for our simulated halos as described in section 2.3.1.1. *Top panel:* Velocity dispersions for 28 Local Group dSphs collected by Walker et al. (2009b)[2], but including the velocity dispersion for the dynamically cold component of Bootes I measured by Koposov et al. (2011) (open circles); and the three-dimensional velocity dispersions of star particles within the half-stellar mass radii of R10 and R10-earlyUV (solid squares). *Middle panel:* The half-light radii for the same sample of dSphs (open circles) and the half stellar mass radii for the final halos in R10 and R10-earlyUV (solid squares). *Bottom panel:* The mean stellar metallicities for 15 Milky Way dSphs measured by Kirby et al. (2008) and Kirby et al. (2011a) (open circles), the mean (solid squares) and median (solid triangles) star particle metallicities for the final halos in R10 and R10-earlyUV.

R10-earlyUV would have V band luminosities of approximately 7.15×10^5 $L_\odot$ and 5.8×10^4 $L_\odot$ respectively. These estimates place the halo in R10-earlyUV at the upper luminosity end of the ultrafaint dSphs and R10 among the lower luminosity classical dSphs (Walker et al. 2009b; Simon & Geha 2007), as shown in Figure 2.9. If we compare our estimated luminosities to the halos' total gravitational masses, these halos have mass-to-light ratios within $r_{1/2}$ (the radius enclosing half the stellar mass) of 85 $M_\odot/L_\odot$ for R10 and 133 $M_\odot/L_\odot$ for R10-earlyUV. The spatial extent of the final stellar component is also comparable to real systems; Figure 2.9 shows that the half stellar mass radii for the final halos in R10 and R10-earlyUV are similar to the half-light radii of dSphs with similar luminosities.

In other highly resolved cosmological calculations of low-mass dwarf halos, the total stellar mass is generally similar to what we have found. Sawala et al. (2010) found, for their highest resolution model of a similar halo mass, a simulated stellar mass of 7.35×10^6 $M_\odot$. Recent work by Governato et al. (2012) also probed halo masses close to 10^9 $M_\odot$, and while the stellar content is not the focus of their study, their models appear to produce only $\sim 5 \times 10^4$ $M_\odot$ of star particles for halos close to this mass. One of the many differences between these two studies is the time of reionization; Sawala et al. (2010) reionize the universe at $z \sim 6$ and Governato et al. (2012) do so much earlier at $z \sim 9$. Considering this, the results of Sawala et al. (2010) are most analogous to our simulation R10, which has a final stellar mass of 1.43×10^6 $M_\odot$, and the results of Governato et al. (2012) are most analogous to simulation R10-earlyUV which has a final stellar mass of 1.16×10^5 $M_\odot$. In

[2]These data were taken by Irwin & Hatzidimitriou (1995); Walker et al. (2009c); Martin et al. (2008); Walker et al. (2007); Mateo et al. (2008); Koch et al. (2007); Martin et al. (2007); Koch et al. (2009); Simon & Geha (2007); Adén et al. (2009); Belokurov et al. (2008); Walker et al. (2009a); Irwin et al. (2007); Geha et al. (2009); Belokurov et al. (2009); McConnachie & Irwin (2006); Côté et al. (1999); Chapman et al. (2005); Ibata et al. (2007); Letarte et al. (2009); Lewis et al. (2007); Ibata et al. (2007); Majewski et al. (2003); Saviane et al. (1996); Fraternali et al. (2009)

this light, these results appear to be roughly consistent with each other (and with the idea that later reionization leads to larger stellar masses), although differences in final stellar mass between analogous halos can approach an order of magnitude.

2.3.1.2 Metallicity

Milky Way dwarfs are observed to lie on a fairly tight luminosity-metallicity relation (Kirby et al. 2011a), shown in Figure 2.9, which may extend beyond the Milky Way (Kirby et al. 2012). Figure 2.9 shows the metallicity-luminosity relation found for Milky Way dSphs. Star particles in R10 have a mean metallicity of 0.84 $Z_\odot$ and a median metallicity of 0.51 $Z_\odot$; in R10-earlyUV they have a mean metallicity of 0.12 $Z_\odot$ and a median metallicity of 0.06 $Z_\odot$. If we make the estimate that [Fe/H] $\sim \log(Z/Z_\odot)$ (e.g. Woo et al. 2008), then these values translate to mean and median [Fe/H] values of -0.076 and -0.29 dex for R10 and mean and median [Fe/H] values of -0.92 and -1.2 dex for R10-earlyUV. Our assumption that [Fe/H] $\sim \log(Z/Z_\odot)$ is a somewhat flawed one given the short duration of star formation in our progenitor halos, and the fact that we do not properly model contributions from SNIa. We would expect this short duration to result in elevated values of [α/Fe] for their stellar populations (Tinsley 1979). This has the potential to decrease our estimated [Fe/H] by a few fractions of a dex, but we are interested in understanding differences in [Fe/H] of a dex or more.

Based on our estimated luminosities calculated in Section 2.3.1.1 and according to the dSph luminosity-metallicity relation of Kirby et al. (2011a), star particles in the final halo in R10 should have an average [Fe/H] of -1.76 dex (1.7×10^{-2} $Z_\odot$) and -2.09 dex (8.1×10^{-3} $Z_\odot$) in R10-earlyUV. Figure 2.9 shows this discrepancy, which is over 1.5 dex for R10 and

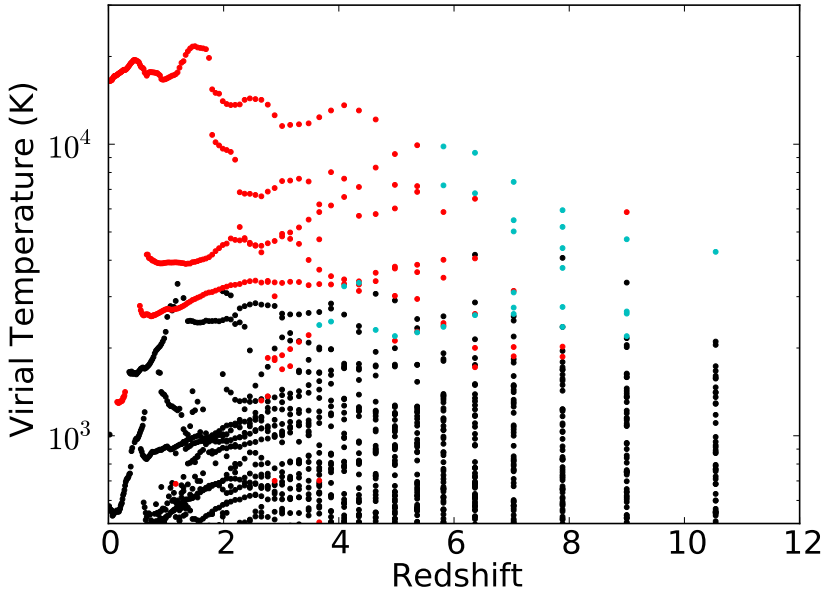

Figure 2.10 Virial temperature versus redshift for progenitor halos that are constituted of at least 50% final target halo dark matter particles. Haloes plotted in black contain no star particles; halos plotted in cyan have formed star particles within the last 20 Myrs; and halos plotted in red contain star particles, but have not formed star particles within the last 20 Myrs.

over 1 dex for R10-earlyUV. This 1-2 dex difference between observed systems and our simulations has important implications for the utility of the feedback model we use. It appears that while our adopted feedback model effectively suppresses the formation of dense gas and stars, it does not drive sufficient metal ejection from the ISM.

2.3.1.3 Gas content and star formation history

Our simulated halo in R10 and R10-earlyUV, has a final gas fraction that is very suppressed; the total mass in gas is less than 1% of the total halo mass, well below the cosmic baryon fraction (see Table 2.2). As we have discussed in Section 2.2.1.2, this remaining halo gas is very diffuse and highly ionized with a temperature of a few factors of 10^4 K (see the $z = 0$

panel of Figure 2.5) and would not be directly observable in a real system.

Many low-luminosity dSphs in the Milky Way are very gas poor with little or no H I, but (unlike our simulated system) some of the more distant Milky Way dwarfs can be quite H I rich, for example Leo T (Ryan-Weber et al. 2008). Our simulated halo is isolated and has had no interactions with the hot halo of a massive galaxy during its formation. We might, therefore, expect it to be more analogous in its gas content to the more distant Local Group dwarfs. The observed strong correlation between environment and gas content for Local Group dwarfs (Grcevich & Putman 2009) suggests that their gas content may be due to environmental effects, which this study does not explore since we only simulate one environment.

Reionization appears to be the mechanism that removes most of the gas mass in our models and the only simulation with evidence for late time gas accretion is R10-noUV, which had no UV background. From this simulation, we conclude that the lack of reaccretion of gas onto our simulated halo is due to its low virial temperature relative to the warm temperature of the IGM after reionization, a consequence of the halo's low mass ($T_{vir} \propto M^{2/3}$). It does not appear that supernovae are a factor in preventing the reaccretion of gas, as the suppression of gas fractions is remarkably similar in our simulations with different levels of supernova feedback.

Figure 2.10 shows that at late times the main progenitor halos and massive subhalos in R10 all have virial temperatures well below the temperature of the IGM (a few factors of 10^4 K). This plot also shows that, prior to reionization, with a few exceptions, progenitor halos generally need to have virial temperatures above 2000 K in order to form stars, due to the inefficiency of H_2 cooling, see Tegmark et al. (1997). After reionization, most

progenitor halos stop forming stars. As we discussed in Section 2.2, this suppression of star formation was due to a combination of the large scale photoevaporation of gas from progenitor halos and the effect of supernova heating on the remaining self-shielded clumps of dense gas. The net effect is consistent with the idea that reionization introduces a filtering mass or filtering virial temperature, below which star formation is truncated (e.g. Gnedin 2000).

Observations of dwarfs in the present epoch cannot tell us the complete evolution of gas in these systems, but their star formation histories derived from color-magnitude diagrams do give us the history of dense star-forming gas. We find that our simulated star formation histories in R10 and R10-earlyUV are sharply truncated after reionization. R10 has the most extended star formation history; however, all star formation in this model ends by a redshift of 3.5. Milky Way dSphs that are closest in luminosity to R10 and R10-earlyUV have a range of velocity dispersions and star formation histories. In general, the most truncated star formation histories tend to be found in systems with the lowest velocity dispersions (~ 3 km s^{-1}) (Brown et al. 2012), although recent analysis suggests at least one system with a luminosity and velocity dispersion comparable to our simulated halos, Canes Venatici I, has only ancient stellar populations (Okamoto et al. 2012). In general, however, most of the Milky Way dwarfs contain some intermediate-age stellar population (Tolstoy et al. 2009) which we do not see in our simulations.

2.3.1.4 Implications of observational comparisons

Given the difficulties in determining the correct observational comparison sample as discussed in the first paragraph of this section, what can we conclude about the discrepancies

between our simulated halos and observed Local Group dwarf systems, especially in regards to the lack of an intermediate age (i.e. 1-8 Gyr old, see Tolstoy et al. (2009)) stellar population? The star-forming state of our simulation appears to be heavily dependent on the metagalactic UV background we implement and this is relatively well understood for $z < 6$. The lack of dense, star-forming gas in our simulations at late times implies one of four things: one, either the implementations of the metagalactic UV background or the local shielding are inadequate and a larger reservoir of gas should survive reionization in these systems; two, our supernova feedback prescription is too effective in destroying dense gas that survives reionization; three, the handful of gas rich, but low luminosity, dwarfs (such as Leo T) observed at large galactic radii have virial temperatures above that of the IGM (and above the halo we simulate) which allows them to accrete gas at late times; or four, our halo merger tree is atypical for this halo mass or is atypical for dwarfs that end up in dense environments.

The first scenario is possible and more sophisticated methods may be used to simulate ionization and shielding, as we will discuss in Section 2.3.6. However, self-shielding would have to be many times more effective than in our current model to significantly impact the gas fractions. The second scenario also seems unlikely, since the discrepancy in stellar metallicity between our simulations and observed systems indicates that our feedback prescription is not effective *enough*. Indeed, in R10-lowFB, we found with weaker thermal feedback that star formation did continue down to low redshift, but star particles were even more metal rich. If the third scenario is true, then we would predict undiscovered dwarfs with the luminosities, star formation histories and gas content similar to Milky Way dSphs in the field. The fourth possibility is that our halo merger tree is different

from dwarfs found in denser environments. Although we do not study this directly, this possibility is plausible. It is certainly the case that the typical mass of progenitor halos at the time of reionization greatly impacts the final properties of the system and this typical mass may be different for different merger histories. It is interesting to note, however, that analysis of more isolated, but more luminous, dwarfs in the local volume indicates general consistency in star formation histories between these systems and Milky Way dwarfs (Weisz et al. 2011a)

2.3.2 Supernova feedback model

In this sub-section, we first compare suppression of star formation due to supernova feedback in our simulations to previous work. Then we explore the effectiveness of our model with simple analytic arguments, and finally suggest improvements.

Our supernova model involves a simple injection of thermal energy into the ISM over a few dynamical times. For our canonical models we chose the level of thermal energy to inject into the gas to be 10^{51} ergs per 150 $M_\odot$ of star particles. As discussed in Section 2.2.2.3, we find that lowering the feedback energy, as in simulations R10-lowFB, produces a more extended star formation history with star formation continuing past $z = 1$. The suppressed star formation histories in R10 and R10-noUV are generally consistent with other cosmological simulations probing halo masses of 10^9 $M_\odot$. Governato et al. (2012) found star formation to be strongly suppressed in halos with viral temperatures below that of the IGM and did not see the formation of central dark matter cores in halos of this mass, which were produced in higher mass halos by repeated starbursts extending down to late times. Sawala et al. (2010) found star formation lasted approximately 2.62 Gyrs

in their highest resolution simulation closest in mass to our simulated halo, a somewhat longer star formation epoch than found in R10.

While a lower level of energy conversion may be indicated by the lack of late time star formation in our simulated halo, the metallicity of the star particles produced in R10 and R10-earlyUV exceeds that observed, arguing in the opposite direction. To better understand how supernova heating occurs in our model, we examine heating and cooling timescales for each cell. We estimate the heating time of a cell to be the ratio of the cell's thermal energy to the average supernova heating rate, assuming that exactly one star particle is heating that cell, spread out over the typical timescale we adopt in the code:

$$t_{heat} = \frac{3}{2}\frac{m_{cell}kT_{cell}}{\mu_{cell}m_H}\frac{t_f}{e_{SN}M_*c^2}, \tag{2.3}$$

where $e_{SN} = 3.7 \times 10^{-6}$ is the fraction of its rest mass energy a star particle returns to the gas; t_f is the time over which a star particle returns its supernova energy to the ISM in our model, which we take to be 10 Myr; and $M_* = 100$ $M_\odot$, a typical star particle mass in our simulations. We computed t_{heat} for every cell within r_{200} and compare it to the cooling time of that cell in Figure 2.11, computed at $z = 7.04$. To be clear, the cells for which we have estimated this heating time are not necessarily being heated by a star particle at the time shown; we are simply estimating a timescale for the response to such heating.

From Figure 2.11, we see that for nearly all of the cells within the halo, the cooling time far exceeds the potential heating time. However, we see that gas with the shortest cooling times lies along the line where heating time equals cooling time. This gas is most likely the star forming gas since star particles tend to form in cells with lower cooling

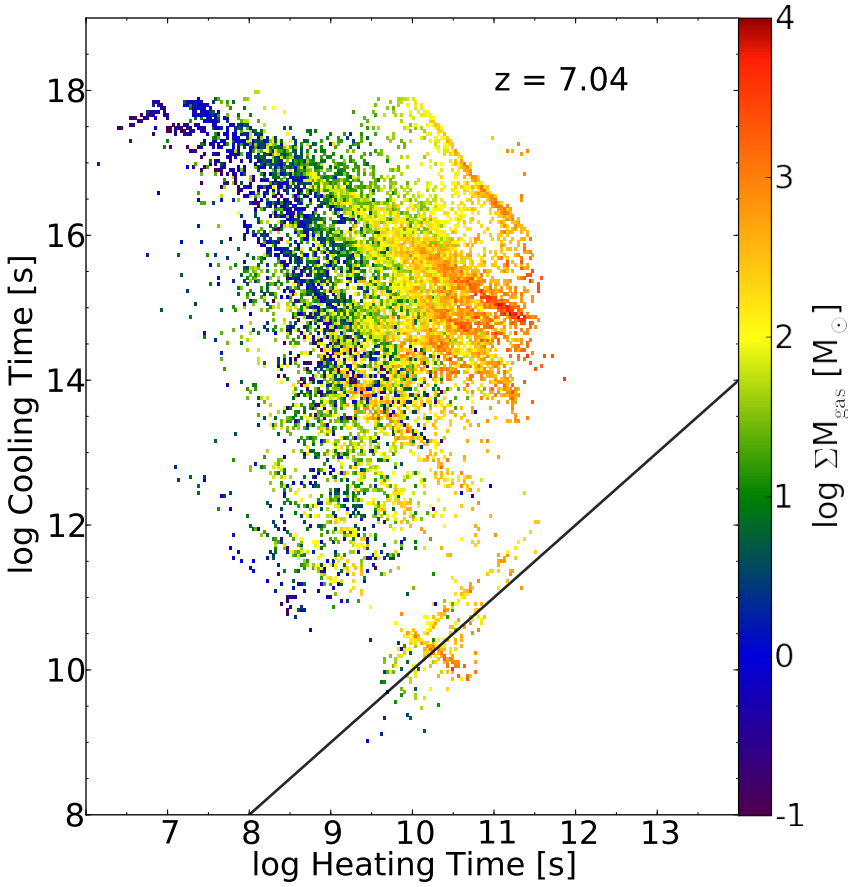

Figure 2.11 Cooling time versus estimated heating time at $z = 7.04$ for cells within r_{200} for the massive progenitor whose phase evolution is shown in Figure 2.5. The line where the cooling time equals the heating time is shown in black. The color of cells shows the cumulative sum of mass within the corresponding cooling time-heating time bin.

times (more precisely in cells where the cooling time is shorter than the dynamical time). Star particles are more likely to heat this gas since young star particles do not wander too far from their formation sites.

We interpret this result to mean that some energy produced by our feedback model is cooled in an unrealistic fashion. The key issue is most likely the length of time over which supernova energy is injected into the ISM, i.e. the length of t_f. Our feedback algorithm was motivated by the requirements of simulating larger mass halos and was

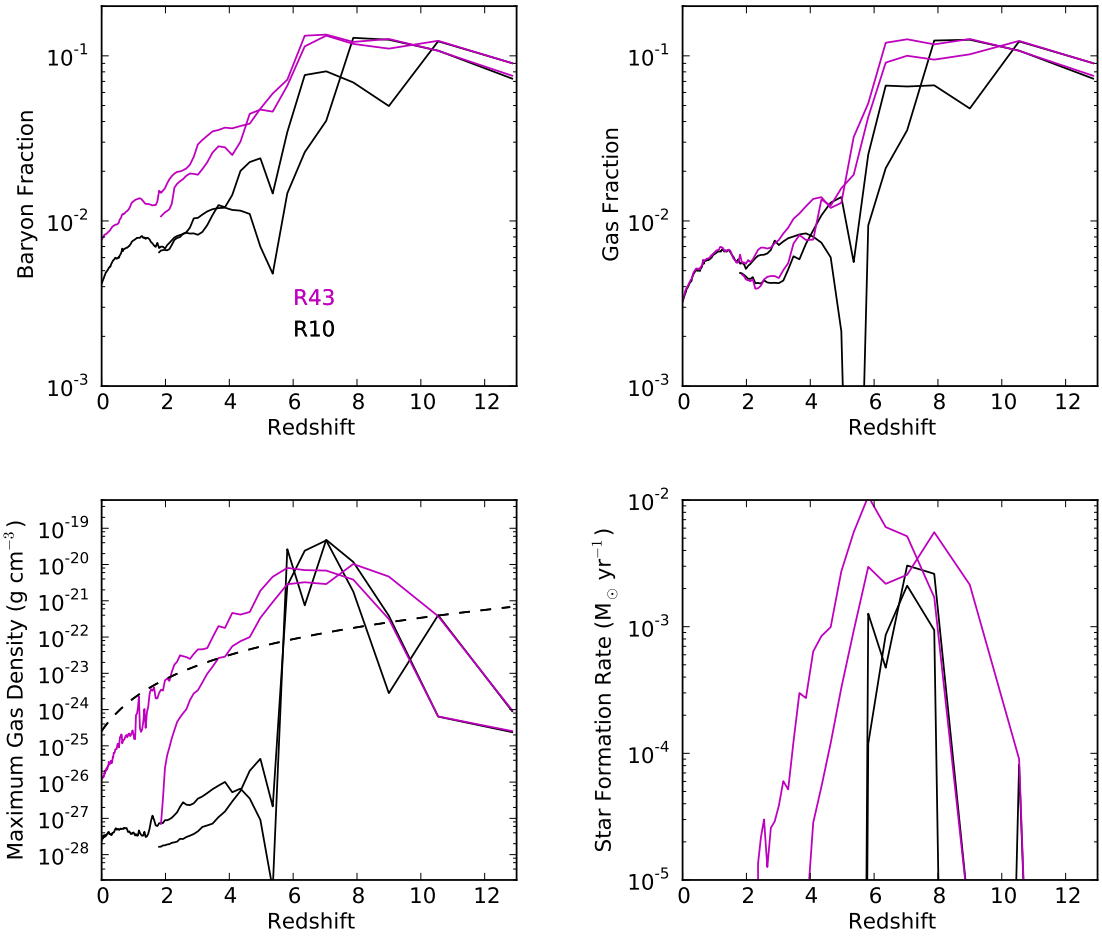

Figure 2.12 Evolution of properties for two massive progenitors in the canonical simulations R10 (black) and the lower minimum resolution simulation R43 (magenta). The properties depicted are the same as those shown in Figure 2.6.

designed to model the release of supernova energy from an entire stellar population that forms over an extended period of time (more than 10^7 years). A typical star particle in our simulations has a mass of 100 $M_\odot$, which is approaching the mass of an individual massive star. Extending the release of supernova energy over 10^7 years is therefore not suitable for this smaller mass star particle which is producing about one supernova's worth of energy. Reducing t_f or even eliminating it and instantaneously injecting energy into the cell would be more appropriate. Reducing t_f would result in a shorter $t_{\rm heat}$ (eq. 2.3), and so cooling would not be able to act before the injected feedback energy begins to operate. Similar models have been explored in high-resolution local simulations of the ISM (Joung & Mac Low 2006). We found, however, that even with our high spatial resolution, injecting a supernova's worth of energy into one resolution element instantaneously proved to be computationally challenging and we are working to develop an improved algorithm.

In our current model implementation, energy that is able to escape the central regions with shorter cooling times will not be quickly lost since gas everywhere outside the central region has comparatively long cooling times. Indeed in Figure 2.4 we do see evidence for supernova heated bubbles and metal pollution of the ISM and IGM. Previously in Section 2.2, we had concluded that reionization determines the overall gas fraction of halos and that dense gas is more directly affected by feedback. This interpretation still largely holds, however, the effect on dense gas may be more pronounced than what we have observed in our simulations. This would have the effect of enhancing the dominance of feedback over the UV background as the regulator of dense gas.

2.3.3 Resolution effects

To explore the impact of spatial resolution, we examine simulation R43, which is a run with the same dark matter particle resolution and physics as R10, but with four times coarser spatial resolution. R43 has a minimum cell length of 43 comoving parsecs. Figure 2.12 shows the evolution of relevant quantities for the two main star forming progenitors in R43 and Table 2.3 lists many of the final halo's properties. The gas fractions of halos in R43 evolve in a similar way to those in R10, with a large decline around $z = 6$. The declines in gas fraction prior to reionization, however, are almost nonexistent. These declines in R10 were due to supernova feedback and we see that coarser spatial resolution has decreased its effect.

The dense gas, which we found was more directly regulated by supernova feedback, also has very different behavior. The dense gas in the two main progenitors does not rise to quite as high a peak density, but is able to survive longer because of the diminished impact of supernovae in the low resolution run. Cells in R43 encompass 64 times the volume of cells in R10; therefore when a star particle injects energy into a cell in R43, the specific heating rate is approximately $1/64^{\text{th}}$ of what it is in R10. Dense gas is therefore able to survive longer. The maximum density cell within each halo peaks at a somewhat higher density in R10 because we are able to better resolve the collapse of cold clouds.

The star formation events in R43 are of longer duration due to the enhanced survivability of dense gas. Star formation continues in the main massive progenitor down to $z = 2$. This produces a final halo with a greater stellar mass (6.82×10^6 $M_\odot$). This is somewhat counter to the expectation that increased resolution will produce more star formation (since we resolve denser gas), however this result makes sense in light of the

Table 2.3 Summary of Final Halo Properties for Coarse Resolution Simulation R43.

	R43
$M_{tot}/M_\odot$	1.54×10^9
$M_*/M_\odot$	6.82×10^6
M_{gas}/M_{tot}	3.28×10^{-3}
r_{200} (kpc)	23.7
$r_{1/2}$ (pc)	326
$M_{1/2}/M_\odot$	1.56×10^7
$M_{300}/M_\odot$	1.42×10^7
$\sigma_{1/2}$ (km/s)	8.56
Log($\langle Z/Z_\odot \rangle$) (median)	-0.1
Log($\langle Z/Z_\odot \rangle$) (mean)	0.0
$\sigma_Z/Z_\odot$	0.83

Note: The quantities presented in each row are the same as in Table 2.2.

resolution-dependent effectiveness of our supernova feedback model.

Two other high-resolution, cosmological simulation studies track the evolution of similar mass halos to $z = 0$: Sawala et al. (2010) and Governato et al. (2012). Both studies use a SPH code, so it is not possible to directly compare our resolutions in a consistent way. However, both simulations are closer in spatial resolution to our simulation R43; Sawala et al. (2010) fix their softening length in such a way that their resolution is typically less than 100 pc and Governato et al. (2012) have a softening length of 64 pc for their highest resolution run. In simulations of somewhat more massive halos (10^{10} $M_\odot$), Governato et al. (2010) found that increasing resolution was key in reducing the central angular momentum of galactic disks that form in their halos and attribute this difference to better resolving spatially separated clouds in their higher resolution simulations, which enhanced the effect of supernova feedback as a regulator of star formation. They also found convergence in behavior between their medium resolution simulation (with a force resolution of 116 pc) and their high resolution simulation (with a force resolution of 86 pc), in contrast to the behavior of our simulations R10 and R43. Therefore, while it appears that resolution in

key in simulating star formation and supernova feedback in galaxy simulations, the exact mechanisms at play and the scales on which behavior converge are dependent on the physical prescriptions and hydrodynamical methods used.

Simulations R10 and R43 do not converge on a star-formation history or baryon fraction for our final halo, however we argue that many of the conclusions we have drawn from our higher resolution simulations hold. Clearly, reionization and feedback operate in the same way in both simulations, where the overall gas fraction is regulated by reionization and the dense gas evolution is regulated by supernova feedback. We do see an increasing effect of supernova feedback on the gas fraction with increasing resolution, so it is possible that increasing the resolution even more will have an even greater effect. The effect of reionization, however, is unchanged and still quite dominant. We may not have converged on a final stellar mass for this halo. We therefore conclude that our measures of the final stellar mass are likely to be an upper limit.

2.3.4 Metal ejection

We find that the main mechanism for gas ejection from these low mass halos is photo-evaporative winds due to reionization. It remains unclear, however, if this is also the mechanism for metal ejection. We see evidence for metal rich supernova heated winds in Figure 2.4, but it also appears from Figure 2.3 that the metallicity of dark halos increases after reionization.

We can answer this question by comparing simulations with and without supernova feedback and reionization: R10, one of our canonical runs that contains our complete physical model; R10-noFB-LimCool, which has no thermal supernova feedback; and R10-

noUV, which has no UV background. Figures 2.6 and 2.8 show that these three simulations have produced varying amounts of star particles over somewhat different star formation histories, but we can nevertheless draw robust conclusions.

Figure 2.13 shows projections of gas metallicity of a large volume that encompasses the dwarf group at $z = 3.3$, which eventually forms the final dwarf halo. It clearly shows that in simulations with thermal supernova feedback, metals are ejected to much greater distances and more completely fill the volume. The simulation without thermal feedback, R10-noFB-LimCool, has significantly less IGM metal pollution. This is despite the fact that the total gas fractions of halos in R10-noFB-LimCool are quite similar to those seen in R10 (Fig. 2.8). The gas fractions of halos in R10-noUV are quite elevated at this redshift as compared to halos in R10 (Fig. 2.6). Despite this, the extent of metal pollution is relatively similar between the two runs with supernova feedback. Therefore, we conclude that supernova feedback is the primary mechanism for metal ejection in our model.

Increased enrichment of dark halos after reionization as shown in Figure 2.3 is likely quite complicated and due to a combination of effects. Since supernova feedback is the mechanism for metal ejection from luminous halos in our model, the enrichment of dark halos depends on the proximity of dark halos to luminous halos and the speeds of supernova enriched winds (e.g. Cen & Bryan 2001). However, the increased degree of enrichment occurs after the cessation of photoevaporative winds due to reionization. The large drop in gas fraction seen in Figure 2.2 indicates the effect of these photoevaporative winds on halo gas. This decline happens in both R10 and R10-earlyUV just before the increase in metallicity of dark halos. It is likely more difficult for supernova driven winds to penetrate halos undergoing strong photoevaporative winds. This issue may be an

interesting topic for future study.

As we have discussed, stellar populations of dSph galaxies are extremely metal poor and this does not appear to be simply due to their low star formation rates. Kirby et al. (2011b) have demonstrated that dSphs in the Milky Way eject almost all of their metals. Dwarf spheroidals are also observed to be quite gas poor (Mateo 1998). As we have discussed, environment most likely plays a key role in the gas content of Milky Way dwarfs. However, our simulations at least demonstrate that the main mechanism for gas expulsion need not be the same as for metal ejection. This picture is consistent with the simulations of Mac Low & Ferrara (1999) and Fragile et al. (2003), who found, using high-resolution, idealized models of dwarf galaxies, that metals were more easily ejected from galaxies than gas.

The discrepancy in metallicity between our simulated stellar populations and observed systems described in section 4.1.2 indicates that star-forming gas in our model is too metal rich. This over-enrichment of star-forming gas may be due to insufficient ejection of metals by our supernova feedback model, despite the apparent large scale enrichment of the IGM on the scale of tens of kpc seen in Figures 2.4 and 2.6. We therefore cannot confidently make predictions for the density of metals in the IGM produced by dwarfs. It is certainly possible that feedback mechanisms other than supernovae may play an important role in ejecting metals, such as ionization from young stars. What our models do show, however, is that in systems where the gas fraction is determined by the cosmic UV background, an extra ingredient that preferentially affects metal rich gas is needed to eject metals.

If supernova feedback is primarily responsible for the stellar metallicity of dSphs, then

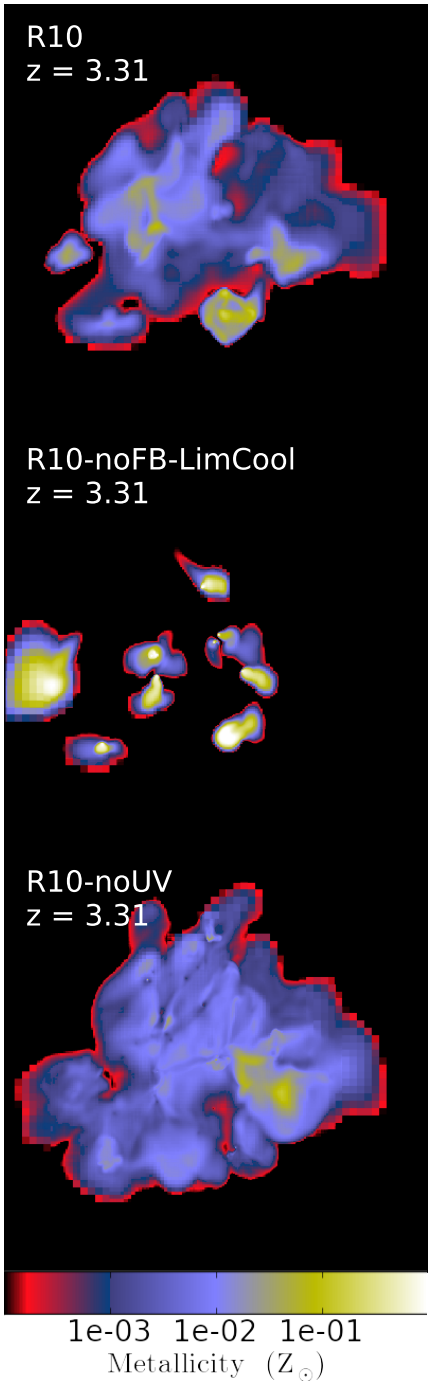

Figure 2.13 Gas density weighted projections of gas metallicity at redshift 3.31 for R10, R10-noFB and R10-noUV. All panels show projections of 150 kpc cubic volumes that encompass all the progenitor halos at this redshift.

these systems are an excellent test to judge the efficacy of feedback models, given the clear constraints of observations. Several simulated models produce low metallicities for Milky Way dSph analogues using a variety of approaches, such as idealized, non-cosmological models (e.g. Revaz & Jablonka 2012); cosmological models focusing on high redshift evolution (Ricotti & Gnedin 2005; Tassis et al. 2012; Wise et al. 2012a); coarsely resolved cosmological models of satellite systems of Milky Way type spiral galaxies (Okamoto et al. 2010; Sawala et al. 2012); and highly resolved cosmological zoom-in simulations like our own (Sawala et al. 2010). Most of these studies rely on feedback schemes that compensate for resolutions too low to capture the Sedov phase of supernovae, with the exception of Wise et al. (2012a), who have very high resolutions (1 comoving pc) in their high redshift study and find that momentum from feedback, in the form of radiation pressure, is necessary to produce low metallicities. The model most comparable to our own, which is run down to $z = 0$, is that of Sawala et al. (2010), who in high resolution simulations (< 100 pc) of isolated halos similar in mass to our own, were able to produce halos that lie on the observed luminosity-metallicity relation. It is unclear, however, how natural this result is given that the fraction of metals injected into the hot (or cold) phase can be calibrated in their subgrid model. In addition, we note that metal mixing remains a serious uncertainty in SPH (Booth et al. 2012). Simulations of larger cosmological volumes that contain larger halos have also found that feedback is important in explaining the evolution of galaxy metallicity and enrichment of the IGM over cosmic time (Finlator & Davé 2008).

2.3.5 Dark matter properties

Dark matter halos in cosmological N-body simulations follow a predictable density profile with a steeply-sloped cusp at the centre (Navarro et al. 1997, 2010). Several previous studies have found that baryon physics, particularly supernova feedback, can weaken the central dark matter cusp (e.g. Navarro et al. 1996; Gnedin & Zhao 2002; Governato et al. 2012). Several mechanisms for this transformation have been proposed, such as the response of dark matter to the sudden removal of gas from halo centres (e.g. Navarro et al. 1996; Gnedin & Zhao 2002), and the direct transfer of energy from repeated energetic gas outflows to dark matter particles (Pontzen & Governato 2012; Governato et al. 2012).

Measuring the actual dark matter density profiles of galaxies is, of course, quite challenging, but one way is to use the resolved stellar populations in dwarf spheroidal galaxies. To date, studies comparing the dynamics of dSphs to cosmological N-body simulations have been inconclusive (Boylan-Kolchin et al. 2012; Strigari et al. 2010; Vera-Ciro et al. 2013). Density profiles with shallow or steep central slopes have been found to fit the observational data equally well (Walker et al. 2009b).

Figure 2.14 compares the dark matter density profiles for the final halo in R10 and R10-DM, a dark matter only simulation run with the same initial conditions. We see that the dark matter density profile is almost the same between R10 and R10-DM; the halo in R10 is slightly less dense in the inner regions relative to R10-DM, indicative of a mild heating effect. We therefore conclude that the impact of baryon physics on the dark matter density was negligible for our halo. Although not shown in Figure 2.14, both profiles are well fit by a NFW profile. The stellar density profile does not follow a NFW profile. It appears to have a central slope similar to a NFW profile but falls off more quickly beyond

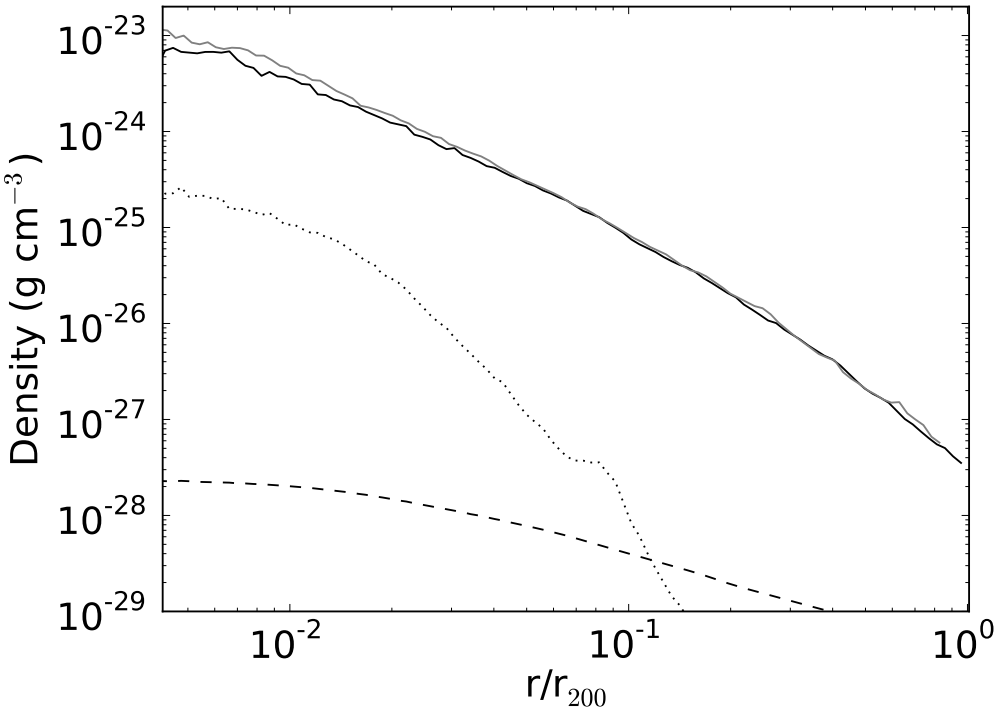

Figure 2.14 Dark matter density profile (solid black line), stellar mass density profile (dotted line) and gas density profile (dashed line) for the final halo at $z = 0$ in R10. The dark matter density profile for the final halo in R10-DM is shown in grey.

300 pc. Visual inspection of the final stellar density map shown in the bottom right panel of Figure 2.4 also shows that clumpiness and tidal features from late mergers remain, which produces a bump in the stellar density profile.

The one other high-resolution study to examine the density profile of dark matter halos at this halo mass scale with baryon physics is Governato et al. (2012), though using a different hydrodynamical method and stellar feedback model. They find flattened central density profiles for halos with virial masses above 10^{10} $M_{\odot}$. For halos below this threshold, they find halos down to our halo mass of 10^{9} $M_{\odot}$ have density profiles consistent with NFW profiles, similar to our results. Haloes in their models do not appear to have consistently

flattened central density profiles until the stellar mass rises above 5×10^6 $M_\odot$.

As we have discussed, our supernova driven outflows may not be sufficiently energetic (as evidenced by the metallicity distribution). It is possible that this failure results in the central density of our halo remaining cuspy, however it is also possible that the low star formation rates of our halo are just insufficient to produce enough energy to have a significant impact on the density profile of our simulated halo.

2.3.6 Neglected physics

In this section, we briefly discuss physical effects that we do not include in our model. We do not have an implementation of local UV heating from young stars, either ionizing or dissociating, in our model. This effect may have an impact on dense gas as young stars will be located within close proximity. Gnedin (2010) found that local UV heating sources dominated over the cosmic UV background for both ionizing and Lyman-Werner radiation in halos with masses between 10^{10} and 10^{12} $M_\odot$ at a redshift of three. We are probing halos at much lower masses with much lower star formation rates, but it may be that UV heating from young stars can suppress star formation or make supernova feedback more effective by preheating gas.

We do not include any effects of dust in our model. The formation of H_2 on the surface of dust grains is important in gas with metallicities above approximately 10^{-3} $Z_\odot$ (Glover 2003). The main effect of H_2 in our models is as a coolant in very metal poor gas. Since the amount of dust in gas with metallicities below 10^{-3} $Z_\odot$ is too small to be important in H_2 production, the lack of dust does not significantly affect cooling and therefore star formation in our models. It does mean that our models do not accurately follow the

molecular gas fraction of halos, which may be an interesting topic of future study.

We do not model early metal-free star formation as a distinct mode of star formation. Wise et al. (2012b) presented high-resolution simulations of low mass halos at high redshift that include the transition between Population III and Population II star formation. They found that a single Population III supernova can enrich the ISM of a halo to the level where metal line cooling dominates over molecular H_2 cooling.

We model supernovae as producing exclusively thermal energy. Supernovae also produce substantial amounts of radiation, which can not only heat the gas, but can also exert radiation pressure. The computational cost necessary to do radiative transfer in cosmological calculations is currently too expensive to follow the evolution of halos down to $z = 0$, however several groups have explored its effect at high redshift (e.g. Wise et al. 2012a). There are also other effects such as magnetic fields and cosmic rays which we neglect and may potentially be important in galaxies of this size (Wadepuhl & Springel 2011).

Chapter 3

Supernova Feedback Modeling

As we have seen in the previous chapter, supernova feedback can play an important role in truncating star formation in photoevaporated, low-mass halos. More crucially, supernova feedback appears to be the dominant mechanism for metal ejection from these halos. This mechanism has also been seen in idealized simulations of outflows from dwarfs (Mac Low & Ferrara 1999; Fragile et al. 2003) and has been conjectured from empirical analysis of Milky Way dSphs (Kirby et al. 2011b).

The supernova feedback technique employed in the galaxy simulations described in Chapter 2 is an intentionally simple model that injects purely thermal energy into a single simulation cell over an extended period of time, roughly equal to a few factors of the gas dynamical time in the star particle's birth cell. This method (adapted from Cen & Ostriker (1992)) was developed for use in coarser resolution studies of more massive galaxies and has been extensively used for this purpose (e.g. Hummels & Bryan 2012). We have found, however, that in our high resolution simulations utilizing this model supernovae were unable to remove metals effectively enough from star forming gas, resulting in a highly

enriched final stellar population.

A number of studies at high redshift or in idealized settings have explored more complex methods of modeling feedback that include a wider array of stellar feedback sources such as effects from stellar winds and ionizing radiation (Agertz et al. 2013; Hopkins et al. 2011; Wise et al. 2012a). A hallmark of many of these treatments is the inclusion of momentum from various feedback sources; and indeed, Wise et al. (2012a) found that radiation pressure was key in ejecting metals from the ISM of high redshift dwarf galaxies.

In this chapter, we will further explore the single cell thermal feedback model employed in Chapter 2. From this discussion, we will propose a new, alternative method of supernova feedback, the defining characteristic of which is the inclusion of kinetic energy injection on short timescales. We will then carefully explore this model with a set of idealized test simulations demonstrating the effect of a single feedback event on a homogeneous medium. These test simulations will cover a wide range of resolutions and physical conditions in order to provide insight into this model's inclusion in galaxy simulations.

3.1 Single cell thermal feedback model

The details of the single cell thermal feedback model used in Chapter 2 rest on several assumptions about the stellar population represented by a star particle and how feedback energy from this stellar population couples to the ISM at coarse spatial resolutions. At the spatial and star particle resolutions employed in the simulations presented in Chapter 2,

some of these assumptions no longer hold.

The first assumption to consider is the assumption that on scales equivalent to the size of a typical cell that all supernova energy is thermalized. On these scales ($\sim$ 11 comoving pc), analytic theory and high resolution simulations of supernova ejecta predict that a significant fraction of energy (Chevalier 1974, e.g. $\sim$ 20-30%) remains in kinetic form. During the energy conserving Sedov phase (Sedov 1959; Taylor 1950), when the supernova remnant expansion is driven by the high internal pressure of shocked gas, the fraction of kinetic energy in the shocked material is approximately 30% (Chevalier 1974). The kinetic fraction begins to decline once the remnant enters the 'snow-plow' phase when radiative cooling dissipates enough energy such that the expansion of the remnant is no longer driven by high internal pressure, but rather is carried along by the self-momentum of the dense, thin shell of swept-up ISM at the shock front. By making some simple assumptions about the cooling curve, the shock radius at which this transition occurs is approximately 24 pc for a supernova energy of 10^{51}ergs and a ISM density of 1 cm^{-3}; it occurs at approximately 3.4 pc in ISM with a density of 100 cm^{-3} (Draine 2011). At redshifts greater that 3.5 when star formation occurs in our galaxy models from Chapter 2, our simulations resolve this radius typically by a few cells. The assumption that all the supernova energy has been thermalized on scales much smaller than the cell width likely no longer holds.

The second assumption to consider is the mass of the stellar population and the timescale over which it will produce supernova energy. The typical mass of star particles in one of our galaxy simulations is 100 $M_\odot$, approaching the mass of a massive star. The stellar population represented by a star particle of this mass should be approximately

coeval and the number of supernova events it produces should be of order of one to a few events. The original reason for the extended release of supernova energy in this model was the assumption that the stellar population represented by the star particle was large and produced many Type II supernovae over an extended time period since the population would likely take several gas dynamical times to form from its natal molecular cloud. Gradually releasing supernova energy over an extended period as we have done may result in some overcooling as we have discussed in Section 2.3.2, however the initial small release of energy may make the energy released later by the star particle more effective, by reducing the density of the surrounding medium.

The results of this model on the metal enrichment of gas and stars can be further seen in Figure 3.1. Here we see that over 52% of the metals produced by stars in simulation R10 from Chapter 2 end up in stars; for R10-earlyUV the amount is 8.5%. In R10 the fraction of metals retained in stars increases as the star formation rate peaks; the amount of metals locked up in stars after redshift 7.5 nearly equals the amount of metals produced. The estimated fraction of metal retention of stars in Milky Way dSphs is below 4% (Kirby et al. 2011a), less than the retention fraction found in R10-earlyUV and much less than the retention fraction found in R10.

Studying this model in an idealized setting reveals how this type of numerical supernova feedback impacts the energetics and momentum of surrounding gas at high resolution. Figures 3.2 and 3.3 show the evolution of energy within a box of gas that is heated by a single star particle undergoing feedback according to this model. We have conducted these models with both the ZEUS hydrodynamical solver used in Chapter 2 and the PPM hydrodynamical solver, a piecewise-parabolic method for solving Eu-

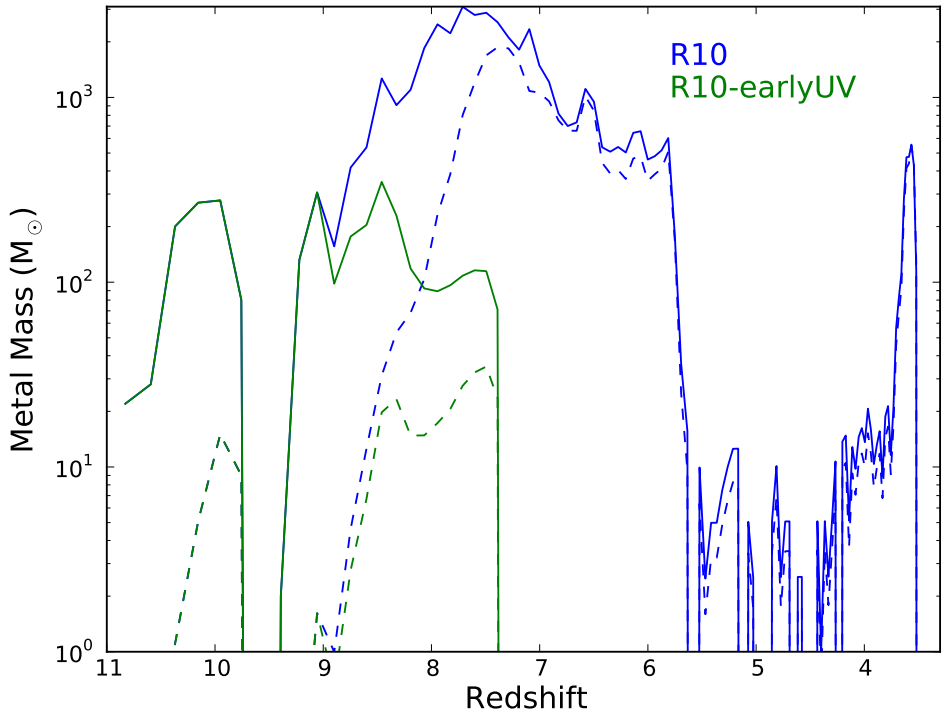

Figure 3.1 An illustration of the production and retention of metals by star particles found in the final target halo in simulations R10 (blue) and R10-earlyUV (green) described in Chapter 2. Solid lines give the mass of metals injected into the ISM by each stellar population versus redshift. Dashed lines give the mass of metals added to newly formed star particles, and therefore removed from the ISM, versus redshift.

ler's equations (Colella & Woodward 1984). The gas within the simulation volume has an initially uniform density and uniform temperature of 100 K, where $\gamma = 5/3$. These simulations include temperature dependent cooling from atomic hydrogen and electron scattering as well as metal line cooling assuming a gas metallicity of 0.1 $Z_\odot$with a cooling floor at $log(T/\mathrm{K}) = 4.2$ adapted from the SPEX package (Schure et al. 2009) as done by Li & Bryan (2012). These models do not include many effects that are important in modeling the ISM (e.g. non-equilibrium cooling, radiation pressure, conduction, magnetic fields etc.) as these simple models are not intended to be detailed models of the ISM. Rather,

these idealized simulations are intended to show the behavior of this feedback method under controlled conditions similar to what is found in a large scale galaxy simulation and provide a bridge to understanding a new supernova feedback method which we will describe in subsequent sections.

Cooling has an immediate impact on the heated gas. In both high and low density media, the amount of energy radiated away begins to become a significant fraction of the energy deposited before even 1% of the total energy has been released. At the end of the energy deposition, which we have fixed to be 100 Myr, approximately only 10% of the deposited energy remains in the ISM. The form this energy takes does differ between high and low density media. In the low density medium tested, about 40% of the thermal energy deposited is rapidly converted to kinetic energy. As thermal energy continues to be injected into the ISM, this fraction of kinetic energy drops to approximately 30%, but as more and more thermal energy is injected thermal energy continues to be converted to kinetic energy, maintaing a kinetic energy fraction of $\sim$ 30%. It is interesting to note this is the fraction of kinetic energy found in adiabatic calculations of the Sedov phase of supernova explosions. In the denser background medium tested, there is a slower rise in the kinetic energy fraction and as thermal energy is continuously injected into the ISM it is not efficiently converted to kinetic energy. The kinetic energy fraction continues to fall, dropping below 20% by 100 Myr.

We have also tested the effect of particle motion. In 100 Myr at 5 km s^{-1} a star particle can move more than 500 pc, a significant fraction of r_{200} for a high redshift progenitor halo. One might expect cooling to be more effective when the particle enters material unaffected by its previous energy release, but that does not appear to be the case in our test models.

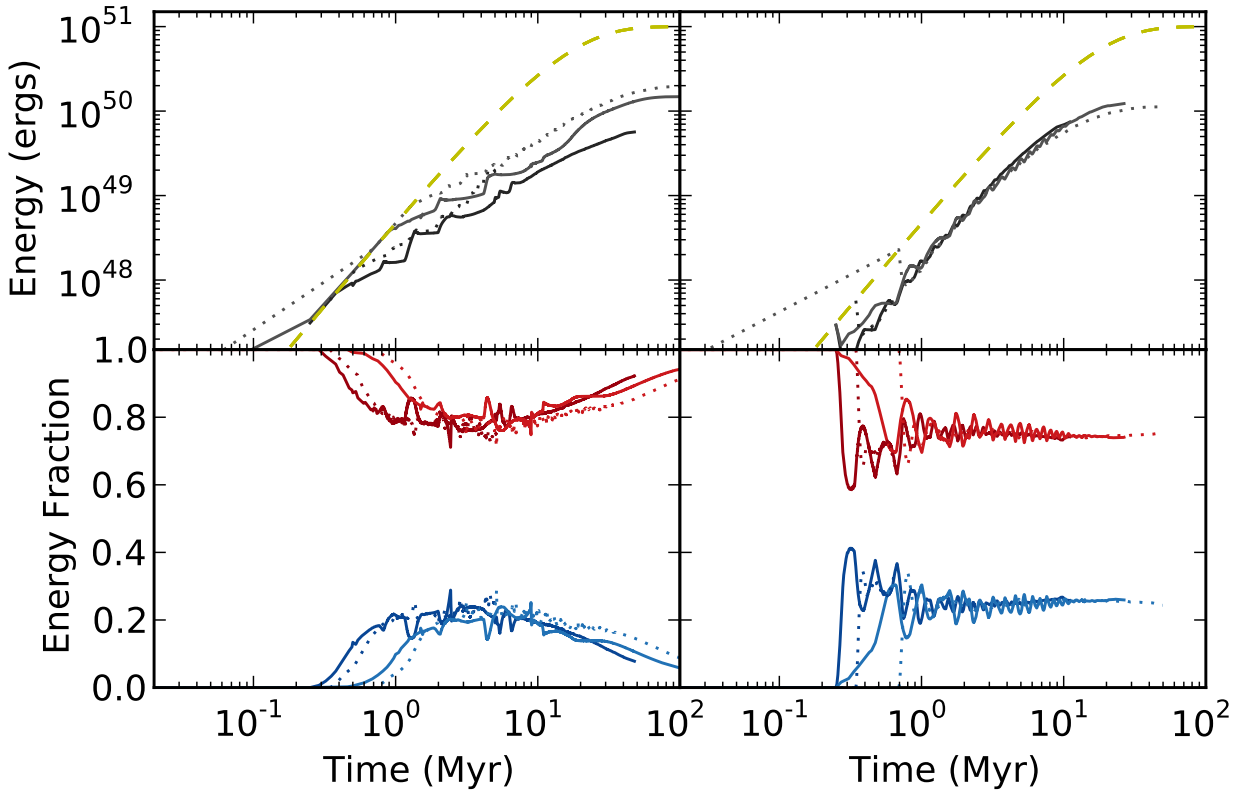

Figure 3.2 Energy evolution of test simulations of the single cell thermal feedback model used in Chapter 2. These simulations were conducted with the PPM hydrodynamic solver. The left column shows the evolution of simulations conducted in a uniform gas density of 100 cm^{-3} and the right column shows identical simulations done in gas with a density of 1 cm^{-3}. We assume the mean molecular weight of the gas is 0.6. The top row shows the total energy excess of the simulation volume, which is the total energy of the volume less the total initial thermal energy. The yellow dashed line shows the energy injected by the star particle versus time. The bottom row shows the fraction of this energy excess in thermal form (red lines) and kinetic form (blue lines). The darker lines of each color in each panel correspond to simulations conducted with a cell resolution of 4 pc. The lighter lines correspond to simulations conducted with a resolution of 8 pc. The dotted lines correspond to simulations where the star particle has a constant velocity of 5 km/s throughout the simulation. Not all of these simulations have been run for the full 100 Myr.

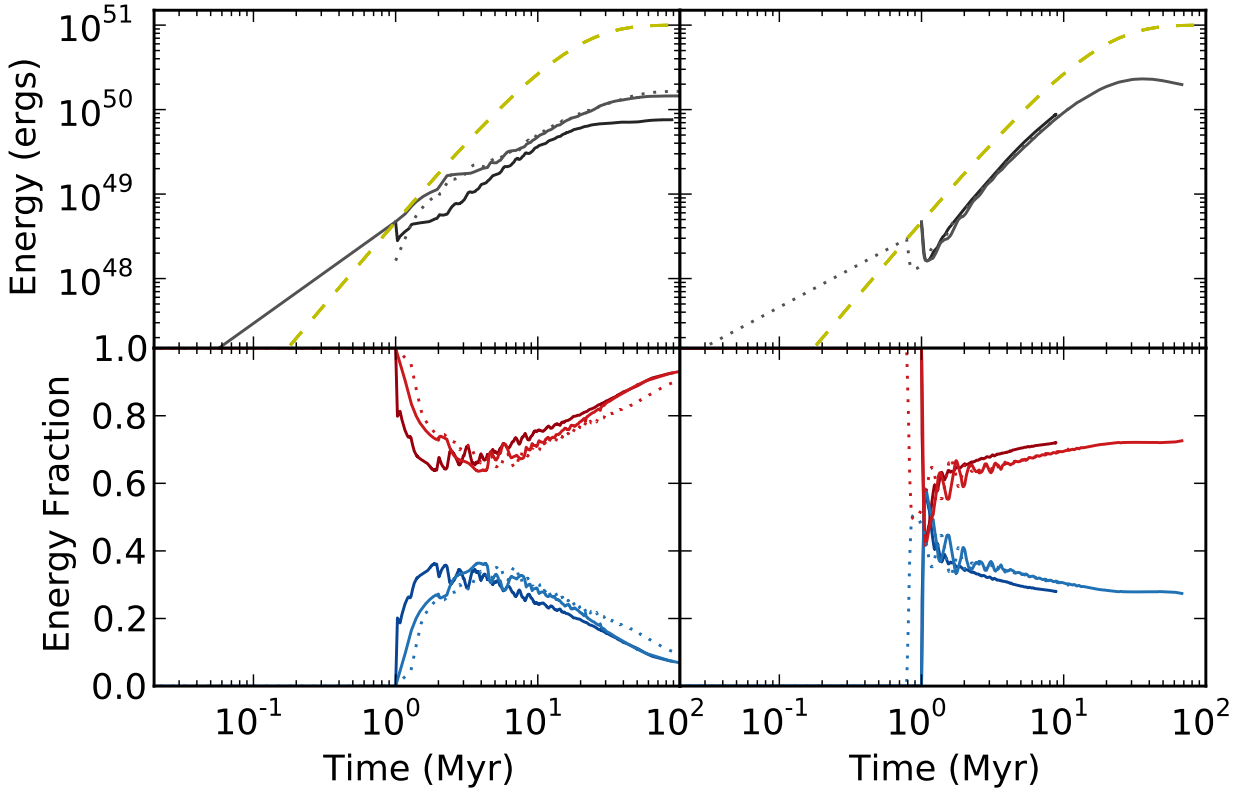

Figure 3.3 The same quantities are presented here as in Figure 3.2, but these simulations were conducted with the ZEUS hydrodynamic solver. Not all of these simulations have been run for the full 100 Myr.

We have also tested the effect of different hydrodynamical solvers. In the simulations presented in Chapter 2 we used the finite-difference method ZEUS, shown in Figure 3.3. ZEUS is not an energy conserving method, however when compared to the evolution of the same simulations done with the PPM method, which is energy conserving, the differences in total energy dissipation are slight. The most noticeable difference is seen in the conversion of thermal energy to kinetic energy, as the simulations done with ZEUS appear to convert small amounts of thermal energy to kinetic energy more readily at the beginning of the simulation.

From these simple simulations, it becomes apparent that the density of the medium

surrounding the star particle is extremely important in determining the subsequent evolution of the supernova heated gas. Of all the effects probed by these test simulations, the density of the background medium has the greatest effect. The density of gas affected by feedback in the galaxy simulations in Chapter 2 is certainly not uniform as in these cases, however, we would expect the density of gas affected to be more like the 100 cm^{-3} case tested, rather than the 1 cm^{-3} case. We can see that while the amount of energy lost is not too dissimilar between the different density cases, the amount of kinetic energy is. The effective conversion of thermal to kinetic energy diminishes over time in the dense medium case.

For this reason and the physical arguments described in the beginning of the section, we have developed and will test a new feedback algorithm that includes the quick injection of kinetic energy.

3.2 Method for Kinetic Feedback

In this section, we describe a method for including both kinetic and thermal feedback from supernovae for use in grid based hydrodynamic codes such as Enzo. Rather than injecting thermal energy into a single cell containing a supernova-producing star particle, this method injects both thermal and kinetic energy into a grid patch based on an algorithm related to the cloud-in-cell (CIC) algorithm (Hockney & Eastwood 1988).

The total supernova energy is defined to be a fraction (ϵ_{SN}) of the rest mass energy of the star particle producing the feedback ($E_{SN} = \epsilon_{SN} m_* c^2$). In this model, the fraction of the supernova energy that is initially injected as kinetic energy is a free parameter, f_{kin},

between zero and one. The kinetic and thermal energies after the supernovae are therefore

$$E^a_{kin} = E^b_{kin} + f_{kin} E_{SN} \tag{3.1}$$

$$E^a_{therm} = E^b_{therm} + (1 - f_{kin}) E_{SN}, \tag{3.2}$$

where E^b_{therm} and E^b_{kin} are the total thermal and kinetic energies of the feedback injection zone before the energy deposition.

Kinetic energy is added to cells by directly altering the cells' momenta. An algorithm is needed that both adds the correct amount of kinetic energy and yet also adds zero net (vector) momentum to the feedback zone (in a frame comoving with the particle). We do this by adapting the well-known CIC method. To remind readers, the CIC method is a way of smoothly adding particle mass to a grid. Conceptually, this is done by virtually converting the particle into a uniform 'cloud' with a size equal to one cell width. Since the particle position is generally not coincident with a cell center, this region will overlap 8 cells on the grid. The amount of mass added to each cell is proportional to the volume overlap of the virtual cloud with that cell.

We adopt this same idea, but instead of using a region of size 1×1×1 cell widths, we use a 3×3×3 cell cloud centered on the star particle's position. The reason for this larger cloud is that the momentum is a vector quantity and therefore momenta with opposite signs should not contribute to the same cell. The direction of the momentum vector of each virtual single cell is found by taking the vector from the center of the region to the center of that virtual cell. The magnitude of each cell's momentum vector is found by enforcing the requirement that the total amount of kinetic energy added to the grid follows

equation 3.1. Since this depends on the amount of momentum pre-existing on the grid, this step is non-trivial and we describe it in detail below. We note that the central cell contributes no momentum.

The contribution of mass, thermal energy and metals is assumed to be uniformly distributed throughout the 3^3 cloud, and the addition of these components is very similar to an expanded CIC method. Since the virtual cloud is of size 3^3, it will, in general, overlap 4^3 cells in the underlying grid (just as for the original CIC method, as clouds of size 1^3 overlap a region of size 2^3 cells).

We now describe how to determine the magnitude of the momentum vectors for each of the $3^3 - 1$ virtual cells (the central cell has zero momentum). The magnitude of each of the vectors must be the same to keep the total net momentum zero. We begin by converting the grid velocities into momentum and translating into a frame comoving with the particle. From the total amount of kinetic energy and mass injected into the gas, we can determine the amount of momentum deposited in each cell, Δp as follows. The total kinetic energy of the gas surrounding the star particle is a sum over all the affected cells (cells in the grid are denoted with a subscript i):

$$E^a_{kin} = \sum_i \frac{1}{2} \frac{(\mathbf{p}^b_i + \sum_j \Delta p f_{i,j} \mathbf{x_j})^2}{m^b_i + \sum_j \Delta m f_{i,j}}, \tag{3.3}$$

The sum within each term is over all of the virtual 'cloud' cells (denoted with a subscript j) that overlap with the grid cell i and $f_{i,j}$ is the fractional volume of that overlap (normalized such that $\sum_i f_{i,j} = 1$). We denote $\mathbf{p^b_i}$ as the momentum before the supernova event in cell i; m^b_i is the mass before in cell i; and $\Delta m = m_{\rm inj}/3^3$ is the mass of each cloud cell ($m_{\rm inj}$ is the

total mass to be injected). Finally, the unit directional momentum vector of each cloud cell is given by $\mathbf{x_j}$. Since star particles will virtually never be perfectly centered within a grid cell, a total of 63 cells will typically receive some momentum contribution.

Because Δp is a constant and can be pulled out of the above sum, equation 3.3 is a quadratic equation of the quantity Δp; we can therefore solve for Δp:

$$\Delta p = \frac{-b + \sqrt{b^2 - 4ac}}{2c}, \tag{3.4}$$

where

$$a = \sum_i \frac{1}{2} \frac{(\mathbf{p}_i^b)^2}{m_i^b + \sum_j \Delta m f_{i,j}} - E_{kin}^a = \sum_i \frac{1}{2} \frac{(\mathbf{p}_i^b)^2}{m_i^b + \sum_j \Delta m f_{i,j}} - E_{kin}^b - f_{kin} E_{SN} \tag{3.5}$$

$$b = \sum_i \frac{\mathbf{p}_i^b \cdot \sum_j \mathbf{x}_j f_{i,j}}{m_i^b + \sum_j \Delta m f_{i,j}} \tag{3.6}$$

$$c = \sum_i \frac{1}{2} \frac{(\sum_j \mathbf{x}_j f_{i,j})^2}{m_i^b + \sum_j \Delta m f_{i,j}}, \tag{3.7}$$

and the total kinetic energy of the gas in the supernova affected region before the blast is given by:

$$E_{kin}^b = \sum_i \frac{1}{2} \frac{(\mathbf{p}_i^b)^2}{m_i^b}. \tag{3.8}$$

This algorithm has been implemented as described into Enzo.

3.3 Kinetic Feedback Model Tests

To better understand the effect of the kinetic feedback model in galaxy simulations such as the ones that will be discussed in Chapter 4, we have conducted a set of idealized test simulations of this method similar to the simulations discussed in Section 3.1. This method introduces a new, tunable parameter f_{kin}, the fraction of injected kinetic energy. Our goal is to understand the effect of f_{kin} over a wide range of parameter space including the conditions found in the galaxy simulations discussed in Chapter 2.

3.3.1 Testing Setup

We have explored the impact of our supernova feedback model by testing its effect on gas at resolutions appropriate for use in large scale cosmological and isolated galaxy simulations. These tests are done by placing a single star particle, which is the source of supernova energy, within a box of uniform density gas and uniform thermal energy with no initial bulk motions. The initial gas temperature is set to 100 K, where $\gamma = 5/3$. The mean molecular weight of the gas is assumed to be 0.6. The particle is placed offset from the box center by half a cell width. The star particle injects thermal energy, kinetic energy and mass within a single time step into a volume equivalent in size to 27 cell cloud centered around the star particle as described in Section 3.2.

Each simulation is conducted in a homogeneous medium with a density between 1 and 1000 cm^{-3}. These test simulations were run with a variety of cell resolutions ranging from 0.5 pc to 8 pc and done without adaptive refinement.

In simulations that include cooling, we use the same temperature dependent cooling

curve as used in Section 3.1, which assumes a gas metallicity of 0.1 $Z_{\odot}$and a cooling floor at $log(T/\mathrm{K}) = 4.2$. As in Section 3.1, we conduct simulations with both the PPM and ZEUS hydrodynamical solvers. In the simulations conducted with PPM we employ the dual energy formalism to maintain consistency between kinetic energy advected by the energy conservation equation and the momentum conservation equation (Bryan et al. 1995).

The width of the simulation box is fixed to be three times the analytic Sedov blast radius, R_{sedov}, at the final time of the simulation (typically 1 Myr) with a minimum box width of 50 cells. The analytic Sedov blast radius depends on the choice of total supernova energy, e_{SN}, and the density of the background medium, ρ_o (Draine 2011):

$$R_{sedov} \propto (\frac{e_{SN}}{\rho_o})^{0.2} t^{0.4}. \tag{3.9}$$

For a background density of 1 cm^{-3}, a supernova energy of 10^{51} ergs and final time of 1 Myr, this gives a box size of 237 pc.

The initial timestep is fixed to be

$$dt_i = 0.1 * \frac{dx}{c_s + v_s}, \tag{3.10}$$

where c_s is the estimated sound speed of gas in the post feedback injection region and v_s is the estimated initial speed of the shock:

$$c_s = ((\gamma - 1)\gamma(1 - f_{kin})\frac{e_{SN}}{m_{cell}})^{1/2}, \tag{3.11}$$

$$v_s = (\frac{2 f_{kin} e_{SN}}{\rho dx^3})^{1/2}, \tag{3.12}$$

and

$$\rho = \rho_o + \frac{f_m M_*}{27 dx^3}. \tag{3.13}$$

Enzo computes an initial time step from the Courant condition based on the initial state of the gas. This estimation, however, would give a time step much too short to account for the large velocities that are induced in the first time step by the injection of energy. This estimate of a shorter time step is necessary to ensure that the bulk flow of gas across the grid in the first time step cannot cross more than one cell width.

3.3.2 High-resolution reference models

To understand how to use our model in a full galaxy simulation where star particles produce supernovae in gas of varying densities and resolutions, we first explore how our model behaves at high resolution. The highest resolution we test is $\Delta x = 0.5$ pc and this resolution is sufficient to resolve the free-expansion, Sedov and (in tests with cooling) the snow-plow phases of supernova remnant evolution. These models will provide context for understanding the more coarsely resolved test simulations.

Figures 3.4 and 3.5 show the behavior of a typical high-resolution test in the presence and absence of cooling. Without cooling, the behavior of our model scales dimensionlessly and models with different background densities produce the same behavior, scaled by the appropriate units. Our adiabatic model produces a well behaved and regular shock that

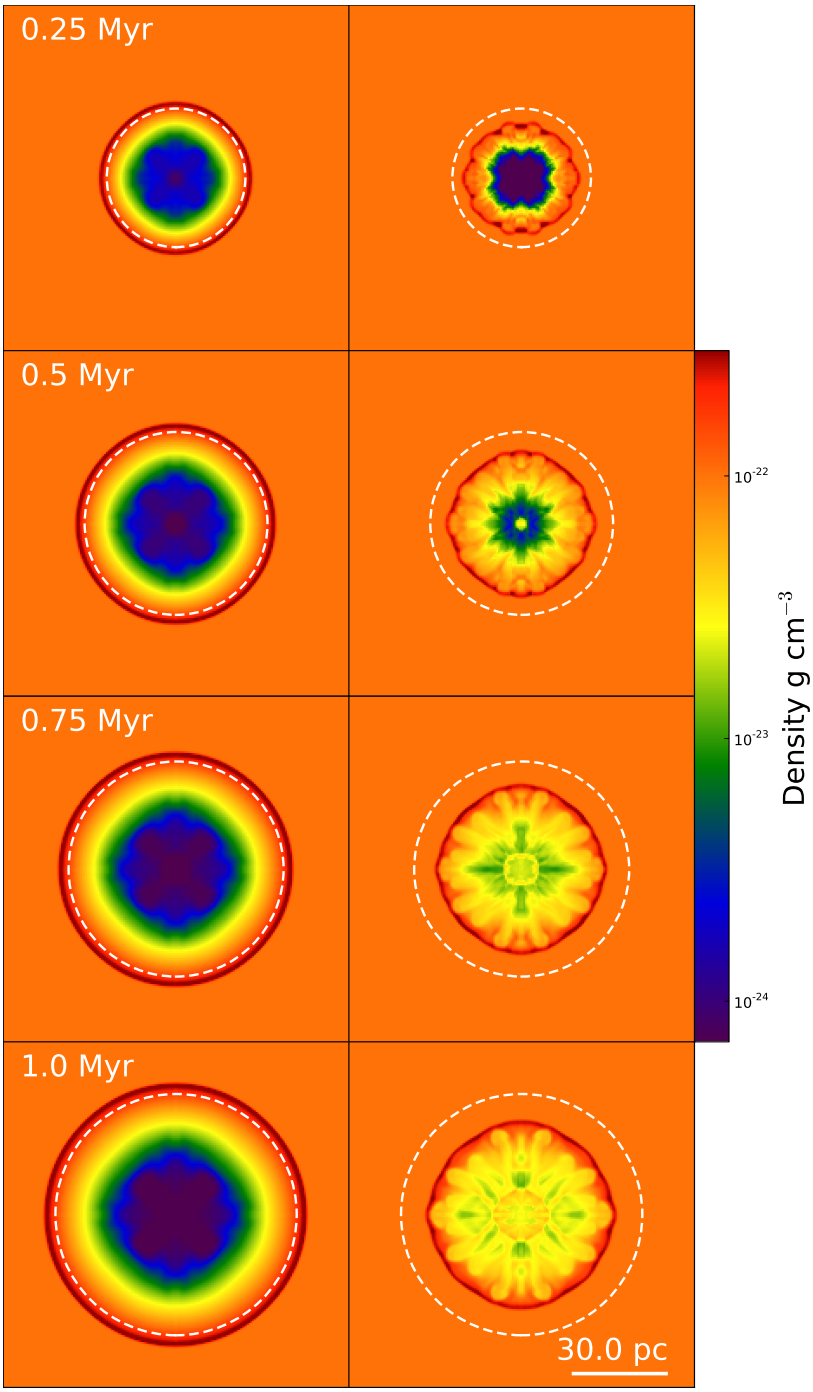

Figure 3.4 Slices of gas density through the center of the feedback region during two tests of the kinetic feedback model conducted at high-resolution. The background density is 100 cm^{-3} and the kinetic injection fraction is set to 0.3. The cell width is 0.5 pc. The simulation on the left does not include cooling and the simulation on the right does. The dashed circles are the size of the analytic prediction for the Sedov blast wave at each time.

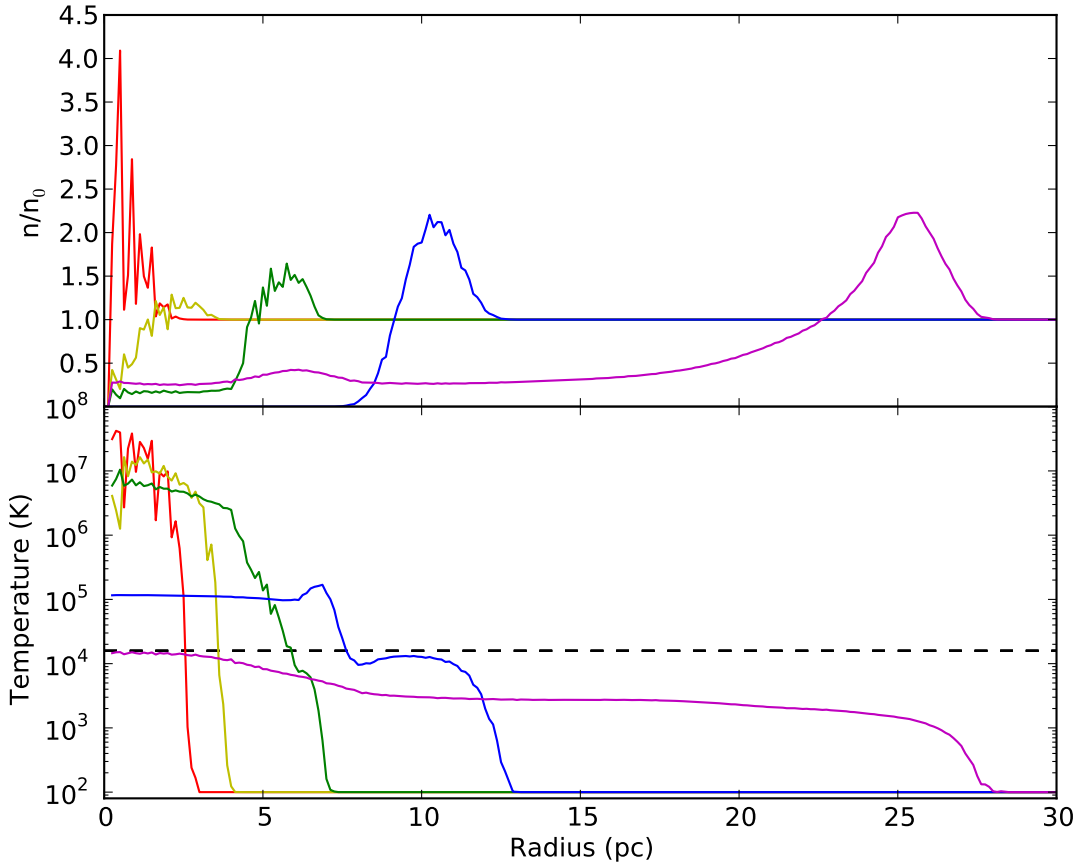

Figure 3.5 Spherically averaged radial profiles of gas density and density weighted gas temperature for a high resolution test simulation of the kinetic feedback model. This simulation includes cooling and is the same simulation presented in the right-hand column of Figure 3.4. The simulation has a background density of 100 cm^{-3} and a kinetic injection fraction of 0.3. Profiles are shown at 10^{-4} Myr (red); 10^{-3} Myr (yellow); 10^{-2} Myr (green); 0.1 Myr (blue); and 1 Myr (magenta). The temperature floor of the cooling curve is shown in the bottom panel as a dashed black line.

propagates outward from the star particle. This shock sweeps up material into a dense shell that reaches an overdensity relative to the background density of approximately 2.5 after 1 Myr. This is less that the overdensity of 4 predicted by shock theory, however, this is likely due to our resolution, as very high resolutions are needed to resolve this very narrow shock feature (Tasker et al. 2008). As we will see, the total mass in the shock matches analytic theory.

We track the evolution of several quantities in each test simulation. We define the shock position as being the radius at which the radial density profile as shown in Figures 3.5 and 3.12 peaks. The shock temperature is defined as the spherical density-weighted average temperature of the gas at this shock radius. The total energy excess in each test simulation is defined as the total energy of the box, both thermal and kinetic, less the initial energy of the box, which is entirely thermal. Similarly, we define the thermal and kinetic energy excesses. The shock mass, or the mass of the dense shell swept up just ahead of the shock front, is defined to be the total mass within the supernova remnant that has an over density relative to the background density greater that 1.1. Figure 3.6 shows the evolution of these quantities for an adiabatic case.

A small amount of excess energy is introduced artificially into these runs by the numerical solver, PPM. This numerical error is small, on the order of a few percent, and more pronounced in simulations with larger initial kinetic energy fractions. This addition of energy is due to the dual energy formalism that corrects for negative thermal energies produced by numerical errors in the advection of momentum.

In the absence of cooling, our test simulations reproduce the analytic Sedov solution for supernova remnants almost exactly. The main deviations from the Sedov solution can

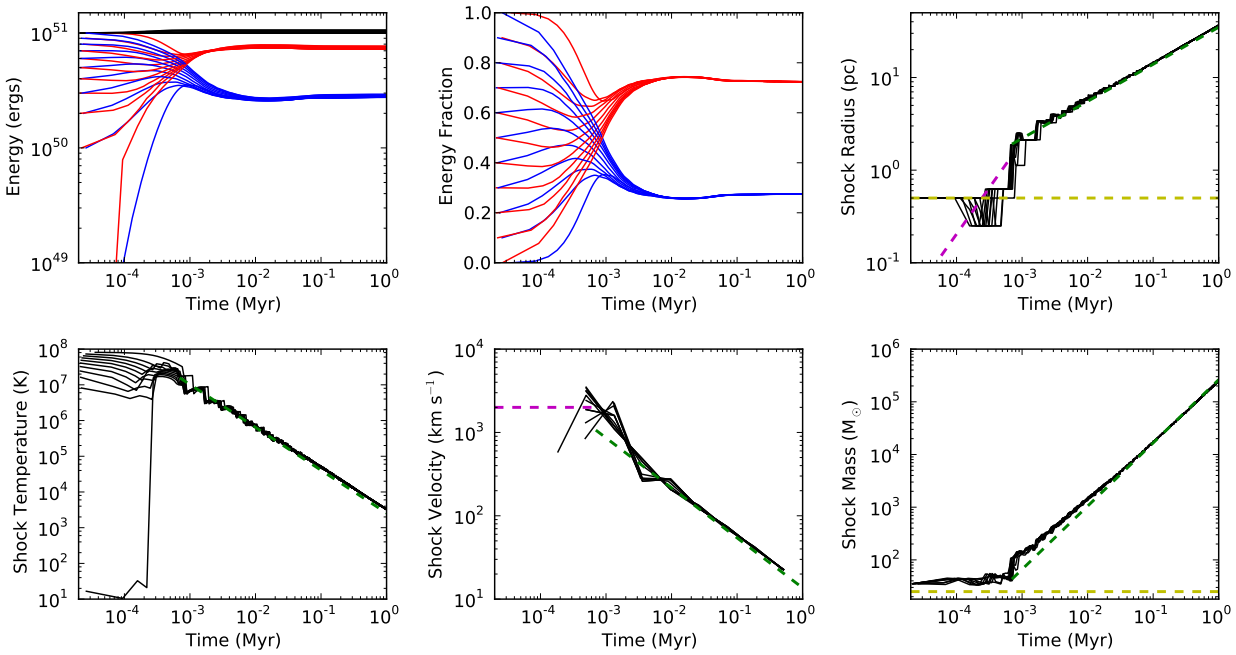

Figure 3.6 High resolution evolution of quantities derived from adiabatic test simulations of the kinetic feedback model conducted in gas with a background density of 100 cm^{-3}. Eleven simulations with kinetic injection fractions ranging from 0 to 1 are presented. *Top Left:* Excess energy in the simulation box. Black is the total energy, red is the thermal energy and blue is kinetic energy. *Top Middle:* Fractions of thermal energy (red) and kinetic energy (blue). *Top Right:* Shock radius. The dashed yellow line is one cell width. The dashed magenta line is the analytically predicted shock radius during the free-expansion phase. The dashed green line is the analytically predicted shock radius during the Sedov phase. *Bottom Left:* Shock temperature. The dashed green line is the analytically predicted shock temperature during the Sedov phase. *Bottom Middle:* Shock velocity as calculated from the shock radius presented in the top right panel. Again, the magenta and green lines are the analytic predictions for this quantity for the free-expansion and Sedov phases. *Bottom Right:* Mass in the expanding dense shell. The dashed yellow line is the total mass the star particle injects into the ISM (25 M$_\odot$). The dashed green line is the analytic prediction of the Sedov solution. Note that coarser resolution simulations take larger time steps and therefore the starting time of simulations with larger cell widths are shifted to later times.

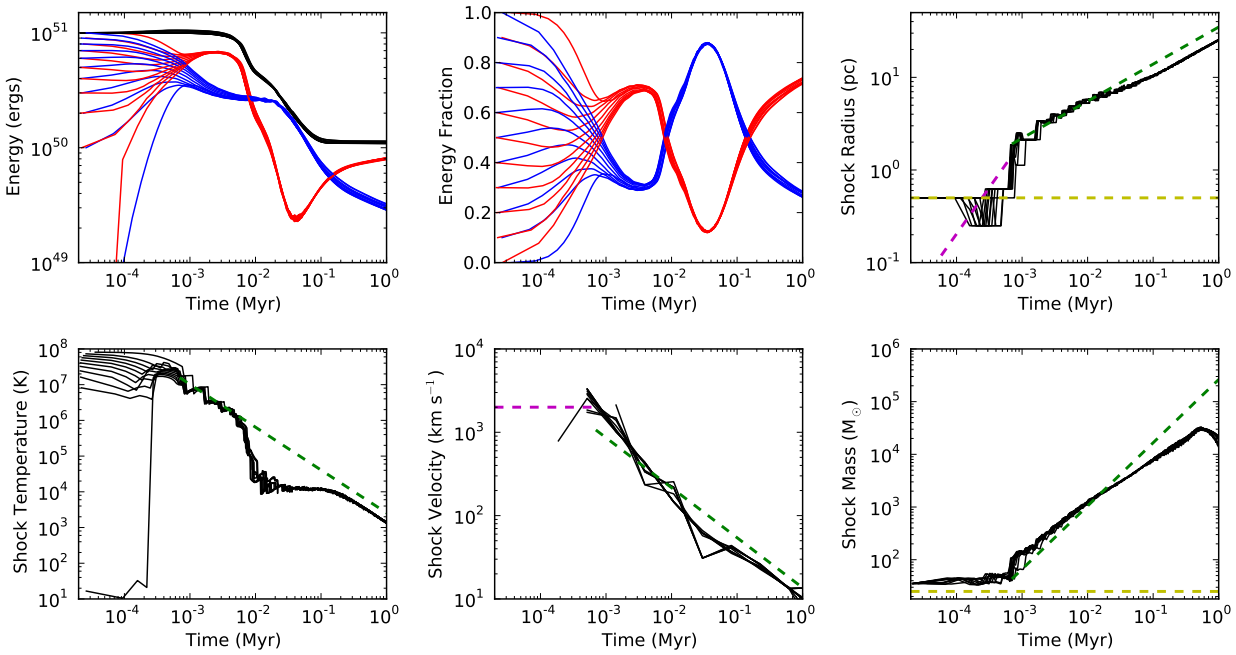

Figure 3.7 High resolution evolution of quantities derived from test simulations of the kinetic feedback model with cooling. The quantities presented are the same as those shown in Figure 3.6.

be seen early in the simulations and appear to roughly approximate the evolution during the free expansion phase that precedes the Sedov phase. This transition is thought to occur when the mass of the ISM swept up by the expanding shock becomes equal to the mass ejected by the star. In our simulations, once the shock mass reaches roughly 50 $M_\odot$, which is twice the ejection mass, there is an abrupt jump in the shock mass above 100 $M_\odot$, and all quantities appear to begin to asymptote to the analytic Sedov solution. The final fraction of kinetic energy found is 25%, close to the value of 28% found by integrating the Sedov prediction for the radial profiles of energy and close to the values of roughly 30% found in other numerical models of supernova remnants (Chevalier 1974; Cox 1972).

Figure 3.7 presents the evolution of the kinetic feedback model in the presence of cooling. Simulated at high resolution, we see that it takes about 10^4 years before cooling

causes deviations from the analytic Sedov solution and the remnant enters the snow-plow phase. As cooling becomes more and more effective, the temperature of the shock drops precipitously and reaches a plateau of 10^4 K. The simple cooling curve we assume for these test simulations has a cooling floor close to this temperature. The total energy continues to decline, but at a decreasing rate. The shock temperature presents the temperature of gas at a single radius, but there continues to be hotter gas interior to this radius as seen in Figure 3.5. During this time the kinetic energy exceeds the thermal energy by a large margin as energy inside the remnant continues to cool. As the dense shell swept up by the shock continues to expand due to its own momentum, more ISM gas is swept up, however the shock is now isothermal, so as mass is added to the shell, the thermal energy begins to increase, while the shock temperature remains the same. However, after 0.1 Myr, the energy losses cease as the shell of dense gas begins to decline in mass, halting the increase in thermal energy.

The final energy that these simulations settle to is dependent on the cooling curve we have assumed. The plateau seen in the shock temperature reflects the floor of the cooling curve we have assumed.

In the high resolution simulations presented here, we see that the evolution of the supernova remnant is entirely insensitive to the initial fraction of kinetic energy. In both the case with cooling and without cooling, it takes a few 100 years for simulations with different initial kinetic fractions to equilibrate, but after this period all simulations behave in the same way. We will now explore how this behavior changes or remains the same at coarser resolution, with different background densities and with different numerical solvers.

3.3.3 The dual effects of background density and resolution

We have explored in detail the behavior of our model at a relatively high resolution and in high background density gas, similar in density to the density threshold for star formation in our galaxy models. Now we will explore the effect of changing background density and resolution on the evolution of supernova heated gas. Figures 3.8 and 3.9 present the evolution of test simulations run at two different background densities, 1 and 100 cm^{-3}, and at five different test resolutions, 0.5, 1.0, 2.0, 4.0 and 8.0 pc per cell width. For each background density and resolution, a range of kinetic injection fractions varying from zero to one are tested. These models were conducted with PPM.

First, it is apparent that at lower background densities these test simulations behave very similarly, regardless of the kinetic injection fraction or resolution. Not only do simulations with the same resolution and different kinetic injection fractions behave very similarly, simulations of different resolution do not differ much either, with the slight exception of the most coarsely resolved set of simulations with a cell width of 8 pc. However, even this slightly deviant case appears briefly to reach a rough approximation to the Sedov phase, bringing its final state in line with the finer resolution simulations.

At a higher background density, this uniformity in behavior breaks down. As we have discussed, at very high resolution (Δx = 0.5 pc), the kinetic injection fraction makes no difference in later behavior. This largely holds for simulations with the next two finer resolutions (Δx = 1.0 pc and 2.0 pc). However, in the two most coarsely resolved sets of simulations where Δx = 4 pc and 8 pc, simulations with different kinetic injection fractions end with very different total energies.

How can we understand these transitions in behavior? A simulation with a given

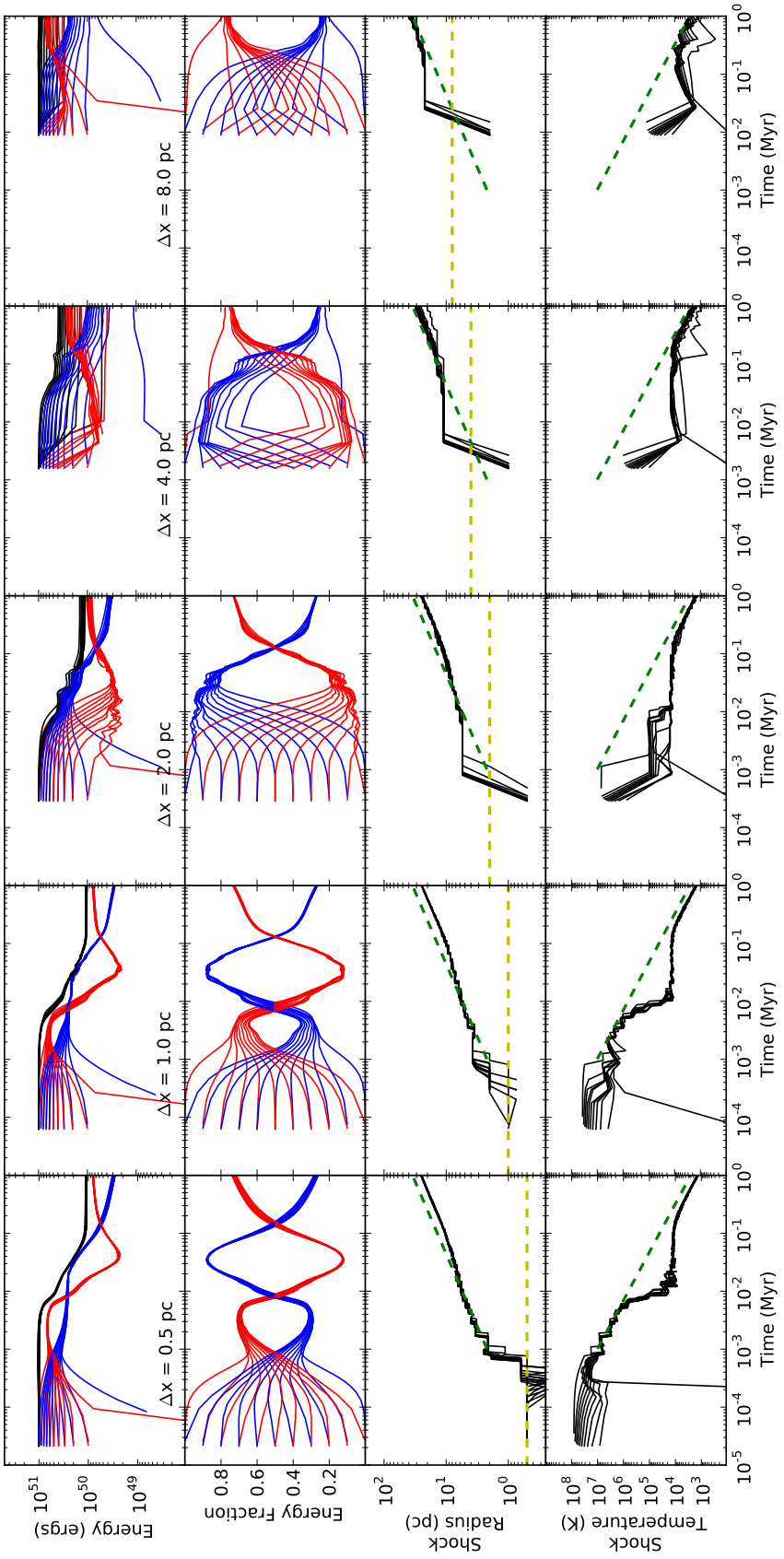

Figure 3.8 Evolution of the excess energy, thermal and kinetic energy fractions, the shock radius and the shock temperature for simulations with an initial background density of 100 cm^{-3}. The colors of lines are the same as in Figure 3.6. Analytic predictions of the Sedov phase are shown with dashed green lines and the cell width is shown as a dashed yellow line in the third row. Each column presents simulations with a different resolution Δx. Each panel presents several simulations with different kinetic injection fractions.

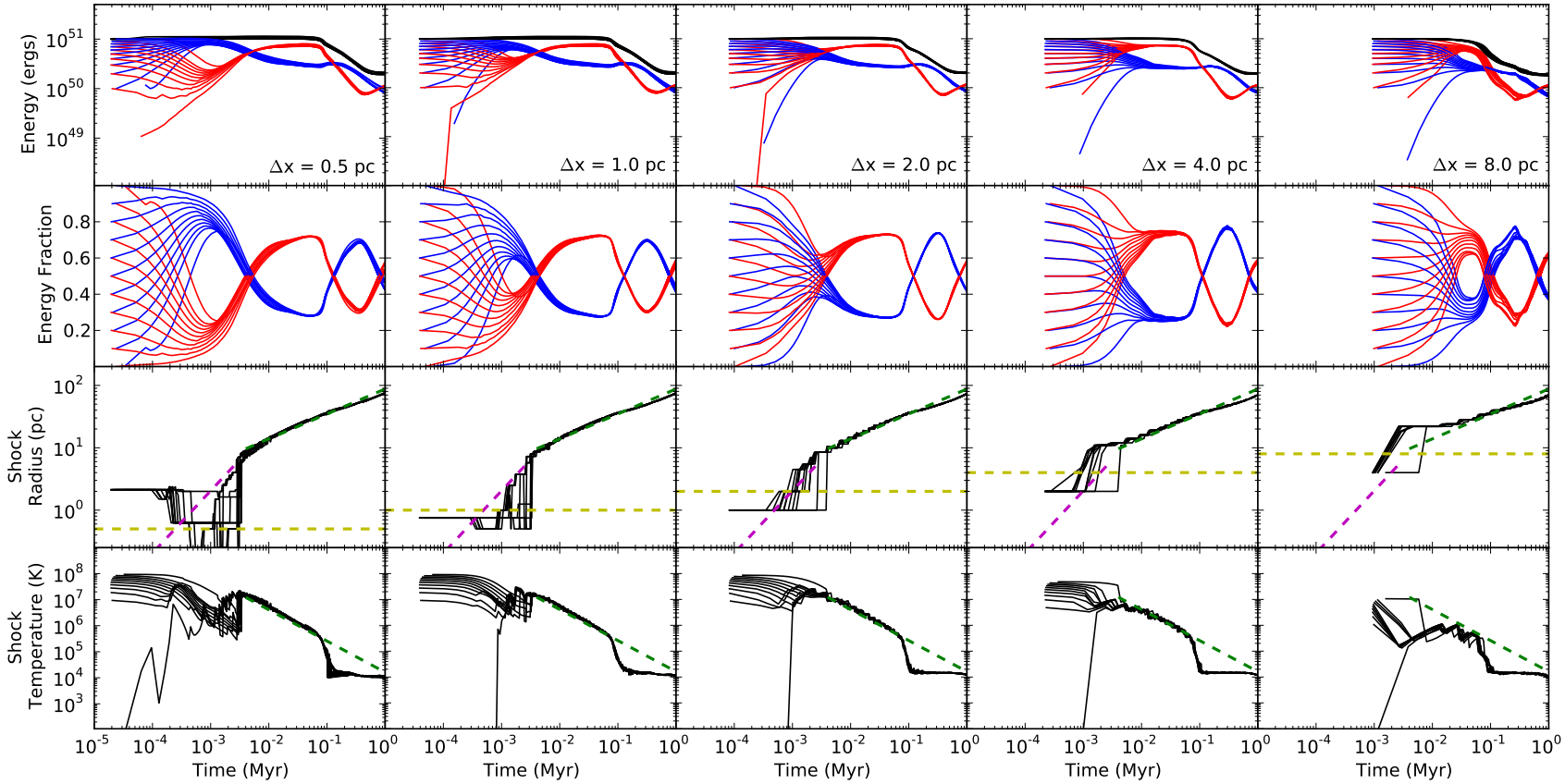

Figure 3.9 Evolution of the excess energy, thermal and kinetic energy fractions, the shock radius and the shock temperature for simulations with an initial background density of 1 cm^{-3}. The colors of lines are the same as in Figure 3.6. Analytic predictions of the Sedov phase are shown with dashed green lines and the cell width is shown as a dashed yellow line in the third row. Each column presents simulations with a different resolution Δx. Each panel presents simulations with different kinetic injection fractions.

background density, resolution and kinetic injection fraction appears to pass through three phases of evolution. The first phase is a numerical equilibrium phase. During this phase, the blast wave is still localized in the initial energy injection site, where its evolution is dominated by the cubical discritization of the hydrodynamical calculation. Before the heated region can begin to reach a regime dominated by physical processes, the remnant must first clear this resolution dominated region. We estimate the size of this region to be three times the size of the initial injection region. The timescale for this phase is therefore approximately the time it takes the blast radius to reach three times the radius of the energy injection region, or equivalently, the time at which the shock radius reaches $4.5\Delta x$. This resolution timescale $t_{\Delta x}$ can be determined from the evolution of the shock radius presented in Figures 3.8 and 3.9.

The second timescale we will consider is the time at which the behavior of the remnant begins to approximate the evolution of the analytic Sedov solution. Physically, the transition from the free-expansion phase to the Sedov phase is thought to occur when the mass of the ISM swept up by the expanding shock is equal to the mass ejected by the star. We have chosen to let star particles eject 25 $M_\odot$ into the ISM, however as we have discussed, the initial evolution is dominated by numerical effects of the local grid. This local grid contains mass and it would be more appropriate in our context to consider a numerical ejection mass equal to the ejection mass plus the mass of ISM in the initial feedback zone of 3^3 cells. We therefore define the Sedov equilibrium timescale to be the time t_{eq} when the swept up mass is equal to twice this numerical ejection mass. We can estimate the mass of swept up ISM from the shock radius and the background density.

The third relevant timescale is the time at which the evolution of the supernova

remnant enters the snow-plow phase. This is a physical transition we expect to happen in real systems but is dependent in numerical simulations on the cooling assumed. Following Draine (2011) we define this timescale (t_{snow}) to be the time at which the energy of the remnant has dropped by one third of its original value. We will note that this level of energy loss typically happens well before the shock temperature reaches the cooling floor, and therefore it is not dependent on our choice of cooling floor.

Figure 3.10 shows these three characteristic timescales for four sets of simulations with different background densities and at each background density, we have conducted test simulations with different kinetic injection fractions and resolutions.

We see that $t_{\Delta x}$ rises with increasing cell width Δx, and the steepness of this rise increases with increasing background density. Simulations with low kinetic injection fractions also have slightly longer resolution timescales. These trends can be explained by the expectation that simulations with larger cells and simulations where the supernova ejecta have lower initial velocities will take longer to expand beyond the resolution dominated region.

At the lowest density ($n_0 = 1\,\mathrm{cm}^{-3}$), t_{eq} and t_{snow} are constant over Δx and t_{snow} remains greater than $t_{\Delta x}$ for all Δx except the very largest. In this regime, the supernova remnant equilibrates to the Sedov solution before energy losses due to cooling become significant and it enters the snow-plow phase.

At the two next higher densities ($n_0 = 10\,\mathrm{cm}^{-3}$ and $100\,\mathrm{cm}^{-3}$), $t_{\Delta x}$ becomes significantly greater than t_{snow} at coarser resolutions. This means that the supernova remnant has not yet cleared the resolution dominated region before energy losses due to cooling become significant. The result is that the snow-plow time becomes much more dependent on

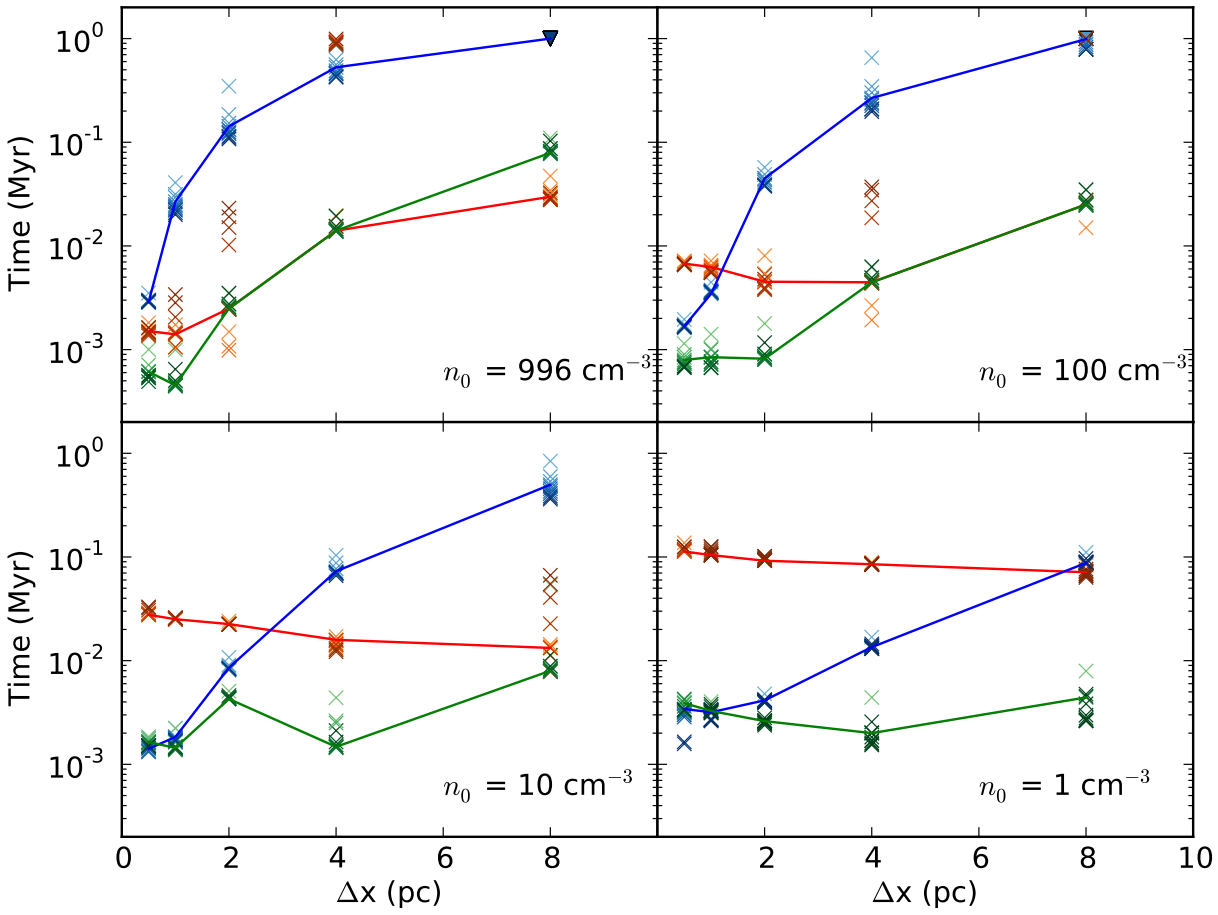

Figure 3.10 The four panels shown present $t_{\Delta x}$ (blue), t_{eq} (green) and t_{snow} (red) for simulations run with four different background densities n_0. The darker the shade of the data point the higher the kinetic energy fraction is for the simulation represented by that data point. In some cases, the t_{eq} exceeded the maximum time of the simulation; these cases are denoted by triangles plotted at 1 Myr. To guide the eye, lines of the corresponding color connect simulations with f_{kin} = 0.3 between different resolutions.

the kinetic injection fraction. Simulations with higher kinetic injection fractions have significantly larger t_{snow} when $t_{\Delta x}$ is much greater than t_{snow}. This difference is because the conversion of kinetic energy to thermal energy in the expanding shock is impeded when $t_{\Delta x}$ is long, and so with more energy locked up in kinetic form, less thermal energy is available to be dissipated and the time it takes for total energy to drop significantly is much longer.

At the very highest density probed ($n_0 = 1000$ cm^{-3}), $t_{\Delta x}$ is longer than t_{snow} at all resolutions tested. In this regime, the Sedov phase and the snow-plow phase cannot be well separated. The snow-plow timescale and the Sedov equilibrium timescale happen at the same time because the conversion between thermal and kinetic energies is so inefficient when $t_{\Delta x}$ is long that the remnant cannot equilibrate before cooling begins to take over. The increase of t_{snow} with increasing cell width is apparent at the two highest background densities. From Figure 3.8, this trend is likely due to the low initial temperatures reached by heated gas. In these test simulations the specific heating rate is low at low resolution, resulting in lower cooling rates and a longer t_{snow}.

3.3.4 The effect of numerical solvers

To this point, we have only considered tests of our new feedback method done with the PPM hydrodynamical solver. The simulations conducted in chapter 2 were done with the ZEUS solver, which is more suited to complex galaxy simulations because of its greater numerical robustness. ZEUS has some features which may impact the evolution of supernova heated gas. Specifically, ZEUS is not an energy conserving method, and small amounts of numerical energy dissipation are expected with this solver. As we have seen,

the PPM solver employed with the dual energy formalism is not without its own energy conservation issues, but overall, we expect PPM to produce a higher fidelity solution in shock problems, as has been shown in other work (Tasker et al. 2008).

Figure 3.11 compares the spatial evolution of several test simulations done with PPM and ZEUS. As we can see, the overall size of the supernova heated remnant is approximately the same in both cases, but the evolution in the ZEUS simulation is highly asymmetric. Tasker et al. (2008) found in much higher resolution calculations of a Sedov blast wave that at early times the shock has a diamond shape relative to the grid. In our calculation, the feedback zone is off center slightly. If the shape aberrations seen by Tasker et al. (2008) are an artifact from the cartesian grid, this offset may explain the asymmetry.

Despite this asymmetry, we track quantities derived from spherically averaged radial profiles such as the ones shown in Figure 3.12. The radial profiles for the ZEUS simulations are less well defined than those for PPM simulations, however for simulations with large cells the resolution is the dominant source of uncertainty in determining the shock radius. As Figure 3.12 shows the radius of the peak density agrees between both simulations to within a few cell widths.

In adiabatic tests with the ZEUS solver, numerical energy losses range between 35% and 45% as shown in Figure 3.13. This energy loss is somewhat greater than the 25% found by Tasker et al. (2008). When we include cooling, we find that the drop in the total energy and the evolution of other simulation properties are very similar to those found in the analogous simulations run with PPM. A set of example test simulations demonstrating this is shown in Figure 3.14, which can be compared to Figure 3.8 that shows the evolution of the same test simulations with PPM. From this comparison, it can be concluded that the

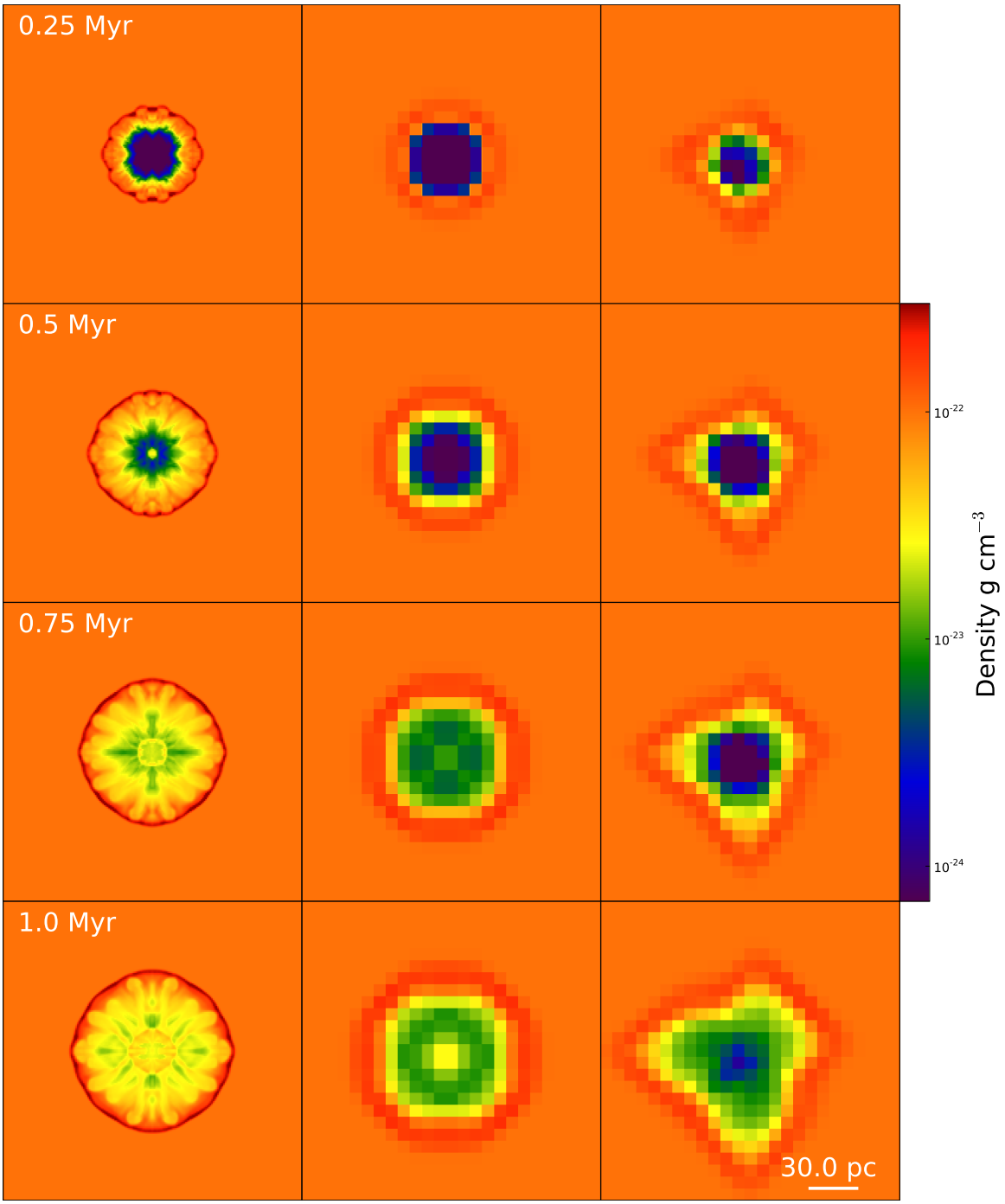

Figure 3.11 Slices of gas density through the center of the feedback region during three tests of the kinetic feedback model conducted at resolutions of 0.5 pc (left column) and 4 pc (middle and right column). The background density is 100 cm^{-3} and the kinetic injection fraction is set to 0.3. All three simulations include cooling.

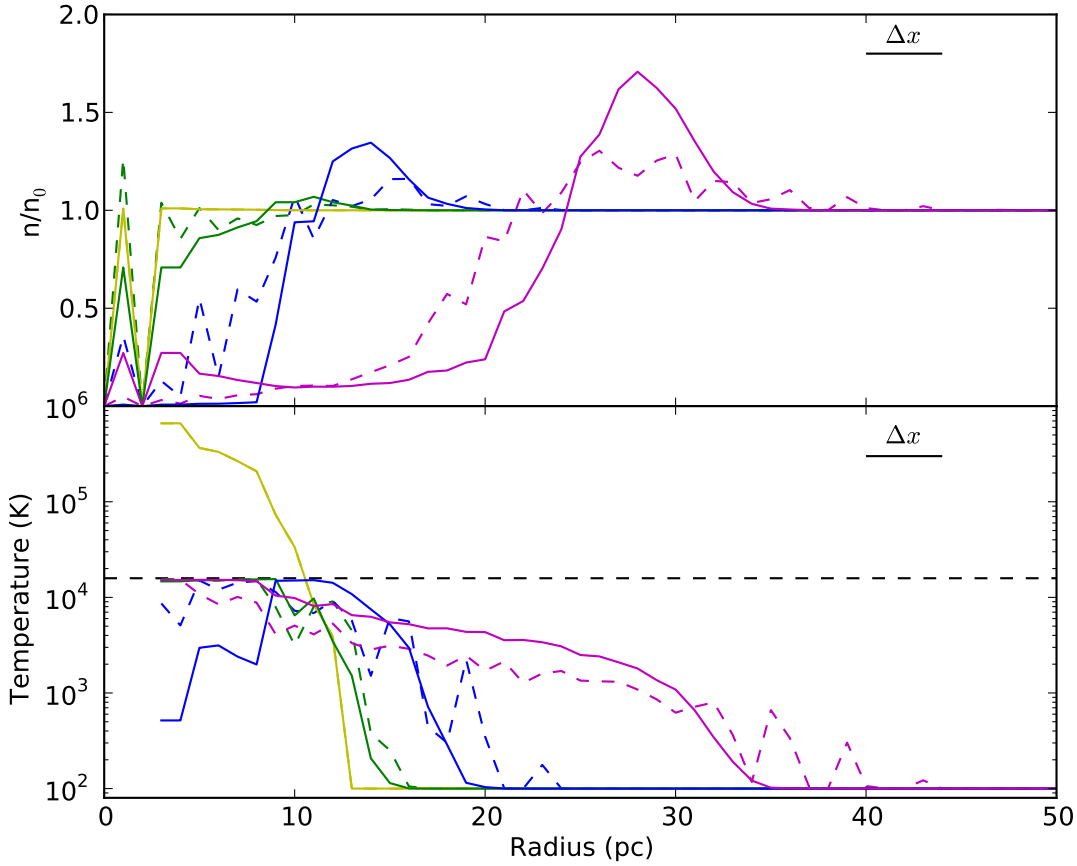

Figure 3.12 Spherically averaged radial profiles of gas density and density weighted gas temperature for two test simulations run with the hydrodynamic solver PPM (solid lines) and ZEUS (dashed lines). These simulations both have a resolution of 4 pc per cell and include cooling. These simulations both have a background density of 100 cm^{-3} and a kinetic injection fraction of 0.3. Profiles are shown at 1.7×10^{-3} Myr (yellow); 10^{-2} Myr (green); 0.1 Myr (blue); and 1 Myr (magenta). Note that the profiles for the PPM and ZEUS simulations at 1.7×10^{-3} Myr are so similar that they lie on top of each other. The temperature floor of the cooling curve is shown in the bottom panel as a dashed black line. The width of one cell is denoted by a solid black line in both panels.

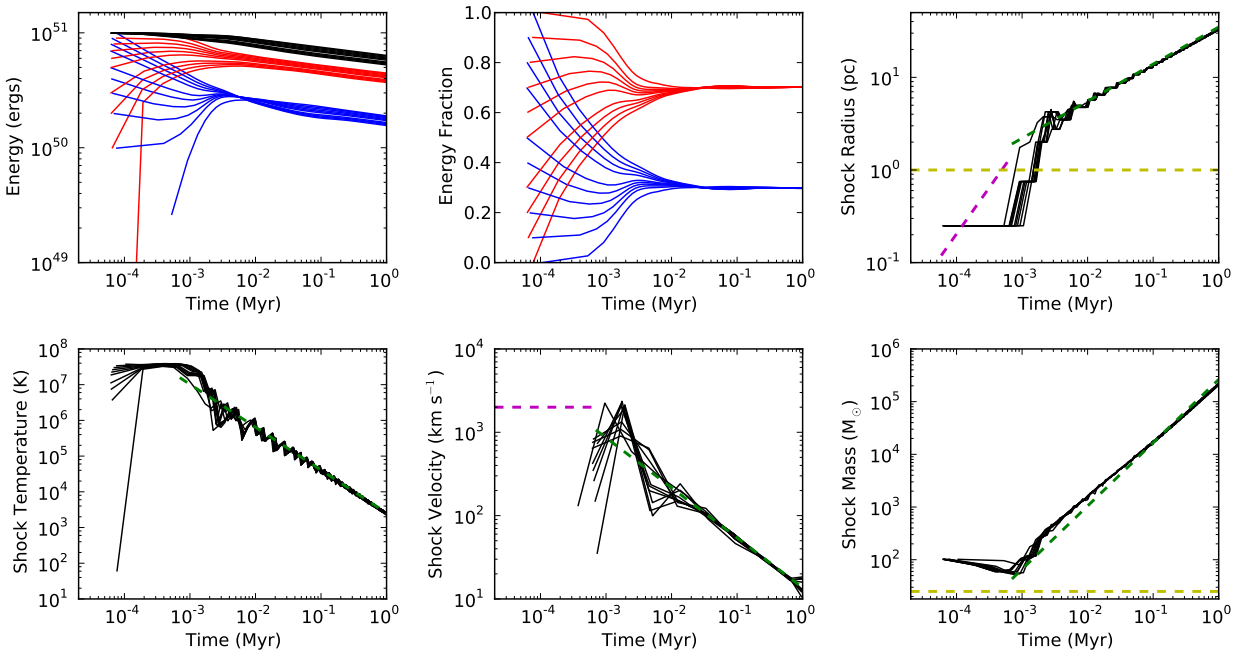

Figure 3.13 Evolution of quantities derived from adiabatic test simulations of the kinetic feedback model run with the ZEUS hydrodynamical solver. The resolution of these tests is 1 pc per cell width and the background density is 100 cm^{-3}. No cooling is included in these simulations. The quantities presented are the same as those shown in Figure 3.6.

effect of numerical energy dissipation will be masked by radiative energy dissipation in simulations conducted with the ZEUS solver, even in situations that include only modest cooling such as we have done in these test simulations.

3.4 Summary of feedback methods

We have explored both the single cell thermal feedback model used in Chapter 2 and a new feedback method that includes kinetic energy. We have conducted simple test simulations with a range of resolutions and in media with a range of densities. The total amount of energy retained in gas heated by these two models depends greatly on the details of the cooling curve assumed, so it is difficult to make a comparison between the two models

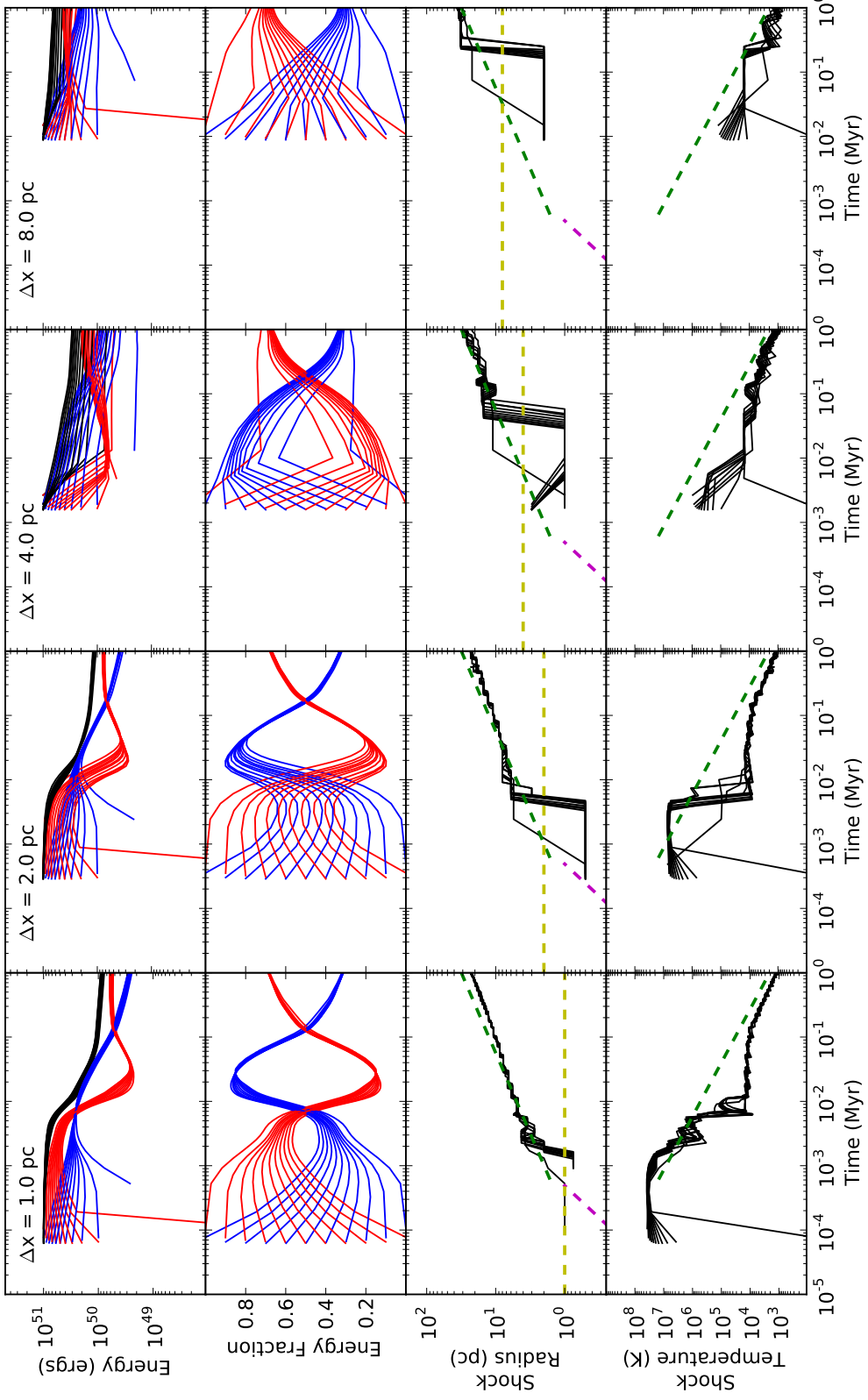

Figure 3.14 Evolution of the excess energy, thermal and kinetic energy fractions, the shock radius and the shock temperature for simulations with an initial background density of 100 cm^{-3} run with the ZEUS solver. Line colors are the same as in Figure 3.8. Each column presents simulations with a different resolution Δx. Each panel presents several simulations with different kinetic injection fractions ranging from zero to one.

on that basis. What can be noted is that the new model, because of its short injection timescale, has the ability to accelerate gas much more quickly than the old model, which may impact the metal fraction of the ISM. At coarse resolutions, it takes the new model a few fractions of a Myr to increase the kinetic fraction of surrounding gas to well above 20%. In the old model, in addition to the energy release being gradual, the fraction of kinetic energy reaches large values in only the low density ISM case.

Our new model is better physically motivated for the resolutions we are simulating. We have established how it will behave in gas of different densities and at different resolutions. This new method does introduce a new tunable parameter, the kinetic injection fraction f_{kin}. At low ISM densities, of order 1 cm^{-3}, the value of f_{kin} does not matter to the evolution of feedback affected gas at the resolutions we have tested. At higher densities, the value of f_{kin} will matter a great deal at resolutions of a few parsecs.

In the galaxy models in Chapter 2, star forming cells were required to be 10^5 times the mean density of the universe at a given redshift, which roughly corresponds to densities between a few tens of particles per cm^3 to a few hundred particles per cm^3 during the epoch of star formation During this epoch, the minimum cell width was typically a few parsecs. An application of our new feedback method to this type of star formation would therefore operate in the regime where the f_{kin} plays an important role in the evolution of feedback affected gas.

The difference f_{kin} makes to the final energy of the supernova affected medium depends on the cooling function. An application to a galaxy model that includes more realistic cooling is therefore the next step in understanding how this model operates.

Chapter 4

Kinetic Feedback in Galaxy Simulations

In this chapter, we will combine the kinetic supernova feedback method described and tested in Chapter 3 with the galaxy models presented in Chapter 2 to better understand the effect of kinetic energy injection from supernovae as well as the effect of prompt energy injection on the evolution of the baryon content of a low mass dark matter halo. This preliminary application presents some new challenges and insights into the realistic simulation of supernova feedback at high resolutions. We have implemented the new supernova feedback model into the same code used for the simulations presented in Chapter 2 and have applied it to the same cosmological 10^9 $M_\odot$ dwarf halo also explored in Chapter 2. This chapter will begin with a detailed description of the implementation of the new kinetic feedback method into our galaxy model and then will present some important ways these new models differ from those presented in Chapter 2. We will conclude by connecting these results to the test simulations discussed in Chapter 3.

4.1 Implementation of kinetic feedback in a cosmological galaxy simulation

For these simulations, we use the same cosmological initial conditions, cooling prescriptions and multispecies solver, metagalactic UV backgrounds, and self-shielding approximations as described in Section 2.1. We turn on the metagalactic UV backgrounds late, between redshifts 6 and 7, in the same way as done in simulation R10. We allow a maximum of twelve levels of AMR beyond the root grid, as was done in simulation R10, giving these calculations a minimum allowed cell width of 10.8 comoving pc.

The new feedback model allows for the injection of energy on short timescales, which we found challenging with the previous method. We choose to inject all the energy, mass and metals produced by supernova feedback in a single time step. We also choose to inject the supernova energy promptly, immediately after the creation of the star particle, mimicking Type II supernovae, but neglecting the significant contributions from Type Ia supernovae, which can be delayed from the epoch of their progenitor's creation by as much as a Gyr.

The total amount of specific supernova energy produced by each star particle is fixed to be the same as in simulation R10. This value is chosen such that 150 $M_\odot$ of star particles inject 10^{51} ergs of energy into the ISM. What differs in these new simulations is the fraction of this energy that takes an initially kinetic form rather than an initially thermal form. This value is a free parameter, f_{kin}, that we will modify and test. As in Chapter 2, star particles return 25% of their mass to the ISM during feedback. Star particles also return metals to the ISM during feedback and the supernova metal yield is assumed to be 2%; all the

metals produced by star particles contribute to a single mean metallicity field. We assume the same criteria for star particle creation as outlined in Section 2.1.4. As in Chapter 2, this set of simulations does not include any pre-supernova stellar feedback such as UV radiation from young stars or stellar winds.

A few adjustments not detailed in Chapter 3 were required for the galaxy application of the kinetic feedback model. Enzo partitions the simulation domain into simply connected blocks of space with uniform resolution that are called 'grids.' Enzo solves Euler's equations on these grids separately as a strategy for distributing the required calculations across many processors working in parallel. During the evolution of a single time step on the the coarsest level of refinement, called the root grid, spatially contiguous grids do not communicate with one another. Therefore, star particles whose feedback zones straddle grid boundaries cannot properly deposit their energy, mass and metals into the gas.

To account for this problem, we have shifted feedback zones away from grid boundaries as needed in order to fit entire feedback zones onto their host grids. Since all our supernova feedback is prompt, i.e. occurring immediately after the star particle's creation at the center of its birth cell, feedback zones never need to be shifted by more than one cell in a given direction, which is only one third the width of the feedback zone. In Chapter 3, many of the idealized test simulations were conducted in parallel, however, with the comparatively simple simulation set-up, we were able to force grid partitioning to accommodate the feedback zone, making this adjustment unnecessary. We will more precisely address this issue in future work by allowing communication between grids.

Unlike our idealized simulations, in the galaxy simulations we do not adjust the time step of the grid in anticipation of the energetic feedback. This necessitated lowering

the courant safety condition, which lowered the time step computed for all grids, an inefficiency which may also be addressed in future work.

4.2 Galaxy simulations

We have conducted two galaxy simulations to test the new supernova feedback model: one simulation with a kinetic injection fraction of 0, called R10-kinf-0 and another simulation with a kinetic injection fraction of 0.3, called R10-kinf-0.3. These two simulations will provide insight on the relative importance of the two new effects introduced by this feedback model: kinetic energy injection and quick energy injection. R10-kinf-0 injects entirely thermal energy into the ISM like R10, but unlike R10, it performs this injection in a single time step.

The simulation R10-kinf-0.3 introduces the added ingredient of 30% injected kinetic energy. This value for f_{kin} is approximately the kinetic equilibrium fraction predicted from the analytic Sedov solution and reproduced by high-resolution adiabatic models in Chapter 3. This choice of f_{kin} is one in a range of values that may be physically relevant, depending on resolution, and further testing is required to fully understand its impact. The idealized test simulations in Chapter 3 show that at high enough resolution and in dense media, feedback affected gas is driven to a Sedov phase that has this fraction of kinetic energy. The typical resolution of R10-kinf-0.3 is coarser that this convergence resolution, but this value of f_{kin} is a natural first choice.

As we will discuss, star formation is greatly enhanced in simulation R10-kinf-0. Due to its higher star formation rate, R10-kinf-0 was considerably slower computationally

Table 4.1 Summary of Kinetic Feedback Galaxy Simulations.

	R10	R10-kinf-0*	R10-kinf-0.3
$M_{tot}/M_\odot$	1.55×10^9	9.80×10^8	1.61×10^9
$M_*/M_\odot$	1.43×10^6	4.84×10^6	1.97×10^5
M_{gas}/M_{tot}	3.24×10^{-3}	6.82×10^{-3}	3.26×10^{-3}
r_{200} (kpc)	23.7	13.9	24.0
$r_{1/2}$ (pc)	704	439	1048
$M_{1/2}/M_\odot$	3.05×10^7	1.89×10^7	5.28×10^7
$M_{300}/M_\odot$	7.53×10^6	1.14×10^7	5.95×10^6
$\sigma_{1/2}$ (km/s)	7.83	8.54	9.76
Log($\langle Z/Z_\odot \rangle$) (median)	-0.29	0.15	-1.58
Log($\langle Z/Z_\odot \rangle$) (mean)	-0.076	0.29	-1.57
$\sigma_Z/Z_\odot$	0.84	2.00	0.02

Note: The quantities presented in each row are (1) the total mass within r_{200}, (2) the total stellar mass within r_{200}, (3) the total gas fraction within r_{200}, (3) r_{200}, the radius within which the mean halo density is 200 times the critical density of the universe, (4) the radius enclosing half the stellar mass, (5) the total mass within $r_{1/2}$, (6) the total mass within 300 pc, (7) the velocity dispersion of star particles within $r_{1/2}$, (8) the mass-weighted median of the star particle metallicities, (9) the mass-weighted mean of the star particle metallicities, (10) the mass-weighted standard deviation of the star particle metallicities.

* Simulation R10-kinf-0 was only run to a redshift of 0.92; therefore, the quantities presented here are for the target halo at this redshift.

than R10 or R10-kinf-0.3. We therefore only ran R10-kinf-0 to a redshift of 0.92. By this redshift, the differences in evolution between R10-kinf-0 and the other models tested are apparent as well as its fidelity (or lack thereof) with observed systems. Halo properties in R10-kinf-0.3 and R10-kinf-0 are summarized Table 4.1.

4.2.1 Global properties

Global halo properties in R10-kinf-0 and R10-kinf-0.3 exhibit many similarities and differences both relative to those of R10 and each other as a consequence of the different feedback prescriptions employed. Figure 4.1 shows the evolution of several key properties.

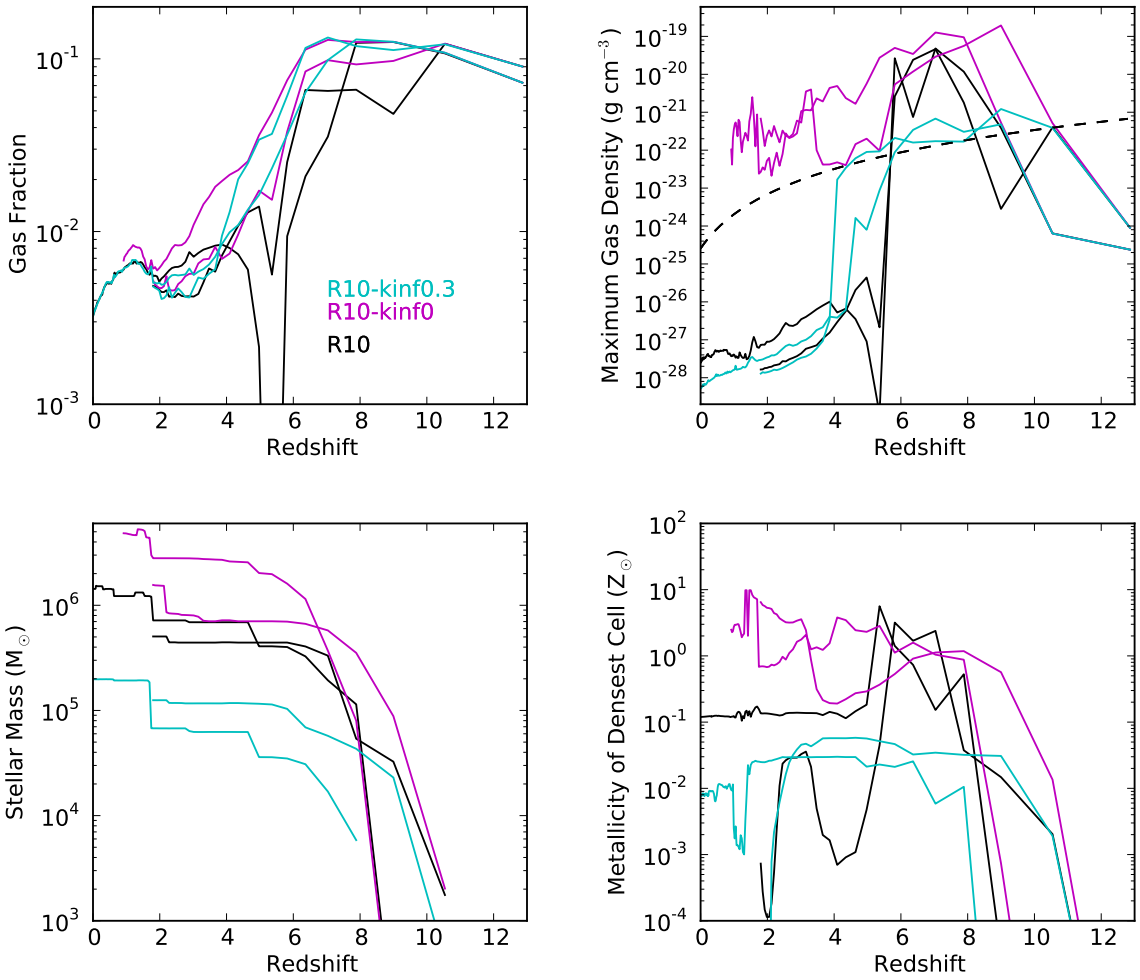

Figure 4.1 Evolution of properties for two massive progenitors in simulations R10 (black), R10-kinf-0 (magenta) and R10-kinf-0.3 (cyan). R10-kinf-0 was not run past a redshift of 0.92. The properties shown here are the halo gas fraction within the r_{200} radius (top left); the density of the densest cell within each halo (top right); the stellar mass within the r_{200} radius for each halo (bottom left); and the gas metallicity of the densest cell within each halo (bottom right). The density threshold for star formation is shown as a dashed line in the top right panel showing the peak gas density.

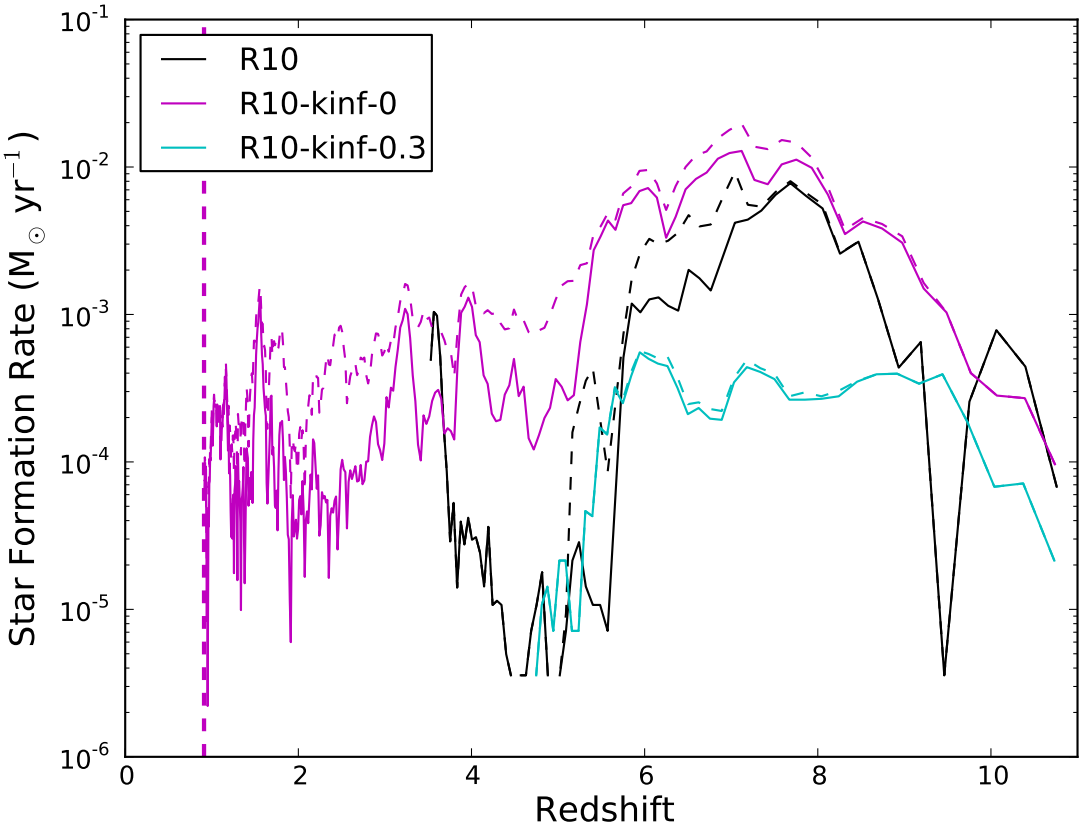

Figure 4.2 Star formation rate in simulations R10 (black), R10-kinf-0 (magenta) and R10-kinf-0.3 (cyan). Solid lines show the star formation rate for the stellar population that ends the simulation within r_{200} of the final target halo. Dashed lines show the global star formation rate for all star particles formed in the simulation volume. Simulation R10-kinf-0 terminates at $z = 0.92$, which is indicated by a vertical thick dashed magenta line.

The overall evolution of the halo gas fraction is very similar in each of these simulations, with all three demonstrating large drops in the halo gas fraction following the onset of reionization, which is introduced between redshifts 6 and 7. This drop is consistent with the analysis presented in Chapter 2 that found that the photoioninzing background was the key factor in setting halos' gas fractions by driving photoevaporative winds.

In R10, several halos, including one of the two massive progenitors, exhibit drops in gas fraction prior to reionization that are due to supernova feedback. In neither R10-kinf-0 nor R10-kinf-0.3 are these types of drops apparent. While supernova feedback is not the dominant mechanism for gas ejection in any of the models we have tested, the quick injection of energy and mass done in the new model appears to be much less effective in expelling gas as the gradual injection done with the old model.

The evolution of dense gas is quite different between the three models. The slow injection of thermal energy done in R10 appears to be effective in destroying self-shielded clumps of dense gas after reionization, unlike the quick injection of thermal energy done in R10-kinf-0, where dense clumps survive to late times and continue to form stars. In both R10 and R10-kinf-0, the maximum gas density in massive star-forming halos continues to rise significantly after the onset of star formation. In R10-kinf-0.3, however, the maximum gas density in these halos appears to follow closely the density threshold for star formation chosen in our models. This trend indicates that supernova feedback very closely regulates star formation in this model, i.e. once gas becomes dense enough to form stars, the feedback produced is able to prevent further collapse and thereby maintains the density of gas at the star-forming threshold.

This self-regulating behavior in R10-kinf-0.3 has the result that the calculation does

not reach the very highest levels of resolution allowed in the simulation because the refinement of the cartesian mesh on the highest levels is primarily triggered by gas density, which is suppressed. In all three simulations, the first star particles form at $z > 10$ on AMR level 9, where the resolution is less than 7.9 physical pc. In R10 and R10-kinf-0, the AMR hierarchy quickly reaches the maximum allowed level of AMR (level 12), which has a comoving resolution of 10.8 pc. In R10-kinf-0.3, the AMR hierarchy does not descend below level 10, which has a physical resolution of 8.6 pc at redshift 4.

The star formation rate in R10-kinf-0 and R10-kinf-0.3 follows the evolution of dense gas as it does in R10. Figure 4.2 shows the star formation rate in all three simulations. The star formation rates in R10 and R10-kinf-0 steadily rise until reionization, when they begin to decline. Star formation in R10-kinf-0 continues to late times at a reduced rate from its pre-reionization peak. Star formation in R10-kinf-0.3 behaves very differently; once the star formation rate rises to a value of approximately 3×10^{-4} $M_{\odot}yr^{-1}$ it plateaus and remains constant until reionization. Post-reionization the star formation rate drops to zero.

The effect of different supernova feedback models manifests itself on larger scales as well. Figures 4.3 and 4.4 show the environment around the population of star forming progenitor halos just prior to the onset of reionization at $z = 7.04$. The global star formation rate in R10-kinf-0.3 is over an order of magnitude lower than it is in R10-kinf-0, but despite this, the supernova driven winds driven in R10-kinf-0.3 create large-scale rarified bubbles of metal-enriched, 10^5 K gas unlike the weaker winds driven in R10-kinf-0.

The weaker winds in R10-kinf-0 have consequences for the enrichment of the stellar component since metals are less effectively driven out of halos, a problem that was seen

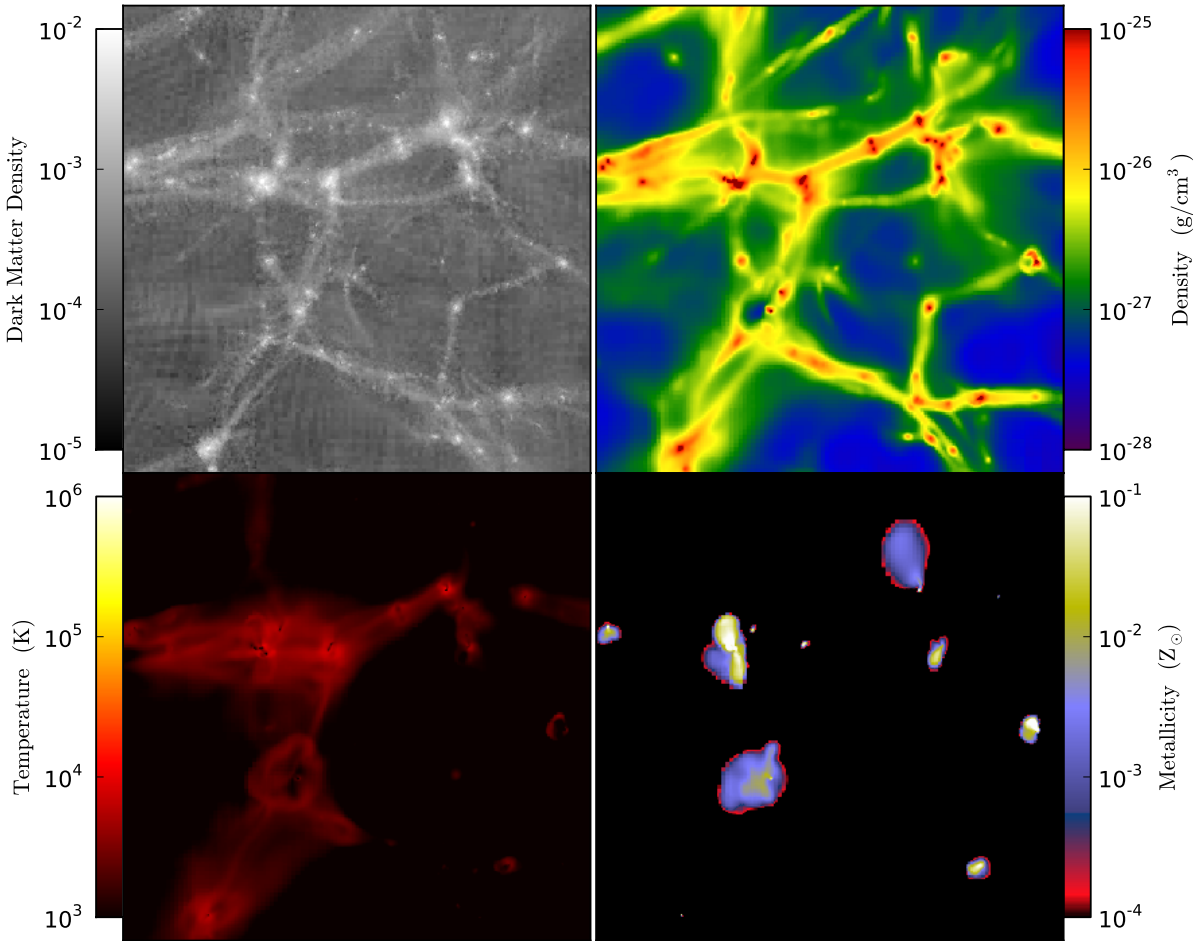

Figure 4.3 Projections of dark matter density (top left), gas density (top right), gas temperature (bottom left) and gas metallicity (bottom right) at redshift 7.04 in simulation R10-kinf-0. The volume projected is 300 comoving kpc, which is 37 kpc at this redshift. This volume encloses all the star forming progenitor halos of the final target halo. All the projections except for the dark matter density projection are weighted by gas density. The dark matter density projection is unweighted.

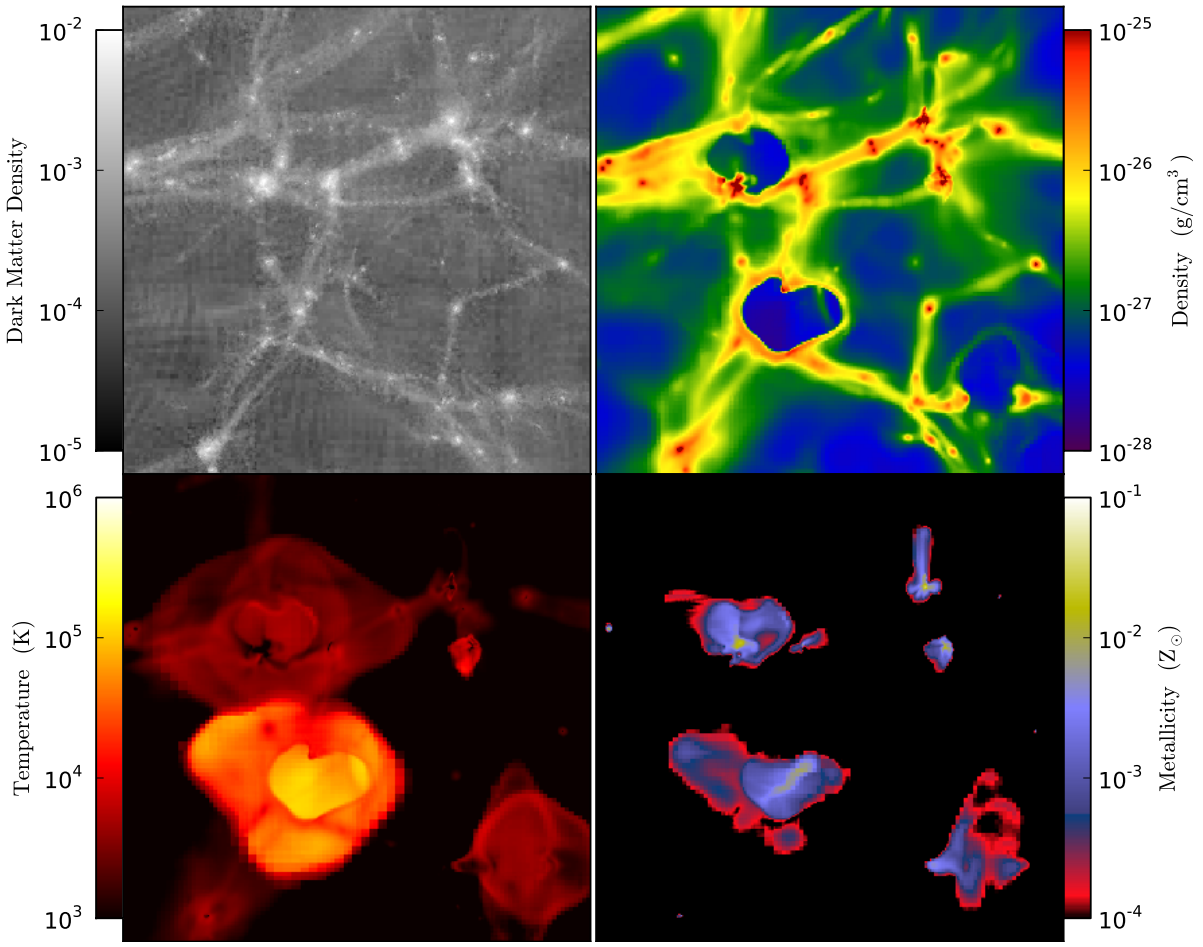

Figure 4.4 Projections of simulation R10-kinf-0.3 at redshift $z = 7.04$. The quantities projected are the same as in Figure 4.3.

in R10. However, unlike in R10, the feedback produced in R10-kinf-0 has a weaker effect on post-reionization self-shielded gas. Clumps of self shielded gas survive in R10-kinf-0 down to low redshift and continue to form stars as demonstrated by the star formation rate shown in Figure 4.2.

4.2.2 Stellar metal enrichment

As we have seen, qualitative differences in the winds produced by star-forming progenitors in R10-kinf-0 and R10-kinf-0.3 indicate that metals are more effectively ejected from halos when kinetic energy injection is used. The mean metallicity of star particles formed in R10-kinf-0.3 is Log($\langle Z/Z_{\odot} \rangle$) = -1.58 and Log($\langle Z/Z_{\odot} \rangle$) = 0.29 in R10-kinf-0. It should be noted, however, that in the case of R10-kinf-0 limits placed on gas metallicity in the calculation to prevent errors in the calculation of the cooling rate in low density gas appear to have been triggered in high density regions, as evidenced by the presence of dense cells at the threshold metallicity as shown in Figure 4.1 and shown by the presence of star particles at this threshold value as shown in Figure 4.5. The limit placed on gas metallicity in R10-kinf-0 does not affect our conclusions concerning the stellar metal enrichment in this simulation because the metallicity threshold far exceeds physically reasonable values for stellar metallicity in a system of this mass and luminosity by many dex.

Figure 4.5 shows the distribution of stellar metallicity of newly formed stars as a function of redshift in R10, R10-kinf-0 and R10-kinf-0.3. The distribution of stellar metallicities reveals differences in how the different models employed release metals, expel them from star forming regions and regulate the density of star-forming gas.

All three models form a small number of star particles at the initialization metallicity

of gas in our model which is 5×10^{-9} $Z_{\odot}$. These star particles represent a Pop III stellar population, although in our model we do not have a distinct mode of Pop III star formation and feedback that differs from our generic model . These essentially metal free stars are formed until $z = 7$ when the reionizing field is introduced. Once the simulation volume is ionized, the cooling and collapse of gas in pristine halos of low mass is no longer possible since they are largely photoevaporated and their virial temperatures are now below that of the IGM.

Low metallicity star particles, i.e. star particles with R10-kinf-0metallicities between approximately log(Z/$Z_{\odot}$) = -8 and -3, are formed in varying number in each of the three models. They are most numerous in R10 where metals are released gradually along with thermal energy. In this model, there is a continuous population of star particles between the 'metal free' stars at log(Z/$Z_{\odot}$) = -8.3 and the metal rich bulk of the stellar population.

In R10-kinf-0 and R10-kinf-0.3, all the metals produced by a star particle are injected in a single time step along with the feedback energy. In pristine gas, the metallicity of enriched gas in the feedback zone surrounding a star particle is determined by the values we have chosen for the supernova metal yield, the mass loading factor and the typical density of the ISM in which supernova feedback occurs. The metal fraction of gas in the feedback zone immediately after feedback will be

$$f_Z = \frac{yM_*}{f_{load}M_* + 27\rho(\frac{\Delta x}{z+1})^3}, \tag{4.1}$$

where y is the metal yield of a star particle, which we have set to 2%; f_{load} is the fraction of mass star particles return to the ISM, which we have set to 25%; and ρ is the background

density of the medium. In gas at the density threshold for star formation, we expect this metallicity to be $\log(Z/Z_\odot)$ = -2.8 on the coarsest grids that contains gas at this density. As pristine gas collapses into halos for the first time, we would expect the first star particles to be formed on these grids. Grids at this level have a comoving cell width of 86.4 pc; therefore, at redshifts greater than six, when the star formation rate peaks, these grids have physical cell widths less than 12.3 pc.

Low metallicity star particles form close to this value in R10-kinf-0 and R10-kinf-0.3. Mixing of this singly enriched gas should form an ISM with a metallicity below this value from which the next star in the halo will form, and indeed there is a population of star particles with metallicities up to a dex below this value. A handful of star particles exist between the zero metallicity population and the second generation population which may be due to halo cross pollution or low-metallicity pockets that mixing has not significantly enriched.

Eventually metals will begin to build up in halos and a metal rich population forms. Since there are multiple star forming halos that all cool gas on different timescales, star particles between the mean metallicity and the pristine gas pollution limit do not follow a monotonic trend with redshift. In R10, the stellar metallicities plateau around 1 $Z_\odot$, but star formation is truncated soon after reionization, so continued star formation would likely produce further enriched star particles. In R10-kinf-0, stellar metallicities plateau at the gas metallicity limit of 10 $Z_\odot$after reionization.

The metal enrichment of the stellar component in R10-kinf-0.3 is very different from the other two models. In this simulation, the stellar metallicities plateau around $\log(Z/Z_\odot)$ = -1.5 and maintain this maximum from z = 9 until the truncation of star formation at

$z = 4$. This self regulation of stellar metallicity is unlike the evolution of enrichment seen in the models with purely thermal supernova feedback, R10 and R10-kinf-0.

4.3 Discussion

The application of our kinetic feedback model to a galactic context reveals broadly the ways in which kinetic energy injection can affect dense gas and star formation. It also provides insights into effects not included in Chapter 3 such as a non-homogeneous medium and low-temperature radiative cooling. The connection between these galaxy models and the test simulations presented in Chapter 3 demonstrate ways in which modeling in each regime can be improved. In this section, we will discuss several aspects of our galaxy models that highlight the effects of differing feedback models such as the star formation rate and production of galactic winds. Also, an examination of the stellar metallicity distribution and how it compares to observations can provide insights into aspects of stellar feedback not included in our model and ways to extend this work in the future.

4.3.1 Star Formation Rate

We have demonstrated that the kinetic injection fraction chosen for the feedback model can have a dramatic impact on the star formation rate of our simulated halo. Given the results of Chapter 3, this is an unsurprising result. At the resolution of these simulations, and for the densities in which supernova feedback occurs in our model, we would expect the resolution timescale of supernova affected regions to be comparable to or to exceed the snow-plow timescale. This means that radiative cooling dominates the energetic evolution

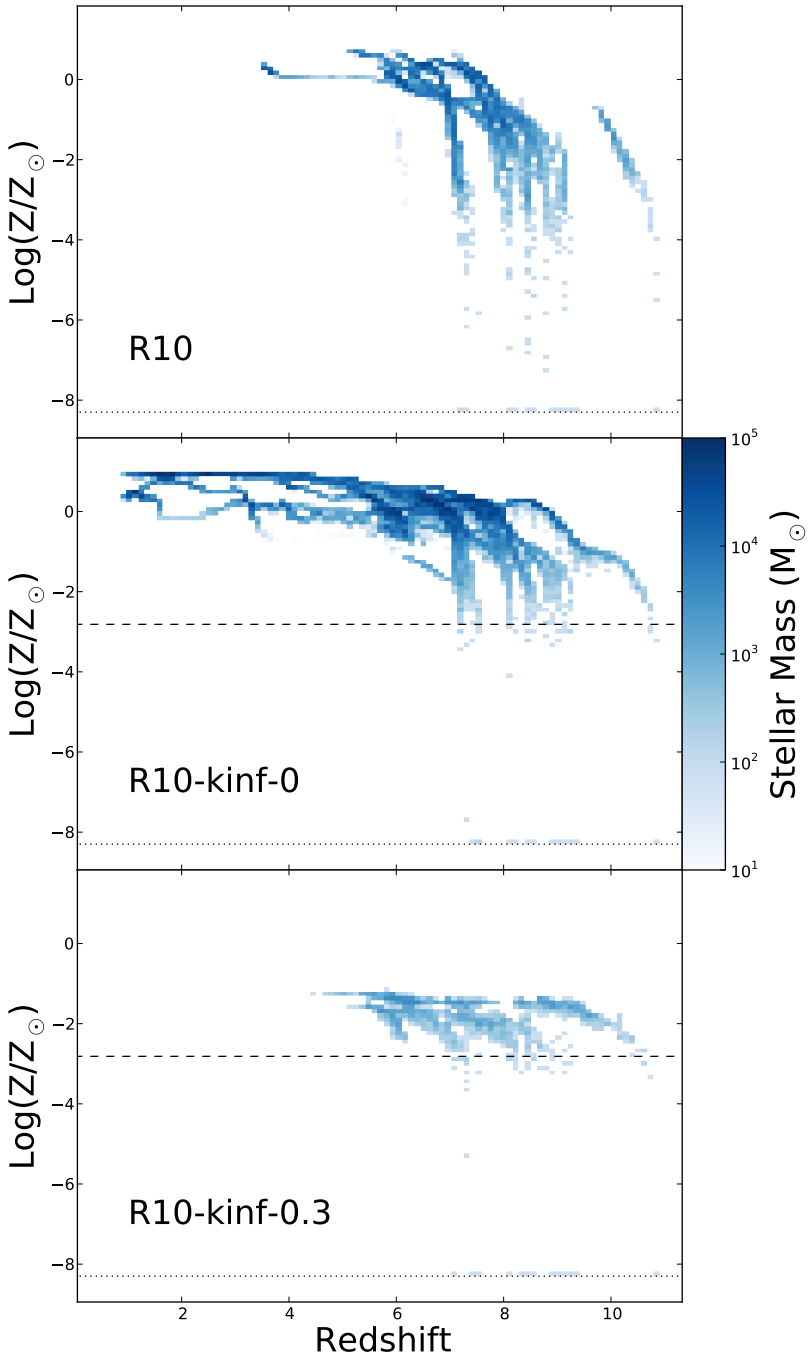

Figure 4.5 Metallicity and redshift distribution of stellar mass formed in R10, R10-kinf-0 and R10-kinf-0.3. The dotted lines at $\log(Z/Z_{\odot})$ = -8.3 indicate the initialization metallicity for gas in our simulations. The dashed lines at $\log(Z/Z_{\odot})$ = -2.8 indicate the metallicity of pristine gas enriched by a single star particle with the kinetic feedback model employed in R10-kinf-0 and R10-kinf-0.3. This value is computed from Equation 4.1 assuming gas at the density threshold for star formation on the most coarsely refined grid that resolves this density.

before the kinetic and thermal energies have a chance to equilibrate. This likely leads to a difference in the level of energy retained in supernova heated gas between R10-kinf-0 and R10-kinf-0.3. The result is a more diffuse ISM in R10-kinf-0.3 that has a lower star formation rate.

A direct comparison between the idealized test models presented in Chapter 3 and the galaxy simulations presented here is complicated by the different cooling prescriptions used in each. The galaxy simulations presented here have radiative cooling at temperatures below 10^4 K, unlike our idealized test models. The test models therefore cannot be used to estimate in absolute terms the size of the energy difference expected between the high resolution converged models and low resolution models run with different kinetic energy injection fractions that are expected to retain different amounts of supernova energy in the ISM. However, the test models are informative in understanding at what resolutions we expect energy dissipation to diverge between models with different initial kinetic fractions. In our model, star particles form on grids with a physical resolutions less than 12.3 pc (i.e. on AMR levels greater than 9 and at redshifts greater than 6). Star particles explode in the dense media from which they form (i.e. $\rho_{gas} \sim 100$ cm^{-3}). Therefore, the 8 and 4 pc resolution panels in Figure 3.8 offer the closest approximation to the feedback behavior in our galaxy simulations. At these resolutions, we do see significant differences in the amount of supernova energy retained in the gas.

As we have discussed, the density of the supernova affected region is crucial in energetic evolution of the surrounding ISM. In our simulations, we may well be injecting energy into an unphysically dense medium, since we inject supernova energy into the surrounding gas immediately after a star particle's creation. The density of this gas is

high (> 10 - 100 cm^{-3}) and is set by the star formation algorithm used. Observations of supernova remnants in the Milky Way indicate that supernovae may occur in ISM with much lower densities (~ 1 cm^{-3}). Type II supernovae are products of massive stars which produce large amounts of UV radiation and stellar winds prior to the supernova event. The amount of energy produced in this phase is comparable to the amount of energy produced during the supernova (Agertz et al. 2013) and in many cases, likely produces a rarified HII region surrounding the star. We have not attempted to simulate this phase of stellar feedback and it may well be important in regulating the density of the ISM around supernova events. On the other hand, the mass of material shed by a massive star during a red supergiant phase may raise the density of the surrounding ISM resulting in a higher background density (van Veelen et al. 2009). It is also interesting to note that the densities surrounding supernova remnants in the massive star forming region of the LMC 30 Doradus exceed the commonly found value in the Milky Way of 1 cm^{-3} (Smith & Wang 2004).

A lower background density for supernova events would reduce the importance of f_{kin} in our model because the snow-plow timescale exceeds the resolution timescale at the resolution of our galaxy model. In addition, our resolution in feedback zones is not constrained to occur at the maximum allowed resolution in the simulation. Rather, it is determined by the local gas and dark matter density. In R10-kinf-0.3, the cell width does not drop below 43 comoving pc, which at $z = 8$ corresponds to a cell width of more than 4 pc. Based on Figure 3.8, if feedback at this redshift was constrained to occur on the finest level of allowed refinement, which has a factor of 4 better resolution, we may expect different behavior of supernova heated gas that is also less sensitive to the choice

of f_{kin}. Most of the star formation and feedback in R10-kinf-0 does occur on grids at the maximum allowed resolution. The reason for this difference, however, is that gas reaches much higher densities in R10-kinf-0 and therefore the resolution needed to reach a state where f_{kin} does not matter is higher.

4.3.2 Galactic winds

As we have seen, the effect of galactic winds on the circumgalactic medium in R10-kinf-0 and R10-kinf-0.3 are dramatically different. The winds in R10-kinf-0.3 are much more effective in heating and enriching the circumgalactic medium.

Figure 4.6 shows the phase space distribution of gas within a single star forming halo in R10, R10-kinf-0 and R10-kinf-0.3. In the simulations employing purely thermal feedback, we see that cells are heated to temperatures up to 10^6 K and in the case of R10, up to 10^7 K. In R10, which produces stronger winds, we see gas following a constant pressure trend, indicating that this gas is in an expanding, pressure supported bubble. There is a metallicity gradient along this trend, with the hottest, lowest density gas being the most metal rich.

In contrast, gas in the example halo from R10-kinf-0.3 shows a very different phase space distribution. There are cells at the highest density heated to temperatures up to 10^5, but there is no gas at 10^6 - 10^7 K, or evidence of pressure supported bubbles. It appears that rather than a high temperature and high thermal pressure region driving an expanding outflow due to a thermal pressure imbalance, momentum directly injected by star particles is responsible for driving winds.

The warm gas seen on large scales in the thermal and kinetic feedback runs therefore

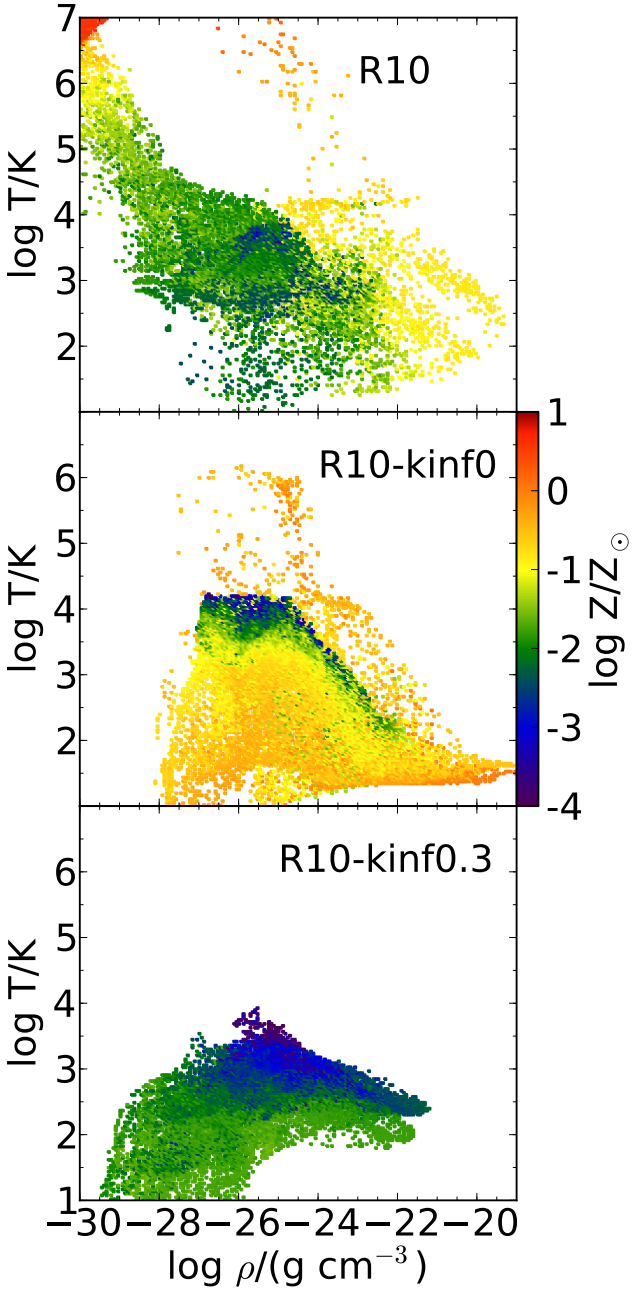

Figure 4.6 Density-temperature phase space of gas within r_{200} for a star forming halo in R10, R10-kinf-0 and R10-kinf-0.3. The color of cells distributed over this phase space is the density weighted average gas metallicity at each phase space position.

have different origins. The heating of the IGM seen in R10-kinf-0.3 is due to shock heating from momentum driven winds interacting with the low density IGM. The heating seen in the thermal feedback runs is some combination of weaker shock heating and residual thermal energy from thermal pressure bubbles that has yet to cool.

4.3.3 Stellar metallicity distributions

As discussed in Section 4.2.2, the distribution of stellar metallicity differs greatly between R10, R10-kinf-0 and R10-kinf-0.3 and these differences are a direct consequence of the feedback model used in each simulation. When compared to the metallicity distributions observed for dSphs in the Milky Way (Figure 4.7), it is clear that the distributions found in R10 and R10-kinf-0 are inconsistent with observed systems due to their high means, which are close to solar, while the distribution found in R10-kinf-0.3 is much closer to those found in observed systems.

The metallicity distribution in R10-kinf-0.3 has a much lower mean metallicity that is quite narrow. The shape of its metallicity distribution is most consistent with the metallicity distribution of Leo II, however, Leo II is an order of magnitude more luminous than the final halo in R10-kinf-0.3. The simulated metallicity distribution in R10-kinf-0.3 is also much more sharply peaked than any of the observed systems, including Leo II.

The differences seen between the metallicity distributions of observed systems and the metallicity distribution of R10-kinf-0.3 may have any one of a number of causes. As we have discussed, the stellar feedback model used in R10-kinf-0.3 closely regulates the density of gas in progenitor halos, keeping it fixed at the density threshold for star formation. In addition, the metallicity of dense gas remains constant once it has enriched

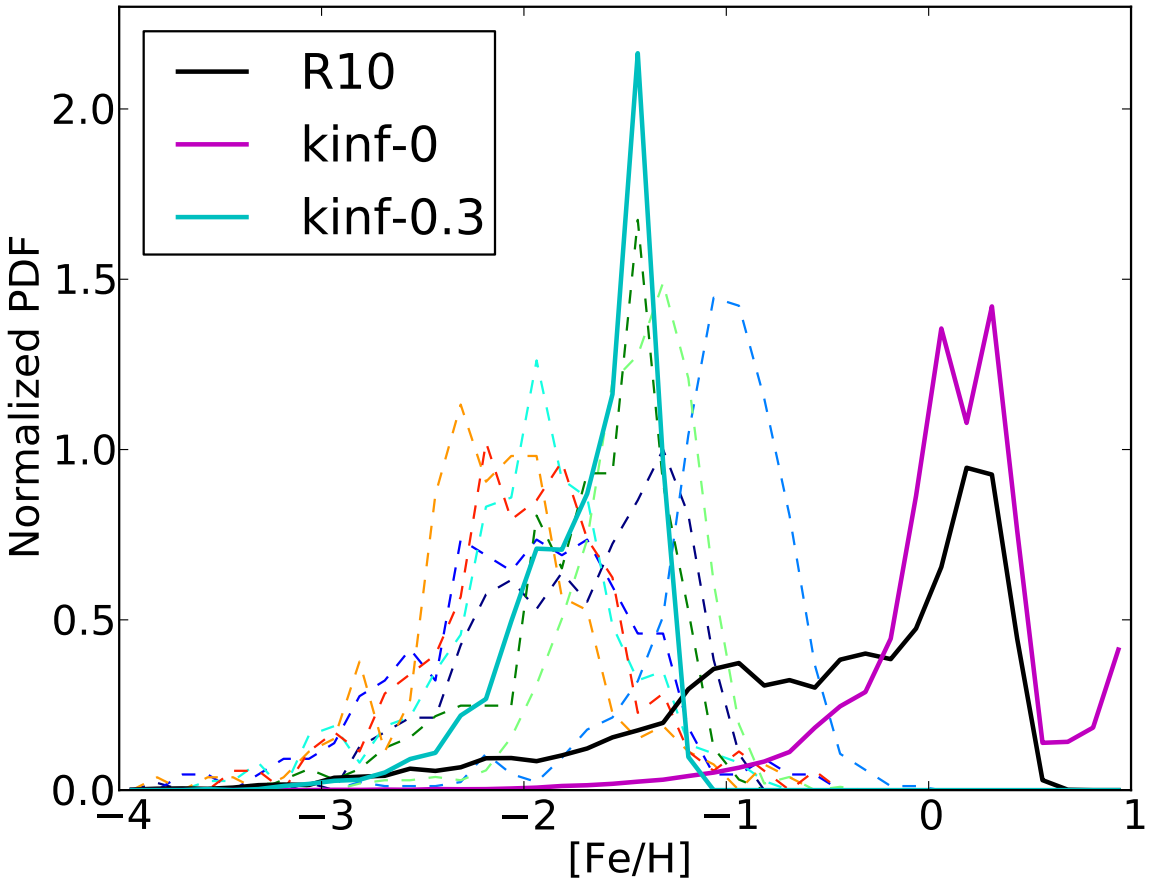

Figure 4.7 Normalized distributions of stellar metallicity for observed dSphs of the Milky Way (Kirby et al. 2011a, dashed lines) and for our simulated halos in R10, R10-kinf-0 and R10-kinf-0.3. The simulated distributions include all star particles that end the simulation within r_{200} of the halo center. The distribution plotted for R10-kinf-0 is for the simulated halo at redshift 0.92.

to an equilibrium level. This results in a roughly constant star formation rate at a roughly constant stellar metallically and as a consequence, a large population of star particles is created at the equilibrium gas metallicity.

A truncation of the star formation history would certainly reduce the population of star particles formed at the metallicity peak since the lower metallicity star particles tend to form earlier, however, the star formation history in this model is already quite truncated relative to Milky Way dSphs. Also, the dSphs with high metallicity peaks tend to be more luminous, which would argue for a more extended star formation history.

Another cause for the strong peak in stellar metallicity in R10-kinf-0.3 may be that the feedback model used is a single, prompt injection of energy and metals, mimicking Type II supernovae, rather than a more comprehensive model that includes multiple sources of feedback occurring on different timescales and with different energies. It is possible that this single source of stellar feedback naturally results in a strong, high metallicity peak. The broadest metallicity distribution found in any of the simulations presented is created in R10, in which there is a gradual injection of metals and energy by star particles. This model creates a large population of low metallicity star particles. While this model is unphysical in many ways, it demonstrates that some ejection of metals through stellar winds in the pre-supernova stage may play a role in producing the broad distribution of stellar metallicites, especially at the low metallicity end.

It is quite interesting to note that a number of observed dSphs have significant high metallicity tails to their distributions. In R10-kinf-0.3 this type of feature is precluded by the way in which feedback regulates gas density and drives out metals. It is possible that some type of delayed feedback, like Type Ia supernovae, could be key in producing

this effect. In addition, the metallicities in our simulations represent a mean over several chemical species, not just an iron abundance, which is the quantity the observational data measure. Iron is produced primarily in Type Ia supernovae, so it is possible that stars formed in post-Type II supernova ejecta will be poorer in iron and richer in other elements.

It is also possible that the metallicity distribution is influenced by the halo merger history or environment. Since our single halo realization probes only a single merger history and a single environment, we cannot comment on these effects. For example, progenitor halos that grow more rapidly early on may undergo an imbalance in the self-regulatory star-forming state achieved in the progenitors of this halo realization because of their deeper gravitational potential wells at early times when the star formation rate peaks.

4.4 Summary of kinetic feedback in galaxy simulations

In this chapter, we have presented cosmological dwarf galaxy simulations that include kinetic energy in supernova feedback as well as the quick injection of supernova energy. We found that the quick injection of purely thermal energy does not make feedback more effective; in fact, the quick injection appears to make it less effective than the model that slowly releases supernova energy used in Chapter 2. This may be due to the effect that early heating in the slow injection model has in priming the background medium for the later injection of the rest of the supernova energy. The initial release of a small amount of energy may decrease the background density of the affected medium enough for the subsequent release of the rest of the supernova energy to have a greater effect.

The greatest effect of the new model, however, is seen in the simulation R10-kinf-0.3 that injects 30% of supernova energy in kinetic form. In this model, the maximum density of gas is suppressed such that star formation rate becomes roughly constant and the ejection of metals from star forming gas is greatly enhanced. There is greater shock heating of the IGM in this model as well, producing large bubbles of rarified gas at temperatures in excess of 10^5 K prior to reionization. The metallicity of the stellar population saturates at value of approximately $\mathrm{Log}(Z/Z_\odot)$ = -1.5. The average metallicity of the resulting stellar population is roughly consistent with observed systems, however, the shape of the metallicity distribution appears to be too narrow, indicating effects we have not included in this model, possibly other sources of stellar feedback.

The proper calibration of this kinetic feedback model is left as an open question. We chose a value of f_{kin} = 0.3 based on the analytic Sedov-Taylor calculation for the adiabatic evolution of supernova remnant energetics and this test, combined with the analysis presented in Chapter 3, has demonstrated the need for kinetic energy inclusion at these resolutions. Further testing like that done in Chapter 3 with a cooling curve that includes radiative cooling of gas at temperatures below 10^4 K is needed to provide a proper calibration of the method. However, it should be noted that in models with high enough resolution (less than one pc), this effect is likely not needed.

Chapter 5

Conclusions

This study has attempted to probe the dominant physical mechanisms at play in the formation of low mass dwarf galaxies. We have explored the role of supernova feedback by testing two different feedback models in order to better understand the relative impacts of momentum injection and prompt energy injection on the star formation rates and metallicities of star particles. We conducted a detailed set of idealized reference models for the two supernova feedback models used in our galaxy simulations. These test models provide a framework in which to understand the behavior of supernova feedback in our galaxy simulations.

5.1 The physics of dwarf galaxy formation

The simulations presented in Chapters 2 and 4 are the highest resolution cosmological simulations to date of a 10^9 $M_\odot$ dwarf halo run down to a redshift of zero. The maximum resolution of these simulations is 11 comoving pc, which means that these simulations

achieve physical resolutions of a few parsecs during the epoch of greatest star formation in progenitor halos, between redshifts of 6 and 10. Our canonical simulations include metal cooling, molecular hydrogen formation and cooling, photoionization and photodissociation from a metagalactic background (with a simple prescription for self-shielding) and star formation. We test two different models for supernova driven energetic feedback.

We find that reionization is primarily responsible for setting the total gas fraction of our halos. This occurs through photo-evaporative winds, which expel most of the gas envelope in our simulated systems (although not the central, dense core). Once the gas is ejected, our halo is unable to efficiently re-accrete new baryons, and so the gas fraction remains suppressed to $z = 0$. The timing of reionization has a major impact on the final stellar mass of our halo, by interrupting the cooling of gas onto lower mass progenitor halos. Depending on the patchiness of reionization, an early or delayed epoch of ionization may result in an order of magnitude change to the resulting stellar mass.

Our final halo, which has a mass of 10^9 $M_\odot$ at $z = 0$, forms hierarchically from several progenitor halos, many of which are star-forming. The stellar population in the final halo was therefore built up from star formation episodes in these separate halos.

The dense gas, from which star particles form, appears to be mostly regulated by feedback from star formation, although UV heating contributes. Once gas in a halo photoevaporates, the remaining dense, self-shield clumps of gas are destroyed by supernova feedback. While reionization is the main mechanism responsible for expelling gas from progenitor halos, supernova feedback is mostly responsible for expelling metals.

H_2 line cooling is a crucial and necessary ingredient to start star formation in these low mass halos. Atomic line cooling in the absence of metals is insufficient by itself to cool

gas to the densities required for star formation in such shallow potential wells. Without a first generation of star formation to pollute the ISM with metals, there is no coolant sufficiently effective to cool gas at subsequent epochs.

5.2 Supernova feedback modeling

The two supernova feedback models we have tested influence both the star formation rate and the stellar metallicities of the our simulated dwarf galaxy. The injection of momentum appears to have a substantial effect and produces a simulated galaxy with the most fidelity to observed systems. At the high cell resolution of our models, it appears that the weak feedback created in purely thermal schemes may be caused by the missing ingredient of kinetic energy, rather than by unphysical overcooling.

The metallicities of star particles formed in simulations that inject purely thermal supernova energy are too metal rich by a dex or more. This is in contrast to the model that includes some momentum injection. This model forms star particles with metallicities that are comparable to stellar metallicities in observed dSphs. The mean metallicity of the final system is slightly elevated for its luminosity, but this may be due to the details of how we convert our simulated single metallicity to the observable quantity [Fe/H]. It is true, however, that the shape of the metallicity distribution is much too narrowly peaked at high metallicity. This discrepancy may indicate that there is still missing physics in our model that can be pursued in future work.

Understanding the effect of the kinetic injection fraction in the context of a galaxy simulation is a challenging problem due to the complex radiative gas cooling prescriptions

typically employed in such simulations. The inclusion of kinetic energy clearly has a strong effect on galactic winds that in turn regulate (or fail to regulate, as the case may be) the galaxy star formation rate and the amount of metal ejection. Our idealized test simulations presented in Chapter 3 demonstrate how kinetic feedback in dense material results in the higher retention of energy in supernova affected gas, but cannot provide a calibration in absolute physical terms due to the limitations of the cooling employed.

It is also important to note that supernova feedback in our models may well be occurring in gas that is too dense. As Chapter 3 demonstrated, in lower density gas the effect of the choice of the kinetic injection fraction is diminished. Because our simulations do not include (by design) any type of pre-supernova stellar feedback, the galaxy models presented in Chapter 4 with the new feedback model may be unrealistically dependent on the choice of kinetic injection fraction.

5.3 Future Work

There is much future work that can be done to extend the results and methods presented in this study. More testing of the kinetic feedback method that we have devised is necessary to fully understand its effects in our galaxy models. Tests that include more complex radiative cooling would be very informative. Additional galaxy simulations conducted with different kinetic injections fractions would also provide an interesting gauge for evaluating the impact of this model in a more realistic ISM.

Many improvements to the galactic application of the kinetic feedback model are still needed. Code developments that will be included in Enzo 3.0 will make communication

between grids possible and negate the need for the artificial shifting of feedback zones near grid edges. Restrictions are also needed on the time steps computed for supernova hosting grids. It may also be desirable to force refinement of supernova hosting grids down to the maximum allowed level of AMR.

An expansion of the feedback model to a wider array of stellar feedback mechanisms would also be interesting. The inclusion of the effects of stellar winds and ionizing radiation may have a significant impact on our models. Including distinct modes of Pop II and Pop III star formation would also be quite interesting given the quick enrichment seen in simulations run with our kinetic feedback model. The inclusion of more chemical species would also provide an additional diagnostic to distinguish between models.

Over the long term, we would like to apply these modeling techniques to a larger sample of dark matter halos with different masses, located in different environments and with different merger histories. The type of detailed analysis we have presented in this study of a single halo provides valuable physical intuition into the processes involved in galaxy formation, but if we want to make significant progress in comparing to observed systems, we need to simulate a more cosmologically diverse and complete sample of halos.

Bibliography

Abel, T., Anninos, P., Zhang, Y., & Norman, M. L. 1997, New A, 2, 181

Abel, T., Bryan, G. L., & Norman, M. L. 2002, Science, 295, 93

Adén, D., Feltzing, S., Koch, A., et al. 2009, A&A, 506, 1147

Agertz, O., Kravtsov, A. V., Leitner, S. N., & Gnedin, N. Y. 2013, ApJ, 770, 25

Agertz, O., Moore, B., Stadel, J., et al. 2007, MNRAS, 380, 963

Alvarez, M. A., Bromm, V., & Shapiro, P. R. 2006, ApJ, 639, 621

Anninos, P., Zhang, Y., Abel, T., & Norman, M. L. 1997, New A, 2, 209

Badenes, C. 2010, Proceedings of the National Academy of Science, 107, 7141

Barkana, R., & Loeb, A. 1999, ApJ, 523, 54

Belokurov, V., Walker, M. G., Evans, N. W., et al. 2008, ApJ, 686, L83

—. 2009, MNRAS, 397, 1748

Booth, C. M., Schaye, J., Delgado, J. D., & Dalla Vecchia, C. 2012, MNRAS, 420, 1053

Boylan-Kolchin, M., Bullock, J. S., & Kaplinghat, M. 2012, MNRAS, 422, 1203

Brown, R. L. 1971, ApJ, 164, 387

Brown, T. M., Tumlinson, J., Geha, M., et al. 2012, ApJ, 753, L21

Bryan, G. L. 1999, Comput. Sci. Eng., Vol. 1, No. 2, p. 46 - 53, 1, 46

Bryan, G. L., Norman, M. L., Stone, J. M., Cen, R., & Ostriker, J. P. 1995, Computer Physics Communications, 89, 149

Bullock, J. S., Kravtsov, A. V., & Weinberg, D. H. 2000, ApJ, 539, 517

Cen, R., & Bryan, G. L. 2001, ApJ, 546, L81

Cen, R., & Ostriker, J. P. 1992, ApJ, 399, L113

Chapman, S. C., Ibata, R., Lewis, G. F., et al. 2005, ApJ, 632, L87

Chevalier, R. A. 1974, ApJ, 188, 501

Colella, P., & Woodward, P. R. 1984, Journal of Computational Physics, 54, 174

Conroy, C., & Gunn, J. E. 2010, ApJ, 712, 833

Côté, P., Mateo, M., Olszewski, E. W., & Cook, K. H. 1999, ApJ, 526, 147

Cox, D. P. 1972, ApJ, 178, 159

de Avillez, M. A. 2000, MNRAS, 315, 479

de Avillez, M. A., & Mac Low, M.-M. 2002, ApJ, 581, 1047

Draine, B. T. 2011, Physics of the Interstellar and Intergalactic Medium

Draine, B. T., & Bertoldi, F. 1996, ApJ, 468, 269

Eisenstein, D. J., & Hut, P. 1998, ApJ, 498, 137

Ferland, G. J., Korista, K. T., Verner, D. A., et al. 1998, PASP, 110, 761

Finlator, K., & Davé, R. 2008, MNRAS, 385, 2181

Fragile, P. C., Murray, S. D., Anninos, P., & Lin, D. N. C. 2003, ApJ, 590, 778

Fraternali, F., Tolstoy, E., Irwin, M. J., & Cole, A. A. 2009, A&A, 499, 121

Geha, M., Blanton, M. R., Yan, R., & Tinker, J. L. 2012, ApJ, 757, 85

Geha, M., Willman, B., Simon, J. D., et al. 2009, ApJ, 692, 1464

Glover, S. C. O. 2003, ApJ, 584, 331

Glover, S. C. O., & Clark, P. C. 2012a, MNRAS, 421, 9

—. 2012b, MNRAS, 426, 377

Gnedin, N. Y. 2000, ApJ, 542, 535

—. 2010, ApJ, 721, L79

Gnedin, N. Y., & Kravtsov, A. V. 2006, ApJ, 645, 1054

Gnedin, O. Y., & Zhao, H. 2002, MNRAS, 333, 299

Governato, F., Brook, C., Mayer, L., et al. 2010, Nature, 463, 203

Governato, F., Zolotov, A., Pontzen, A., et al. 2012, MNRAS, 422, 1231

Grcevich, J., & Putman, M. E. 2009, ApJ, 696, 385

Guedes, J., Callegari, S., Madau, P., & Mayer, L. 2011, ApJ, 742, 76

Haardt, F., & Madau, P. 2001, in Clusters of Galaxies and the High Redshift Universe Observed in X-rays, ed. D. M. Neumann & J. T. V. Tran

Haardt, F., & Madau, P. 2011, ArXiv e-prints

Hinshaw, G., Weiland, J. L., Hill, R. S., et al. 2009, ApJS, 180, 225

Hockney, R. W., & Eastwood, J. W. 1988, Computer simulation using particles

Hopkins, P. F., Quataert, E., & Murray, N. 2011, MNRAS, 417, 950

Hummels, C. B., & Bryan, G. L. 2012, ApJ, 749, 140

Ibata, R., Martin, N. F., Irwin, M., et al. 2007, ApJ, 671, 1591

Irwin, M., & Hatzidimitriou, D. 1995, MNRAS, 277, 1354

Irwin, M. J., Belokurov, V., Evans, N. W., et al. 2007, ApJ, 656, L13

Joung, M. K. R., & Mac Low, M.-M. 2006, ApJ, 653, 1266

Jungwiert, B., Combes, F., & Palouš, J. 2001, A&A, 376, 85

Katz, N., Hernquist, L., & Weinberg, D. H. 1992, ApJ, 399, L109

Kennicutt, Jr., R. C. 1998, ApJ, 498, 541

Kirby, E. N., Cohen, J. G., & Bellazzini, M. 2012, ApJ, 751, 46

Kirby, E. N., Lanfranchi, G. A., Simon, J. D., Cohen, J. G., & Guhathakurta, P. 2011a, ApJ, 727, 78

Kirby, E. N., Martin, C. L., & Finlator, K. 2011b, ApJ, 742, L25

Kirby, E. N., Simon, J. D., Geha, M., Guhathakurta, P., & Frebel, A. 2008, ApJ, 685, L43

Klypin, A., Kravtsov, A. V., Valenzuela, O., & Prada, F. 1999, ApJ, 522, 82

Koch, A., Kleyna, J. T., Wilkinson, M. I., et al. 2007, AJ, 134, 566

Koch, A., Wilkinson, M. I., Kleyna, J. T., et al. 2009, ApJ, 690, 453

Koposov, S., Belokurov, V., Evans, N. W., et al. 2008, ApJ, 686, 279

Koposov, S. E., Gilmore, G., Walker, M. G., et al. 2011, ApJ, 736, 146

Kormendy, J., Fisher, D. B., Cornell, M. E., & Bender, R. 2009, ApJS, 182, 216

Kroupa, P. 2007, ArXiv Astrophysics e-prints

Kruijssen, J. M. D., & Mieske, S. 2009, A&A, 500, 785

Krumholz, M. R., & Tan, J. C. 2007, ApJ, 654, 304

Kuhlen, M., Krumholz, M. R., Madau, P., Smith, B. D., & Wise, J. 2012, ApJ, 749, 36

Letarte, B., Chapman, S. C., Collins, M., et al. 2009, MNRAS, 400, 1472

Lewis, G. F., Ibata, R. A., Chapman, S. C., et al. 2007, MNRAS, 375, 1364

Li, Y., & Bryan, G. L. 2012, ApJ, 747, 26

Mac Low, M.-M., & Ferrara, A. 1999, ApJ, 513, 142

Machacek, M. E., Bryan, G. L., & Abel, T. 2001, ApJ, 548, 509

Madau, P., Ferguson, H. C., Dickinson, M. E., et al. 1996, MNRAS, 283, 1388

Majewski, S. R., Skrutskie, M. F., Weinberg, M. D., & Ostheimer, J. C. 2003, ApJ, 599, 1082

Makarov, D., Makarova, L., Sharina, M., et al. 2012, MNRAS, 425, 709

Martin, N. F., de Jong, J. T. A., & Rix, H.-W. 2008, ApJ, 684, 1075

Martin, N. F., Ibata, R. A., Chapman, S. C., Irwin, M., & Lewis, G. F. 2007, MNRAS, 380, 281

Mateo, M., Olszewski, E. W., & Walker, M. G. 2008, ApJ, 675, 201

Mateo, M. L. 1998, ARA&A, 36, 435

McConnachie, A. W., & Irwin, M. J. 2006, MNRAS, 365, 1263

McGaugh, S. S., Schombert, J. M., de Blok, W. J. G., & Zagursky, M. J. 2010, ApJ, 708, L14

Monelli, M., Gallart, C., Hidalgo, S. L., et al. 2010, ApJ, 722, 1864

Moore, B., Ghigna, S., Governato, F., et al. 1999, ApJ, 524, L19

Navarro, J. F., Eke, V. R., & Frenk, C. S. 1996, MNRAS, 283, L72

Navarro, J. F., Frenk, C. S., & White, S. D. M. 1997, ApJ, 490, 493

Navarro, J. F., Ludlow, A., Springel, V., et al. 2010, MNRAS, 402, 21

Norman, M. L., & Bryan, G. L. 1999, in Astrophysics and Space Science Library, Vol. 240, Numerical Astrophysics, ed. S. M. Miyama, K. Tomisaka, & T. Hanawa, 19

Okamoto, S., Arimoto, N., Yamada, Y., & Onodera, M. 2012, ApJ, 744, 96

Okamoto, T., Frenk, C. S., Jenkins, A., & Theuns, T. 2010, MNRAS, 406, 208

Oppenheimer, B. D., & Davé, R. 2008, MNRAS, 387, 577

O'Shea, B. W., Bryan, G., Bordner, J., et al. 2004, ArXiv Astrophysics e-prints

Osterbrock, D. E., & Ferland, G. J. 2006, Astrophysics of gaseous nebulae and active galactic nuclei

Pontzen, A., & Governato, F. 2012, MNRAS, 421, 3464

Revaz, Y., & Jablonka, P. 2012, A&A, 538, A82

Ricotti, M., & Gnedin, N. Y. 2005, ApJ, 629, 259

Ryan-Weber, E. V., Begum, A., Oosterloo, T., et al. 2008, MNRAS, 384, 535

Sales, L. V., Navarro, J. F., Schaye, J., et al. 2010, MNRAS, 409, 1541

Saviane, I., Held, E. V., & Piotto, G. 1996, A&A, 315, 40

Sawala, T., Scannapieco, C., Maio, U., & White, S. 2010, MNRAS, 402, 1599

Sawala, T., Scannapieco, C., & White, S. 2012, MNRAS, 420, 1714

Scannapieco, C., Tissera, P. B., White, S. D. M., & Springel, V. 2006, MNRAS, 371, 1125

Schaye, J., Dalla Vecchia, C., Booth, C. M., et al. 2010, MNRAS, 402, 1536

Schure, K. M., Kosenko, D., Kaastra, J. S., Keppens, R., & Vink, J. 2009, A&A, 508, 751

Sedov, L. I. 1959, Similarity and Dimensional Methods in Mechanics

Shang, C., Bryan, G. L., & Haiman, Z. 2010, MNRAS, 402, 1249

Simon, J. D., & Geha, M. 2007, ApJ, 670, 313

Slyz, A. D., Devriendt, J. E. G., Bryan, G., & Silk, J. 2005, MNRAS, 356, 737

Smith, B., Sigurdsson, S., & Abel, T. 2008, MNRAS, 385, 1443

Smith, D. A., & Wang, Q. D. 2004, ApJ, 611, 881

Springel, V., & Hernquist, L. 2003, MNRAS, 339, 289

Stinson, G., Seth, A., Katz, N., et al. 2006, MNRAS, 373, 1074

Stone, J. M., & Norman, M. L. 1992, ApJS, 80, 753

Strigari, L. E., Bullock, J. S., Kaplinghat, M., et al. 2008, Nature, 454, 1096

Strigari, L. E., Frenk, C. S., & White, S. D. M. 2010, MNRAS, 408, 2364

Tasker, E. J., Brunino, R., Mitchell, N. L., et al. 2008, MNRAS, 390, 1267

Tasker, E. J., & Bryan, G. L. 2006, ApJ, 641, 878

Tassis, K., Gnedin, N. Y., & Kravtsov, A. V. 2012, ApJ, 745, 68

Taylor, G. 1950, Royal Society of London Proceedings Series A, 201, 159

Tegmark, M., Silk, J., Rees, M. J., et al. 1997, ApJ, 474, 1

Teyssier, M., Johnston, K. V., & Kuhlen, M. 2012, MNRAS, 426, 1808

Tinsley, B. M. 1979, ApJ, 229, 1046

Tollerud, E. J., Bullock, J. S., Graves, G. J., & Wolf, J. 2011, ApJ, 726, 108

Tolstoy, E., Hill, V., & Tosi, M. 2009, ARA&A, 47, 371

Truelove, J. K., Klein, R. I., McKee, C. F., et al. 1997, ApJ, 489, L179

Turk, M. J., Smith, B. D., Oishi, J. S., et al. 2011, ApJS, 192, 9

van Leer, B. 1977, Journal of Computational Physics, 23, 276

van Veelen, B., Langer, N., Vink, J., García-Segura, G., & van Marle, A. J. 2009, A&A, 503, 495

Vera-Ciro, C. A., Helmi, A., Starkenburg, E., & Breddels, M. A. 2013, MNRAS, 428, 1696

Wadepuhl, M., & Springel, V. 2011, MNRAS, 410, 1975

Walker, M. G., Belokurov, V., Evans, N. W., et al. 2009a, ApJ, 694, L144

Walker, M. G., Mateo, M., Olszewski, E. W., et al. 2007, ApJ, 667, L53

—. 2009b, ApJ, 704, 1274

Walker, M. G., Mateo, M., Olszewski, E. W., Sen, B., & Woodroofe, M. 2009c, AJ, 137, 3109

Walker, M. G., & Peñarrubia, J. 2011, ApJ, 742, 20

Weisz, D. R., Dolphin, A. E., Dalcanton, J. J., et al. 2011a, ApJ, 743, 8

Weisz, D. R., Dalcanton, J. J., Williams, B. F., et al. 2011b, ApJ, 739, 5

Whalen, D., O'Shea, B. W., Smidt, J., & Norman, M. L. 2008, ApJ, 679, 925

Wise, J. H., Abel, T., Turk, M. J., Norman, M. L., & Smith, B. D. 2012a, MNRAS, 427, 311

Wise, J. H., Turk, M. J., Norman, M. L., & Abel, T. 2012b, ApJ, 745, 50

Wolcott-Green, J., Haiman, Z., & Bryan, G. L. 2011, MNRAS, 418, 838

Woo, J., Courteau, S., & Dekel, A. 2008, MNRAS, 390, 1453